AN INVESTIGATION OF A SUPERCLUSTER OF GALAXIES IN PISCIS AUSTRINIS

Peter S. Bunclark

A Thesis Submitted for the Degree of PhD
at the
University of St Andrews

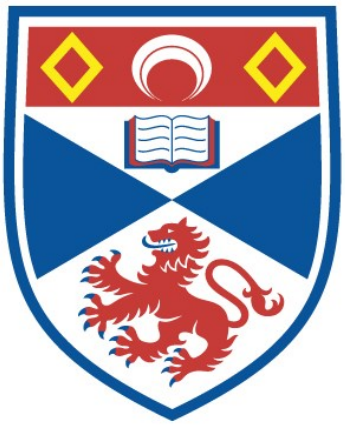

1986

An Investigation of a Supercluster of Galaxies in Piscis Austrinus.

Peter S. Bunclark.

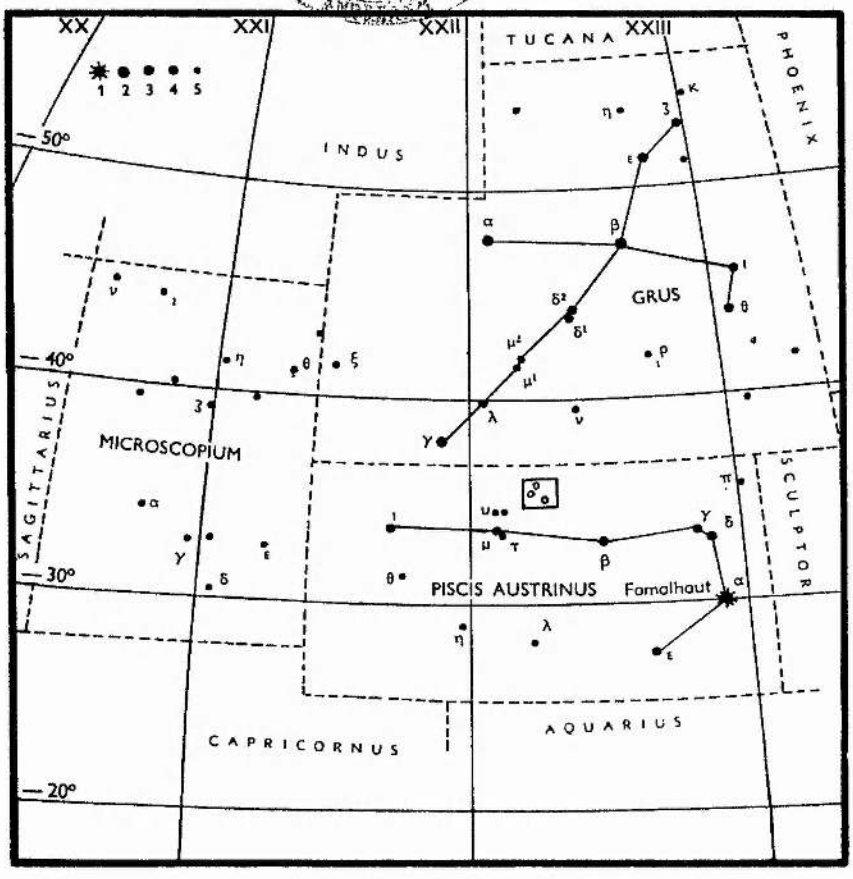

ProQuest LLC.
789 East Eisenhower Parkway
P.O. Box 1346
Ann Arbor, MI 48106 – 1346

An Investigation of a Supercluster in Piscis Austrinus.

ABSTRACT

An examination of a IIIaJ plate taken on the United Kingdom Schmidt Telescope of Survey field 405 revealed a possible supercluster of clusters of galaxies. Three rich clusters could be seen grouped within one degree, and which appeared to be of similar distance.

The project described in this thesis has investigated the supercluster hypothesis by determining relative (and less precisely, absolute) distances to the three component clusters. It is described how the photographic material was painstakingly reduced to relative magnitudes and colours, and how these values were calibrated using a stellar sequence photo-electrically observed using the 1m telescope at South African Astronomical Observatory. Radial velocities were determined by a process which maximises the amount of information derived from intrinsically low-precision objective prism material.

It is found that the Supercluster has, within the errors, a line-of-sight dimension of twice its projected dimension; this suggests that in fact the clusters of galaxies are in as close proximity spatially as they are apparently. The distance derived to the supercluster is 550 Mpc, giving a projected diameter of 10Mpc, with a recession velocity of 47700 kms^{-1} which leads to a determination of Hubble's constant:

$$H_o = 87 \pm 20 \ kms^{-1}Mpc^{-1}$$

CERTIFICATE

We certify that P.S. Bunclark has spent nine terms in research in the Department of Astronomy of the University of St Andrews, that he has fulfilled the conditions of Ordinance General No.12 and Senate Regulations under Resolution of the University Court, 1967, No.1, and that he is qualified to submit the accompanying thesis in application for the degree of Ph.D.

C.W. Fraser

D.W.N. Stibbs

PREFACE

The thesis presented in this volume deals with the determination of relative distances to an apparent group of three clusters of galaxies in Piscis Austrinus which are suspected of being component parts of a supercluster.

The raw material used is a set of photographic plates taken by the United Kingdom Schmidt Telescope Unit, photometrically calibrated from a photoelectrically observed stellar sequence. Chapter I introduces the astronomical background, aim and problems associated with the work. Chapter II reports the observation and reduction of the sequence. Chapters III, IV and V describe the techniques evolved to cope with the difficult problem of photographic photometry of faint galaxies. Chapter VI demonstrates the use of an objective prism plate to measure useful radial velocities of cluster members. Finally Chapter VII collates the photometric and spectroscopic distance estimations and completes the project. A value for Hubble's constant is also derived from the data.

Declaration.

I, Peter Stephen Bunclark, hereby certify that this thesis which is approximately 29,000 words in length has been written by me, that it is the record of work carried out by me, and that it has not been submitted in any previous application for a higher degree.

Septemb 1985

I was admitted as a research student under Ordinance No. 12 and as a candidate for the degree of Ph.D. on 1st October 1976, the higher study for which was carried out under supervision in the University of St Andrews between 1976 and 1979, and completed at the Institute of Astronomy in the University of Cambridge.

Date September 1985

In submitting this thesis to the Unversity of St Andrews I understand that I am giving permission for it to be made available for use in accordance with the regulations of the University Library for the time being in force, subject to any copyright vested in the work not being affected thereby. I also understand that the title and abstract will be published, and that a copy of the work may be made and supplied to any bona fide library or research worker.

I would like to acknowledge the help, guidance and perseverance of my two supervisors during the production of this work, formerly Dr C. W. Fraser and latterly Professor D. W. N. Stibbs, and to Dr H. T. MacGillivray and Dr R. J. Dodd for providing the inspiration for this project. I am grateful to the Science Research Council for three year's financial support and subsequent employment with the APM group. Thanks are also due to Margaret Harding and Jean Burris who typed the substantial part of the thesis.

CONTENTS

CHAPTER I

Introduction.

Superclusters of galaxies are now accepted entities in the Cosmological Scene. They are probably the largest identifiable discrete "objects" which can be observed except for the Universe itself.

The acceptance of the existence of superclusters has only recently come about, but now we talk freely of, for example, "the local supercluster".

Clusters on all scales are powerful astronomical probes. Star clusters have long been studied, their value being of course that the set of stars identified with a particular cluster have a common formation mixture and evolution time. Further, these stars are at the same distance from the sun and suffer similar interstellar absorbtion. Thus it is easy and valuable to construct a stellar cluster colour-magnitude diagram, rather than the much more difficult Hertzsprung-Russell diagram, and immediately derive (at least comparative) stellar composition, age and evolution (Shu 1982).

The usefulness of clusters extends up through the hierarchy to resolved galaxies, where the colour-magnitude diagram is still a powerful tool, to clusters of galaxies. Jones and Forman (1984) state: "Clusters of galaxies are the largest well-studied aggregates of matter in the universe. Their study is significant in the determination of the large-scale distribution of matter in the Universe as well as for understanding the structure and evolution of clusters themselves."

Following the lead of all this work on clusters of larger and larger scales takes us naturally to the study of superclusters of clusters of galaxies. Firstly, superclusters must be identified and established as such; then their properties can be used in conjunction with modelling to place constraints on both their origin and evolution, and that of their component clusters and galaxies within the clusters (for example Binggeli 1982, Dekel, West and Aarseth 1984).

Specifically, this thesis deals with a suspected supercluster in Piscis Austrinus whose possible existence was suggested by MacGillivray following an examination of a IIIaJ United Kingdom 48-inch Schmidt (UKST) plate of survey field 405. Three clusters were detected in a field of two square degrees, the two richest being tabulated in Braid and MacGillivray (1978) as numbers 301 and 302. Confusingly, the authors place no 302 at 0.6 arcmin, corresponding to 6.5mm on the plate, too far West, and 301 about half that error. A geometrical examination of these three clusters is described in MacGillivray et al (1976) using COSMOS data from the IIIaJ plate. That paper suggests from a comparison of the ten brightest galaxies in each cluster that they are of a "similar distance".

This investigation has examined the supercluster hypothesis using a photometrically calibrated UBVR sequence of UKST plates combined with UKST objective prism data (table 1.1).

Monochromatic Photometry.

Probably the most useful presentation of one-colour studies of clusters of galaxies is the luminosity function. It would be useful if the luminosity function were identical for all clusters, in which case the well-known logarithmic integrated luminosity function would be universal, requiring only a horizontal and vertical shift to match it

Plate		field	ra	dec	date	time	emuls	filter	expos	quality		
B 2371	HTM	N1	22 14.0	-35 40	76-06-02	20:38	IIAO	GG 385	65.0	B		B 2371
V 2392	HTM	N1	22 14.0	-35 40	76-06-24	22:17	IIAD	GG 495	60.0	A		V 2392
R 2419	HTM	N1	22 14.0	-35 40	76-07-06	22:58	098	RG 630	70.0	A		R 2419
U 2547	HTM	N1	22 14.0	-35 40	76-08-25	20:46	IIAO	UG1	100.0	BIT		U 2547
UJ 2620P	HTM	N1	22 14.0	-35 40	76-09-22	21:49	IIIAJ	NONE	75.0	BI	IN	UJ 2620P
B 4248	CWF	405	22 24.0	-35 00	78-05-05	20:11	IIAO	GG 385	5.0	A		B 4248
R 4269	CWF	405	22 24.0	-35 00	78-05-14	19:54	098	RG 630	5.0	BI		R 4269
V 4270	CWF	405	22 24.0	-35 00	78-05-14	20:10	IIAD	GG 495	5.0	BI		V 4270
U 4418	CWF	405	22 24.0	-35 00	78-08-03	21:20	IIAO	UG1	120.0	BI		U 4418

Table 1.1: The set of UKST plates used.

to a particular cluster, depending on distance and richness respectively. As pointed out by Dressler (1978), it can be seen from inspecting Sky Survey prints that luminosity functions of clusters of galaxies are fairly similar, consisting of a more or less flat faint end terminated by a steep cutoff for high luminosity galaxies, which occurs at approximately the same absolute magnitude in different clusters.

This apparent similarity would, as stated above, be of great value if it could be demonstrated with certainty, and preferably if some reasonable physical explanation of the phenomenon could be given. Abell (e.g. Abell 1975) has proposed that observational evidence does demonstrate the universality of the luminosity function; he characterises the shape of the logarithmic cumulative function as

$$\log N(\leq m) = K_1 + S_1 m \qquad m \leq m*$$
$$\log N(\leq m) = K_2 + S_2 m \qquad m > m*$$

where $S_1 \approx 0.75$ and $S_2 \approx 0.25$. The quantity "m*" is the magnitude of the break and is potentially an excellent standard candle for distance determinations. As with any parameter derived from data from a whole luminosity function, m* depends on data for many galaxies, and so should be much more stable than the magnitude of, say, the brightest member of a cluster.

Schecter (1976) has proposed a continuous luminosity function:-

$$\Phi(L)dL = \Phi*(L/L*)^{\alpha}\exp(-L/L*)\, d(L/L*)$$

where $\Phi*$, $L*$ and α are parameters to be determined from the data. The parameter $\Phi*$ is a number per unit volume, and $L*$ is a characteristic luminosity leading to a characteristic magnitude, $M*$, at which the

luminosity function exhibits a rapid change in the slope on the (log Φ, log L) plane, and which is very similar to the m* break of Abell. The dimensionless parameter α gives the slope of the luminosity function in the (log Φ , log L) plane when $L << L^*$. Schecter finds that the expression gives a good approximation to both the general luminosity function and the cluster-galaxy function over a range of 6 magnitudes, the only difference being a multiplicative constant.

This useful observational result might arise if galaxies were formed at an earlier epoch than clusters and under relatively uniform conditions over large volumes of space. In this case the luminosity function of a cluster would reflect only statistical selection from a population of galaxies whose luminosity distribution is universal. However, Dressler (1978) has found that in a sample of 12 rich clusters there exists variations too large to be purely statistical fluctuations, implying (1) large scale (cluster size) inhomogeneities of density, temperature, or angular momentum might have existed in the early universe; (2) clusters may undergo evolutionary changes which result in alteration of the original luminosity function (for example, a cD galaxy might cannibalize other massive cluster members; collisions and stripping might also alter galaxy characteristics); (3) clusters themselves might have formed at an earlier epoch than individual galaxies.

There is, in fact, strong evidence to suggest that cD galaxies can remove the outer envelopes of nearby galaxies, leaving them subluminous but of comparatively high surface brightness.

Multi-colour Photometry.

It is desirable to employ wide-band filters so that as deep as possible a sample can be observed. It is further preferable to use the standard UBVR system to tie-in the work to the vast amount of

information already obtained with the system.

The usual colour indices derived from UBVR observations are of course (V-R), (B-V) and (U-B). However, Strom (Strom et al. 1977) shows that the index (U-R) is expected to reflect the metal abundance variations because as the metal-to-hydrogen ratio Z decreases: (1) The contribution of blue horizontal-branch stars to total-system light will increase, thus decreasing (U-R); (2) The mean effective temperature increases for the K and M giant stars; these dominate the system light at R and contribute somewhat at U. As a consequence of the increase in T_{eff}, (U-R) decreases; (3) Line blanketing for all stars that contribute to the total light observed in the U bandpass decreases, thus reducing (U-R). Strom demonstrates that (U-R) varies by a whole magnitude for the range of metallicities represented by globular clusters. He then justifies the assumption that (U-R) provides an appropriate index of metallicity in "mixed" formation systems such as E and SO galaxies as opposed to "single burst" globular clusters by demonstrating the similarity of the locus described by globular clusters in the (U-V) plane with that described by the halo colours of two galaxies. The (U-V) index measures primarily the fractional contribution of horizontal-branch stars and a decrease in line blanketing for all stellar types. (V-R) is a measure principally of the change in T-eff of the K and M giant stars which dominate the light in V and R. Strom concludes that the same agent that determines the globular cluster colours also determines the halo and nuclear region colours of these two galaxies.

It is observed that there is a correlation between galaxy colour and absolute magnitude. Faber (1973) argues that this effect arises from a variation of mean metal abundances along the luminosity sequence where the mean chemical composition of the lower-luminosity

galaxies appears to be lower. Thus the index (U-R), being a good indication of metal abundance, should show the best correlation with M_V. Apart from implications of the internal physics of galaxies, this property could be a distance indicator for clusters of galaxies. Strom (1978) finds (U-R) = 0.24 - 0.101 M_V for Coma centre; this is apparently in good agreement with results obtained by Sandage. If this relation is universal, comparison with the (U-R)/V diagram for a particular cluster would lead to its distance modulus.

Biographical Note.

The work described in this thesis was originally envisaged as a joint project between the Royal Observatory, Edinburgh (ROE) and the Astronomy (now Astronomy and Astrophysics) Department at the University of St. Andrews. The earlier geometrical work of MacGillivray et al (1976) was to be followed up by radial velocity measures undertaken by Dodd and MacGillivray at ROE, providing kinematic data, and a detailed photometric study by Fraser and the author at St. Andrews, building on the extensive experience gained in surface photometry of nearer galaxies (Fraser 1976, Blackman 1977).

While work started on the photographic photometry at St. Andrews, applications for Anglo-Australian Telescope time to obtain calibrating UBVR photometry and spectra for radial velocities of some cluster members were unsuccessful. [In fact ROE did not take further direct part in the project.] The author felt that radial velocity data would add such a useful extra dimension to the study that measurements from the UKST objective prism plates were attempted. This extra facet took the elapsed time beyond the three-year Science Research Council support grant, and the author took up a position with the Automatic Plate Measuring (APM) group at the Institute of Astronomy in Cambridge.

Whilst the experience gained at St. Andrews in techniques of

photographic photometry, machine control and reduction techniques became invaluable in continuing the development of APM (Bunclark 1982), there was an adverse effect on the supercluster project. However, the APM system was used to supplement the St. Andrews Joyce-Loebl microdensitometer scans, and thereby led to a more extensive investigation than was originally possible.

CHAPTER II

PHOTO-ELECTRIC SEQUENCE

As noted in the introduction, the large-telescope time necessary for direct calibration of the galaxy photometry was not forthcoming, and consequently an indirect method was sought. It was decided to observe a stellar sequence in the UBVR passbands to match the Schmidt plate material. The method used to calibrate the photography with the sequence, differently for the Joyce Loebl data and the APM data, will be described in the relevant sections.

Observations were carried out in September 1977 by C. W. Fraser, assisted by R.J. Dodd and A. Brown, and in September/October 1978 by the author and Fraser using the 1m telescope at the South African Astronomical Observatory (SAAO) and the St Andrews photometer in its pulse-counting mode (Kelly 1977). The standard UBVR filter set was used, for which the transformations at SAAO are accurately and regularly monitored.

The programme maybe divided into three sub-sequences in the vicinity of each of the clusters of galaxies. Finding charts for the sequences are shown in fig 2.1. Standard stars from the E regions were selected in the magnitude range $6.5 < V < 13.0$ from Cousins (1962,1976). A diaphragm of 14 arcsecond was used except for the final night of the observing programme when one of 7 arcsecond was

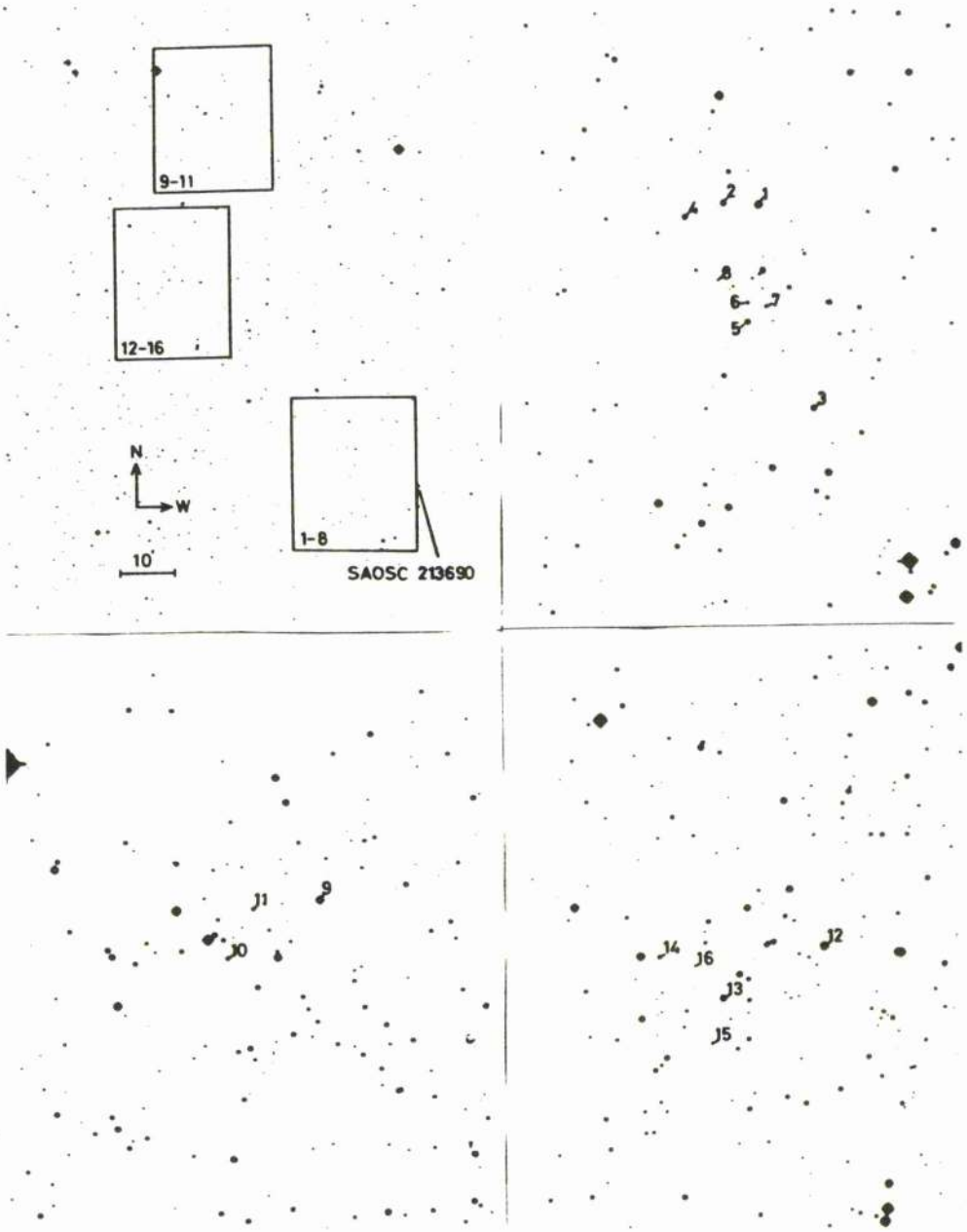

Figure 2.1: Finding chart of the whole sequence at top left, with enlargements of the three sub sequences for clarity. The co-ordinates of SAOSC 213690 are $22^h13^m54^s.4$, $-36^o1'58''.0$.

Star	α	β	V	B-V	U-B	n	V-R	n
0	22 13 54.7	-36 1 58	9.71	0.61	0.01	3	0.33	1
1	22 14 50.7	-35 55 36	12.12	0.94	0.65	2	0.53	1
2	22 14 58.2	-35 55 21	13.25	0.60	0.06	4	0.34	2
3	22 14 42.9	-36 4 49	13.54	0.95	0.77	2	0.55	1
4	22 15 6.8	-35 55 48	13.80	0.82	0.45	3	0.45	1
5	22 14 55.5	-36 0 46	13.86	1.01	0.80	3	0.58	1
6	22 14 55.1	-35 59 54	15.25	0.97	0.75	4	0.57	2
7	22 14 51.2	-36 0 9	15.98	1.52	1.42	3	1.11	2
8	22 15 1.0	-35 58 45	16.25	0.55	----	1	0.29	1
9	22 16 43.8	-34 52 30	12.01	0.98	0.71	1	0.51	1
10	22 17 3.7	-34 55 2	14.84	0.60	-.01	1	0.35	1
11	22 16 58.0	-34 52 50	14.89	0.56	-.01	1	0.35	1
12	22 17 3.7	-35 25 2	12.45	0.92	0.69	1	0.51	1
13	22 17 48.4	-35 27 19	13.50	0.88	0.59	1	0.49	1
14	22 18 2.1	-35 25 29	15.02	0.95	0.74	1	0.57	1
15	22 17 50.8	-35 29 21	16.06	0.52	-.03	1	0.33	1
16	22 17 54.5	-35 25 54	16.97	0.62	0.02	1	0.35	1

Fig. 2.2.

Coordinates (1950) and photometry of stellar sequence.

Star no. 0 is SAOSC 213690.

used.

The reductions were carried out on the IBM 360/44 of the University of St Andrews Computing Laboratory using software developed by D. Kilkenny.

For the UBV observations obtained with a photomultiplier with S-11 response (blue tube), the SAAO standard extinction coefficients and scale factors were used, but for the VR measurements, using a photomultiplier with S-20 response (red tube), they were calculated from the data.

A significant colour term was found only for the B measurements through the red tube, in the sense that a correction of $-0.033\ (B-V) + 0.23$ was required.

From overlap measurements obtained on several nights, the internal standard deviation of a single measurement for stars with $V < 14.0$ is 0.015m in V and 0.011m in (B-V), and for stars with $14.0 < V < 15.5$, it is 0.025m and 0.011m respectively. Although the results for some of the fainter stars follow from single observations, dictated by very limited observing runs, the corresponding formal deviations for stars with $V > 15.5$ are 0.05m and 0.04m in V and (B-V). The possibility of spurious errors or misidentifications was eliminated by comparison with the photographic material. The results are tabulated in fig. 2.2. The co-ordinates were measured from an APM scan of UKST plate V2392, the epoch of that plate being 1976.6 and the co-ordinates deduced for equinox 1950; the reference frame is that of the PERTH 70 catalogue (Høg and van der Heide 1976). The sequence has been published (Bunclark, Fraser and Dodd 1980).

Discussion.

While the photo-electric observations were actually made simply to calibrate the photography, it is useful to examine the results

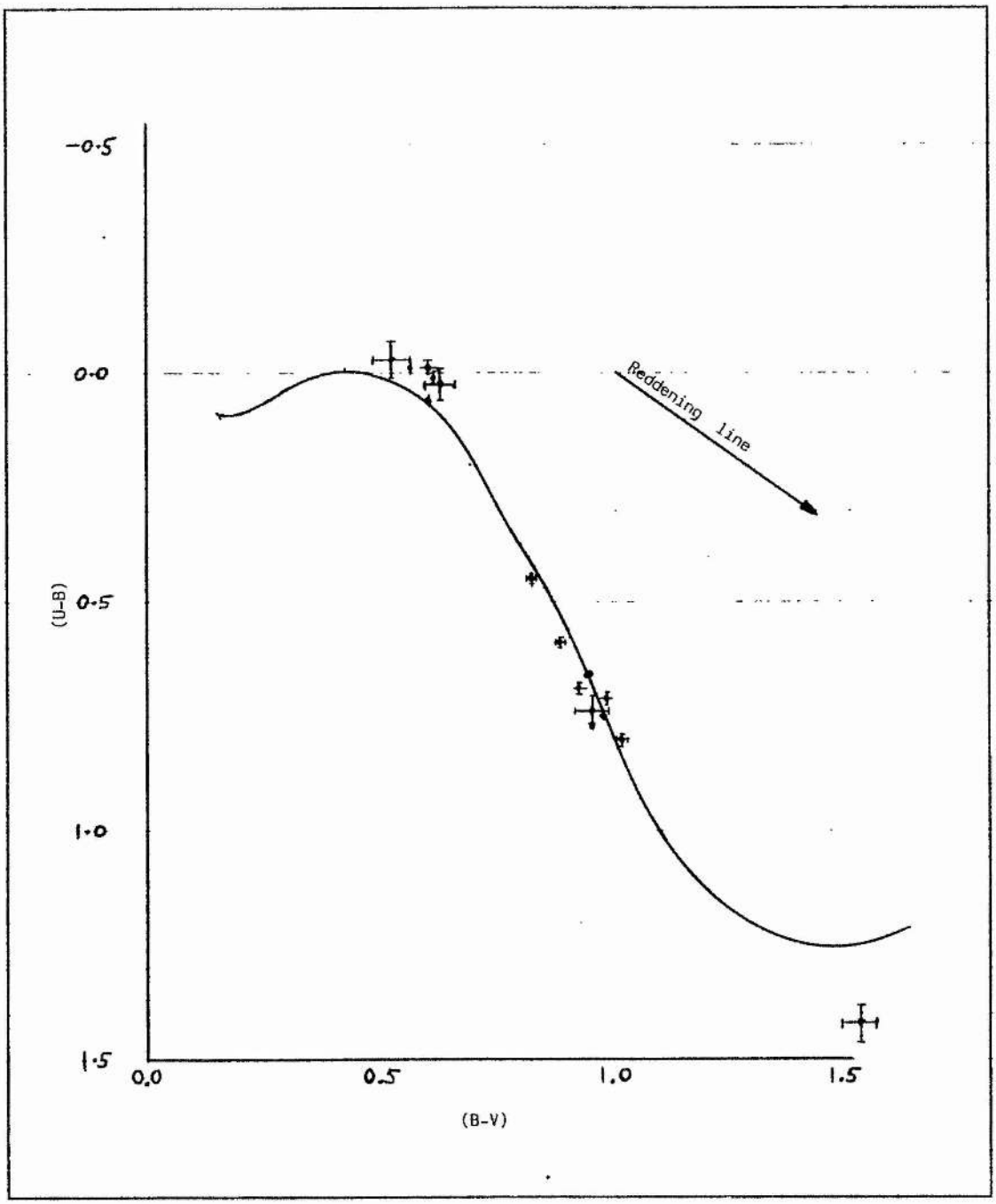

Figure 2.3: Two-colour diagram for sequence stars. The solid line is the main sequence.

Star	V	B-V	U-B	M_V	d/pc
0	9.71	0.61	0.01	4.6	100
1	12.12	0.94	0.65	6.3	150
2	13.25	0.60	0.06	4.5	560
3	13.54	0.95	0.77	6.4	270
4	13.80	0.82	0.45	5.8	400
5	13.86	1.01	0.80	6.6	280
6	15.25	0.97	0.75	8.8	560
7	15.98	1.52	1.42	10.0	157
8	16.25	0.55	——	4.2	2600
9	12.01	0.98	0.96	6.4	132
10	14.84	0.60	-0.01	4.5	1200
11	14.89	0.56	-0.01	4.2	1400
12	12.45	0.92	0.69	6.0	160
13	13.50	0.88	0.59	6.2	290
14	15.02	0.95	0.74	8.5	500
15	16.06	0.52	-0.03	4.0	2600
16	16.97	0.62	0.02	4.6	3000

Table 2.4.

Photometrically derived distances for sequence stars.

themselves for two reasons. Firstly, the UBV values for the stars are consistent with the standard main sequence; secondly, an estimation of the reddening in this direction ($l = 8.4$, $b = -56.1$) can be made. Fig. 2.3 shows the (U-B), (B-V) plot for the sequence superimposed on the luminosity class V main sequence (Mihalas and Binney 1981 table 3-3).

The stars with $0.8 < (B-V) < 1.1$ and star no. 2 at $(B-V) = 0.60$ could all lie on the main sequence within the errors. The group at $0.5 < (B-V) < 0.6$ seem to be metal poor (Mihalas and Binney 1981 figs. 3-11 and 3-12) with logarithmic metal abundances [Fe/H] relative to the Sun of about -0.1. The only star away from the main sequence is the reddest, namely no. 7. Its colours are more like those of a giant. Assuming all stars to be on the main sequence and not reddened, table 2.4 tabulates V, (B-V), (U-B), absolute visual magnitude (M_V) and distance in parsecs. In fact, the data presented in fig. 2.3 suggest that, to within the observational errors, there is no reddening in the direction of the field. Accordingly, this result will be applied to the extragalactic analysis.

CHAPTER III

Data Reduction of Joyce Loebl Scanned Direct Plates.

Introduction.

The objective of the next two chapters is to describe the scientific requirements of two-dimensional photographic data acquisition and analysis, and to demonstrate the practical processes of measurement and reduction in the context of this project.

The essential raw material for the project is a number of photographic plates on loan from the United Kingdom Schmidt Telescope Unit (UKSTU) at the Royal Observatory, Edinburgh. The production and delivery of these plates is well documented elsewhere and is not further described here. Absolute calibration is effected by means of stellar sequences photo-electrically observed on the 1m telescope of the South African Astronomical Observatory at Sutherland, the results of which are presented in Bunclark, Fraser & Dodd (1980) and in chapter II.

In this chapter the measurement and analysis of the plate material using the data processing facilities of the University Observatory, St Andrews, is described.

Joyce Loebl Microdensitometer.

Plate Table.

One of the initial problems encountered in this project was the absence of a mechanical support for the 14-inch (35cm) square UKST plates on the Joyce Loebl microdensitometer.

The sample table has a 13cm x 25cm plate holder recess; clearly the Schmidt plates have to be supported above the table. Two mechanical design constraints exist due to the small distance between the imaging optics and the central pedestal of the machine:- (i) the plate holder was not to protrude beyond the physical edge of the glass; and (ii) it was to remain as low as practicable since the pedestal slopes towards the optics so that the higher the plate is carried the smaller the objective-to-pedestal distance. It was also desirable to keep the plate low to maintain the focal plane near to its nominal position.

The solution to the problem is shown in plate 3.1. The two parallel steel bars faced with felt are held in opposite pairs of sample-table sockets by expanding bolts; the remaining four sockets hold small studs of identical cross section to the bars. The plates are held frictionally by their own weight. This fairly simple but well-engineered device holds the Schmidt plates evenly without sagging, and by rotation of the plate every part may be scanned apart from the central 6mm square.

Optics and Aperture.

There are two major reasons why the size of scanning aperture must be minimised. They are basically the practicality of obtaining density measurements, and the results of sampling theory.

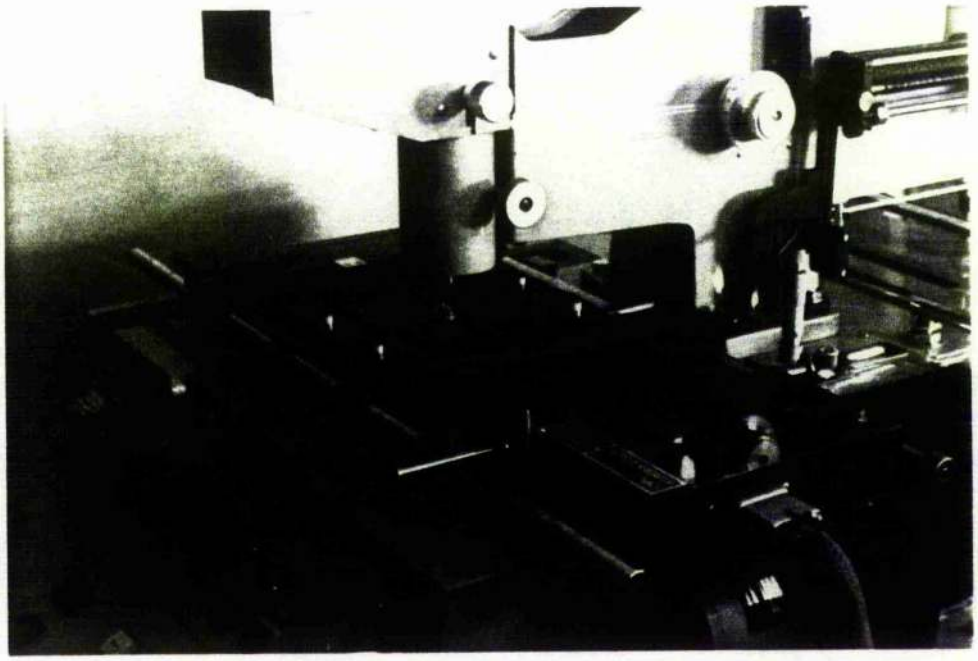

Plate 3.1

The Digitised Joyce Loebl Microdensitometer in the St Andrews University Observatory Data Processing Laboratory.

Note the addition of the plate support system consisting of two horizontal bars and four small studs, faced with felt.

The machine may be operated interactively from the front panel to aid setting up, and on-line from the host computer during scanning.

A microdensitometer nominally measures density. However, it actually averages the transmission over the area of the aperture and then converts this to density. To give a rather extreme example of the effect that this can have, let us suppose that within the area of the slit the sample has two equal parts, one of exactly density two and the other of density zero. Then the mean density over the slit is 1.0. However, the transmission over the area is just slightly greater than 0.5, which when converted to density is slightly greater than 0.3 - a huge error. Mathematically,

$$\frac{\iint D \, dx \, dy}{\iint dx \, dy} \neq \log \frac{\iint 10^{-D} dx \, dy}{\iint dx \, dy}$$

and the recorded data is not the true data convolved with the aperture. In more realistic cases, this effect imposes a criterion that the aperture width must be such that the density gradient within it is small.

Another, related effect is that if there is a density gradient within the slit area, then on calibration to intensity an average is taken over a part of the characteristic curve. This effect will be negligible if the previous criterion is satisfied. A photographic image is degraded by smearing effects and noise. When digitally recording an image, it is desirable to both avoid degrading the image further, and in fact to record enough information to attempt restoration.

The sampling theorem states that the image must be sampled at intervals of at least twice the maximum frequency present. This assumes an infinitely small sampling aperture, which in practice is of

course unattainable. However, if the characteristic width of the sampling device is denoted by a, the sampling interval by Δx, and the inverse of the resolution element width, the Nyquist frequency, by δn, then the ideal condition is

$$a << \Delta x \leq 1/(2\delta n)$$

(Fischel 1976).

This is not often possible since a reasonable aperture must be used to transmit a measurable signal, and the principle is further compromised by the need to keep the noise to a minimum. However, the condition $a \leq \Delta x$ can be considered essential if restoration is to be possible.

The application of the criterion to 48-inch Schmidt material calls for a square aperture of less than 15 micron. (15mu = 1".01 arcsec on UKST plates.) With the optics initially available on the Joyce Loebl, i.e. a x10 objective and a x3 condenser, it was found that at high density the pen would "stutter". This was taken to be photon noise causing rapid fluctuations in the photomultiplier output to the servo motor.

In investigating the cause of and solution to this problem, Dr R.P. Edwin (Senior Scientific Officer at the University Observatory, St Andrews) and the author visited Joyce Loebl at Gateshead. A sample of astronomical plate material was taken and the stuttering effect was reproduced on a factory microdensitometer.

This visit resulted in the purchase of a x20 objective which was combined with the x10 objective now used as a condenser. The new condenser had double the numerical aperture and so produced four times the illumination per unit area. A side effect of this is to decrease

the area of sample illuminated; however, the area now illuminated is still larger than that imaged on the slit, and so is more than adequate. The numerical aperture of the objective was chosen to match that of the condenser, and its higher magnification had a further advantage in that for a given sampling aperture the actual mechanical aperture is twice as wide, thereby making it easier to set.

Data Processing Facilities.

The facilities available at the beginning of the project were a digitised Joyce Loebl microdensitometer, interfaced by a CAMAC crate to a Data General Nova 820 minicomputer with 16k of memory, a Tektronix 4010 interactive graphics video terminal, a few other terminals, and one 2.3 megabyte cartridge disk drive. A Honeywell H316 minicomputer with 12k of core memory and a magnetic tape transport was available, but data could not be transferred between the two computers, and therefore at that time it could not be transported to a large computer for analysis. For this reason, the reduction of data was commenced using the Nova. However, it was later realised that keeping the data on-site had some considerable advantages, for example the avoidance of serious problems that often arise in reading magnetic tapes at another installation to that at which they were written. The Nova computer is multi-programmed in Forth (Moore 1974), an interactive computing language originally designed for equipment control by minicomputer. In addition to the primary function of photographic data digitisation and reduction, the system was also interfaced through CAMAC to a two-channel pulse-counting photometer used on either the 20-inch or 37-inch telescopes at the University Observatory, St Andrews. The photometer was used for both conventional and fast photometry, an example of the latter being the work of Brown, Bunclark, Stapleton &

Stewart (1979) on an occultation of Aldebaran.

As work on the project progressed, the system was extended as follows: the Nova and Honeywell were linked through CAMAC, enabling data to be stored on magnetic tape; the Honeywell was also programmed in Forth, and a disk drive was obtained for it, making the Honeywell capable of control of the Joyce Loebl and of handling some of the reduction procedures (in fact, any of those not employing floating-point arithmetic); a second disk drive, a second Tektronix 4010 and an extra 8k of memory were obtained for the Nova, so the Nova could practically support two simultaneous photometric reduction processes; a floating-point arithmetic unit was built as a CAMAC module based on the Advanced Micro Devices Am9511 calculator chip (Carr & Stapleton 1978), giving a gain in speed and also taking the load off the cpu - an important factor in this multi-programmed system. Finally a digital-to-analogue converter was built to drive a Hewlett-Packard X-Y recorder as a graph plotter on which many of the diagrams in this thesis were produced. The software for the plotter was written by the author in such a way that after the command "HP" any other command normally causing graphical output to a Tektronix 4010 produces identical results on the plotter. Further, a picture can first be displayed on a Tektronix for checking and without further alteration may then be obtained as a hard-copy paper output.

Scanning Control.

The digitised Joyce Loebl had been interfaced through CAMAC to the Honewell H316 computer and controlled by a Fortran/Assembler programme, van Breda et al. (1974).

In this mode, it was used extensively (e.g. Blackman 1977) but for this project the old programme was discarded. It had certain

limitations, for example, a scan size was set by using push-buttons to delimit the perimeter of a field; whilst this was a useful function it is preferable to have the facility of numerically defining a scan area to a specific size. A further drawback was that at that time the only mass storage device was a magnetictape transport; during a raster, the data for each scan line was written as a single record on to tape. Writing one record with a gap of the order of three minutes for many hours is far from optimum operating conditions, and frequently a scan would be ruined by a fatal tape drive error. (In April 1979 the H316 was interfaced to a disk drive.) Finally, the programmer responsible for the Joyce Loebl driver left the group and it was felt that it would be extremely time consuming to extend or modify the existing programme.

At the commencement of this project, a Forth system had been implemented on the Data General Nova 820 minicomputer. Since the Joyce Loebl was interfaced through CAMAC, no additional hardware was required to drive it from the Nova.

At that time the Nova had one disk drive, and a rudimentary scanning programme had been written.

It was realised that with the power and flexibility of Forth, a high-level scanning programme with all required features could be easily implemented. In fact, over the period of this project the programme was almost continually upgraded and added to either directly by the author, by Mr G.C. Stewart, or by Mr J.R. Stapleton in collaboration with them.

System Reliability.

Although most of the hardware gave trouble-free operation, there were at times some serious hardware faults which caused considerable

delays in data reduction.

Before the H316 tape drive and the Nova's second disk drive were available, a Tandberg cartridge recorder was added to the system. Not only was this used for archiving of data but some effort went into programming the drive as a real-time random-access mass-storage device, for use as intermediate storage during image processing. The Tandberg did not perform according to specification, and had to be abandoned. Archived data and all programming effort in that direction were wasted. The project was retarded until the H316 tape transport became available.

The following three faults slowed progress considerably:

(i) Due to the lack of a particular part of the technical specification by Advanced-Micro Devices for their AMD9511 maths chip, the AMD-based maths module had a design fault which resulted in the unit hanging up in a "busy" state, thereby halting all procedures using it.

(ii) A 16k Ampex memory board was installed in the Nova, giving the computer its full 32k capability. However, when the machine was run with the mixture of memory, the system would go down occasionally. The problem was not resolved and the memory board finally repossessed by the suppliers.

(iii) One of the disk drives developed a fault which caused it to drop its "ready" status. The disk software was adapted to check "ready" before initiating data transfer, but the drive occasionally dropped after data transfer commenced. The result was either corrupted data, or a system crash and corrupted data. Engineers were not able to trace the fault during the period of use by the author.

Each one of these problems disrupted progress, since even when an actual system crash did not occur, a data fault could, for example,

ruin an entire Fourier transform, in which every point in the transform is derived from every point in the data.

Fault (i) was eventually corrected; (ii) disappeared; and as stated above, (iii) was never overcome. Although system failure only occurred perhaps once in 50 hours of continuous use, it was nevertheless enough to ruin about two out of five attempts at restoring a 512 x 512 pixel image.

Additionally, there was the expected number of occasional failures which in general were corrected satisfactorily, causing only temporary delays in progress.

During the time span of this project, the data processing facilities underwent continuous extension and refinement, (in some aspects of which the author played a considerable role). Some penalty was, however, paid in that normal work was often disrupted. Nevertheless, the outcome was a data-processing system that was powerful in coping with the demands made by the research programmes in progress at the University Observatory.

Photometric Calibration.

The calibration of the photographic material has two stages: (i) the characteristic curve is used to derive relative intensities then (ii) the zero point of the intensity scale is determined photo-electrically.

Photographic Calibration.

The first stage utilises the step wedges impressed upon the North and East edges of the UKST plates. Since these wedges are exposed simultaneously with the main plate exposure, they should be ideal for calibration; unfortunately, the wedges used are themselves of poor

quality. However, the well-known Baker density linearised calibration-curve method is used (e.g. de Vaucouleurs 1968). Thus the seven step heights are fitted by a function with only two degrees of freedom which therefore is reasonably robust. With so few data, a more complex function, such as the five-parameter fit by Tsubaki & Engvold (1975), cannot be used as it would simply follow the errors in the points.

It was initially planned to have the facility of real-time conversion to intensity as a plate was scanned on the Joyce Loebl. Later it was decided to store raw data so that the choice of further processing could be left open. Little extra overhead ensues since digitisation takes much longer than calibration. Meanwhile, a routine was written to determine the calibration curve very rapidly. In the Baker-density system, first $\omega = 10^{D}-1$, where D is the density above fog level, is computed for each step, then

$$\log I = \log A + n \log(\omega)$$

The procedure for deriving A and n is as follows: a linear scan of a step wedge is made, and displayed either in real time or at any time later. The display is on a Tektronix 4010 interactive graphics terminal. The data in each step are averaged by picking off a region with the cross-hair cursor. In this way, spikes and defects can be rejected interactively. The averaging is done by the computer, then each step is converted to $\log(\omega)$, matched with the corresponding published value of log I as the independent variable.

The data, solution and residuals are then listed on the terminal and the data with fitted line are displayed graphically. The solution can then be visually examined for errors, and the value of n noted.

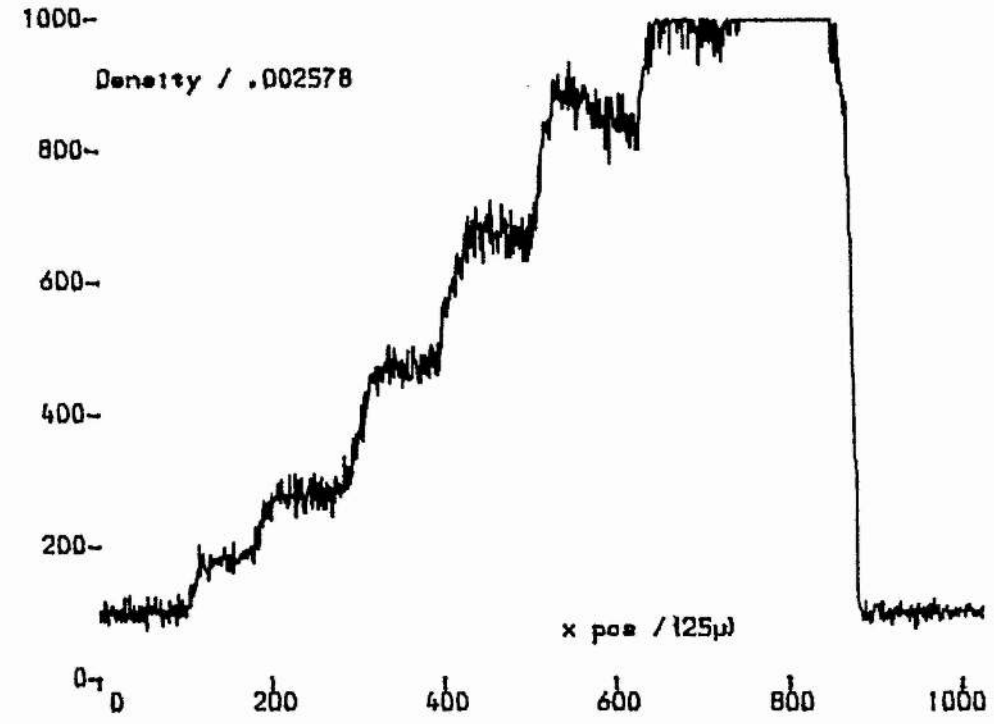

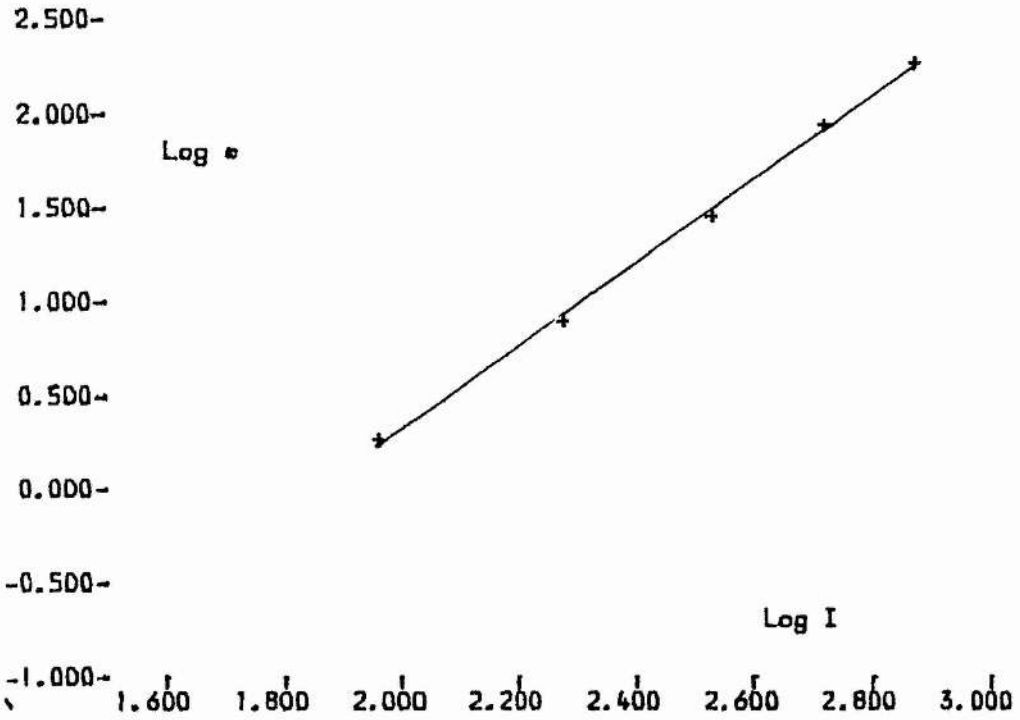

Figure 3.1: Example of calibration using a linear scan of a step wedge (top) showing the linear Baker Density vs log I relationship (below).

The value for A is not required since only relative intensity can be derived initially.

Scanning the wedge takes three or four minutes, and the complete reduction procedure takes between ten and sixty seconds depending on how much time is spent selecting steps interactively. Examples of the procedure are shown in Fig. 3.1

The value of n derived was combined with the scan data in several slightly different ways; the final method is described here.

The first problem in converting data to intensity is the resulting dynamic range. Data is recorded in density which is to first approximation proportional to log I. Thus the higher densities convert to a very large value of I. If the largest possible value of I is scaled to fit safely into a sixteen-bit integer, the resolution at low intensity is not adequate.

It was realised that normal spectrum data, when converted to intensity and normalised to the continuum, could easily be scaled in integer form since there is nothing above the continuum, all absorption lines obviously being below the continuum. Furthermore, the continuum is placed at 1.0, so the data lie in a very predictable range.

This fortuitous situation was reproduced in the case of direct two-dimensional images as follows: the raw data are displayed and a rectangular area of clear sky is selected using the cursor; the mean value is computed and converted to intensity using $I = \omega^n$. Next, each data value is converted to intensity and divided by the sky intensity; data in sky areas are now approximately 1.0, and those within objects are in units of the sky intensity. Finally, the reciprocal is taken so that all data are less than or equal to 1.0 but greater than zero, and this is scaled by 30,000 to fit conveniently into a sixteen-bit integer. Unsigned arithmetic is used so that there

is sufficient range above 30,000 (and below 65536) for negative noise spikes.

This scheme means the maximum possible dynamic range is catered for; also the resolution surpasses the original measurement resolution, and the scan occupies the minimum amount of storage space (i.e. one 16-bit word per pixel).

In practice each data point is not converted analytically; the Joyce Loebl has a ten bit density encoder so there can only possibly be 1024 intensity levels within a scan. These 1024 values are computed once (using floating point arithmetic) and placed in a look-up table; the scan conversion routine then refers to this table. In this way a 512 square scan is converted in about fifteen minutes.

Photo-electric Calibration.

At this stage 'instrumental' magnitudes and colours may be derived; to place these on an absolute scale, photo-electric calibration is necessary. Ideally, this would take the form of multi-aperture direct photometry of programme objects; however, as noted in Chapter II the large-telescope time necessary for the execution of such a procedure was not made available. Instead, a stellar sequence was obtained, in UBVR in the range V = 12 to V = 17.

Combining Photographic and Photo-Electric Data

Profile Fitting.

By the end of 1977 a partial sequence was available, i.e. there were values of UBV for eight stars, in the range V = 12.12 to V = 16.25. Short-exposure plates were not available until mid-1978, and so a method was devised to utilise the deep-exposure plates. It is

necessary to look at those parts of a star image away from saturation - i.e. the middle and outer parts of the image. To do this the expected shape of the image must be known.

The Final Profile of a Star Image.

Before any broadening mechanisms are applied to it, a star image may practically be thought of as a unit Dirac delta function multiplied by the luminosity of the image, so that the distribution of intensity in the image is $I_o(x,y) = L\delta(x_o,y_o)$, where (x_o,y_o) are the co-ordinates of the centre of the image on the tangent plane of the sky.

This distribution is then broadened by atmospheric seeing, then aberrations within the telescope before it reaches the image plane. This broadening is independent of the image brightness and over a small distance will be practically independent of position in the focal surface.

The broadened image is then received at the photographic plate and will be scattered, reflected and refracted within the emulsion. Let the convolution of all these broadened effects be b(x,y), then the intensity distribution of the star image can be represented by

$$\begin{aligned} I(x,y) &= I_o(x,y) * b(x,y) \\ &= L\delta(x_o,y_o) * b(x,y) \\ &= Lb(x-x_o,y-y_o) \end{aligned}$$

i.e. the luminosity multiplied by the broadened function shifted to x_o,y_o.

Finally this intensity distribution is then recorded by the emulsion, and if the plate can be calibrated correctly, I(x,y) will be

recovered.

All stars will have the same profile except for a scale factor proportional to their luminosity

As mentioned above however, the cores of the bright stars are not measurable.

Placing the origin of the co-ordinate system at the centre of a star, the intensity distribution is

$$I(x,y) = Lb(x,y)$$

$$\text{ie} \quad \log I(x,y) = \log L + \log b(x,y)$$

so in logarithmic co-ordinates the star profile is the broadening profile plus a vertical shift. If two stellar profiles were plotted on transparent paper and could be slid until they coincided, then the distance between their origins would give the magnitude scale.

To put these ideas into practice, a procedure was written to plot points in a stellar profile as a function of radius. The data for this procedure is a raster scan which has been calibrated and transformed into units of sky intensity. Values of log I(r) are printed on a hard-copy terminal with a resolution of one line per tenth of a raster step. A mean profile is then drawn manually through these points.

The validity of the above assumptions can now be tested as follows: the profiles are placed on top of one another so that the middle and outer parts coincide; then using any arbitrary zero point the shifts are measured and converted to magnitudes (-2.5 log I).

When these magnitudes are plotted against photo-electric magnitudes, the expected result is a straight line with a unit gradient.

The above procedure was tested using a scan of cluster #1 from

plate V2392. Six stars with photometry were available within the scan, and the application of the procedure gave a gradient of 1.186 + 0.044. The largest residual in the shift magnitudes was 0.150. Omitting this point, the gradient was 1.113 + 0.017, and the largest residual was 0.046. There is therefore a fairly small, systematic difference to the result that the gradient is 1.0, which can probably be explained by subjectively shifting the profiles too much, so a more objective approach is applied to the actual calibration.

Choosing an arbitrary but convenient zero point, the shifts that the profiles ought to have are calculated from the photo-electric measurements, and the profiles superimposed with these shifts. Since the gradient determined above was nearly unity, the result is not much different from the manually adjusted profiles.

Using this set of profiles, a 'true' overall profile can be drawn; the fainter stars give the central part faithfully, while the outer regions of the brighter stars are sufficiently above the noise to be determined accurately.

This composite profile is then digitised manually, and numerically integrated to give its instrumental magnitude; its actual magnitude was chosen initially in order to compute the vertical shift; thus the relationship between instrumental and actual magnitude is determined.

The integration of the composite profile involved an extrapolation to infinity; this was achieved graphically by plotting $1/L(r)$ vs $1/r$, and extrapolating to $1/r = 0$. The last measured point had been at $\log I = -2.3$, and the extrapolation beyond this point was determined to be only about 0.003 magnitudes. A larger error would result if the central region of the profile, containing most of the luminosity, were incorrectly determined: the largest error likely would seem to be an overall shift of about 5mm on the scale of the profiles,

which converts to an error of 0.30 magnitudes. This is probably pessimistic.

In the example stated, the V magnitude of the arbitrary profile was 15.87, and the corresponding derived instrumental magnitude was -5.25 + 0.30.

This gives the relationship

V = instrumental magnitude + 21.12.

The value 21.12 is the sky brightness per square raster unit which converts to 20.50 magnitudes per square arcsec.

Using this technique, it was possibleto achieve calibration, but not really with adequate accuracy. One drawback also was that it was impracticable to determine any colour term in the calibration.

Direct Integration

Once the short-exposure plates were available the calibration problem became more tractable. Stars of V = 13.5 on these plates are not saturated, and so the images of most of the stars in the sequence were able to be integrated directly. Then the sequence could be transferred to fainter stars for use on the deep plates.

The calibration procedure was now as follows: the cluster fields on the short-exposure plates were scanned and converted to relative intensity as described before; interactively, the sky brightness in the vicinity of each sequence was measured, then the area containing the star was selected and the total luminosity found by numerical integration.

Instrumental magnitudes were obtained by $m_i = -2.5 \log$ (luminosity).

In fact, all stars in each field were measured and their instrumentalmagnitudes stored in a catalogue on disk. (This catalogue and the method of combining the contents of catalogues in different colours are described later). Having reduced scans in all four colours, instrumental U-B, B-V and V-R colour indices are determined.

If the photographic pass-bands exactly matched the photo-electric pass-bands, then a plot of instrumental magnitude or colour against the photo-electric value would be a straight line with unit gradient. Since this is hardly likely to be so, it is assumed that for example $V = V_i + C_v(B-V)_i + Z_v$ where V_i and $(B-V)_i$ are instrumental magnitude and colour, C_v is the coefficient of the colour term and Z_v is the zero point. Then $(V-V_i)$ and $(B-V)_i$ are entered into a linear least squares solution to determine C_v and Z_v. Finally, all the other stars in the catalogue are converted to V. Rather than also determining U,B, and R it was felt better to directly calibrate instrumental colours with photo-electric ones. A similar relation to that for V is assumed for B:

$$B = B_i + C_b(B-V)_i + Z_b$$

so $$(B-V) = (B-V)_i + (C_b-C_v)(B-V)_i + (Z_b-Z_v)$$

therefore, $$(B-V) = [1 + (C_b-C_v)](B-V)_i + (Z_b-Z_v)$$

or $$(B-V) = C_{b-v}(B-V)_i + Z_{b-v}$$

The preference for this method is because some of the errors in determining B and V are systematically the same in both pass-bands; by directly deriving (B-V) these errors cancel. The principle is the same as that routinely applied in the reduction of photo-electric observations. A similar argument holds of course for (U-B) and (V-R). Figures 3.3 - 3.6 show the photo-electric/photographic fits for the sequence within the cluster 1 field. Table 3.1 lists the solutions

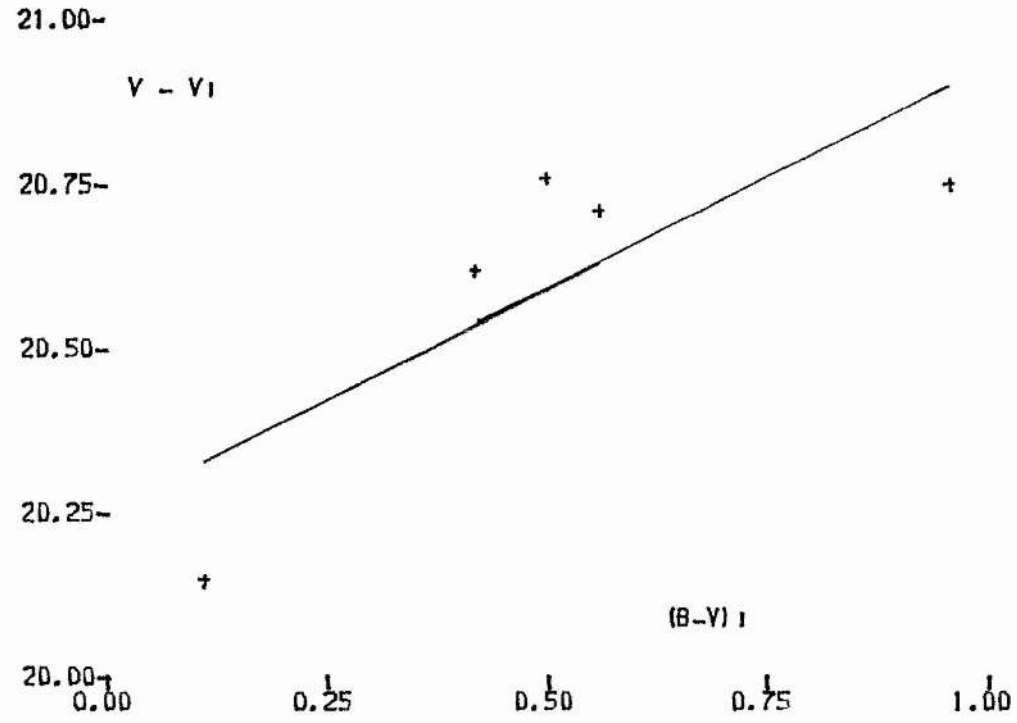

Figure 3.3: V calibration for cluster 1.

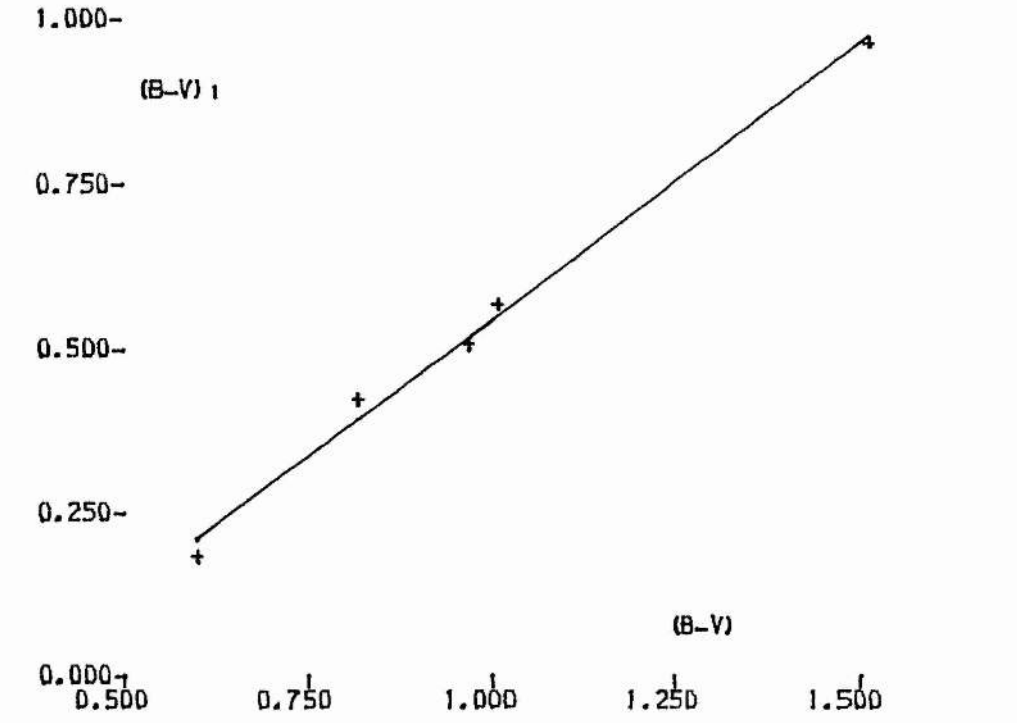

Figure 3.4: (B-V) calibration for cluster 1.

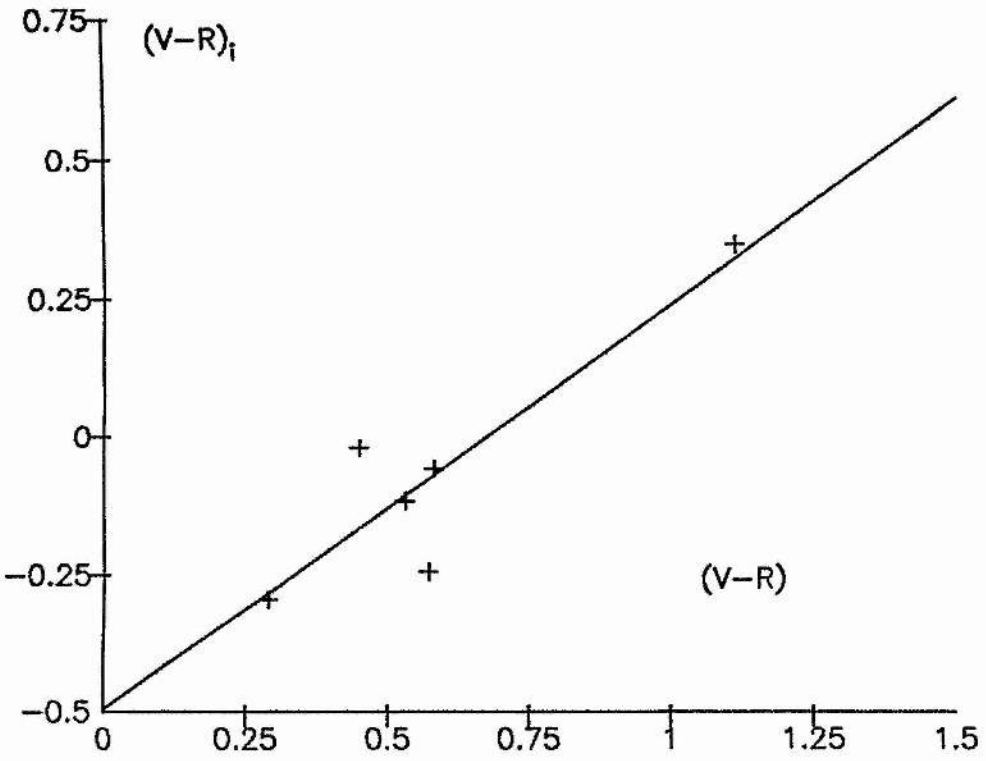

Figure 3.5: (V-R) calibration for cluster 1.

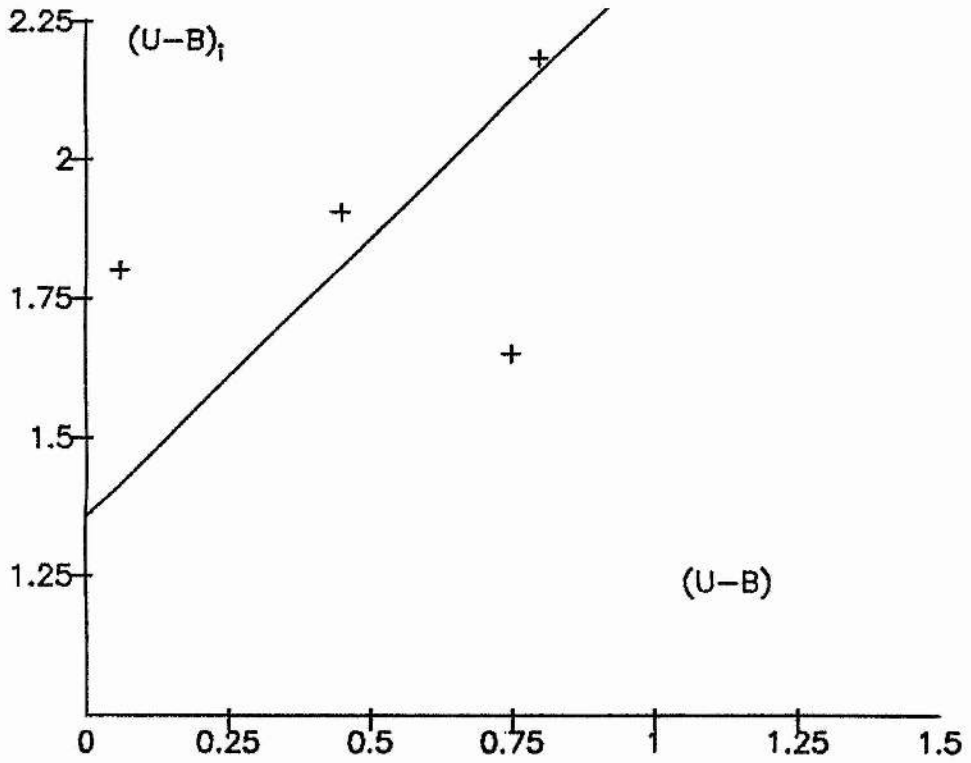

Figure 3.6: (U-B) calibration for cluster 1.

Vi	V	V-Vc
0.425	20.630	-0.088
0.570	20.718	-0.079
0.509	20.768	-0.170
0.117	20.152	0.184
0.965	20.751	0.152

gradient = 0.699 ± 0.299 intercept = 20.258 ± 0.175

(B-V)	(B-V)i	(B-V) - C
0.600	0.185	0.008
0.820	0.425	-0.042
1.010	0.570	-0.023
0.970	0.509	0.003
1.520	0.965	0.021
0.550	0.117	0.033

gradient = 0.862 ± 0.040 intercept = -0.324 ± 0.039

(V-R)	(V-R)i	(V-R)i - C
0.530	-0.117	0.008
0.450	-0.021	-0.146
0.580	-0.059	-0.013
0.570	-0.245	0.166
1.110	0.342	-0.026
0.290	-0.295	0.011

gradient = 0.732 ± 0.180 intercept = -0.496 ± 0.115

(U-B)	(U-B)i	(U-B)i - C
0.060	1.802	0.384
0.450	1.907	0.099
0.800	2.184	0.026
0.750	1.652	-0.456

gradient = 1 intercept = 1.358 ± 0.136

Table 3.1
Cluster #1 photo-electric/photographic calibrations.

plotted in figures 3.3 - 3.6 for V, (B-V), and (V-R). The fit for U-B was so poor that the relation

$$(U-B) = (U-B)_i + Z_{u-b}$$

was assumed, i.e. the data was solved only for a zero point. The reason for this poor fit would be due to a combination of the comparatively large error in the U photometry and the fact that the calibration wedges on UKST U plates are extremely faint, so that a value for the Baker "n" must be estimated from only two or three density steps. The internal errors of the photographic calibration, as determined from the mean residuals, are 0.135 mag in V, 0.065 in (V-R), 0.022 in (B-V), and 0.258 in (U-B).

Since the cluster 1 sequence was the most numerous with the largest spread of colour, the formal errors in the solutions were significantly better than those for the other two clusters; therefore the gradients obtained in the cluster 1 solutions were used in the clusters 2 and 3 solutions, only the zero-points being solved for in these cases.

Having obtained a faint photographic sequence, the same method is used to calibrate the deep exposure plates.

Image Restoration

Reasons for Fourier Image Analysis.

After an appraisal by the author of results of one-dimensional Fourier analysis techniques being applied to photographic spectrum data by other workers at the Observatory, it was decided to attempt two-dimensional Fourier restoration of the cluster image data.

Restoration can be considered as a process which attempts to reconstruct or recover an image that has been degraded by using some **a priori** knowledge of the degradation phenomenon. Thus, restoration techniques are oriented toward modelling the degradation and applying the inverse process in order to recover the original image. The process is designed to yield some optimum estimate of the desired result. Enhancement techniques, on the other hand, are basically cosmetic procedures which are designed to manipulate an image in order to take advantage of the psychophysical aspects of the human visual system. For example, contrast stretching is considered an enhancement technique because it is based primarily on the pleasing aspects it might present to the viewer, while removal of seeing and instrumental profile is considered a restoration problem. In photometric applications, a procedure like contrast stretching is valueless since the restoration process must conserve the energy of the data.

The advantage attainable with Fourier restoration depends on original image quality; if the data are very good, fairly complete restoration can be achieved; if the data are noisy, the high frequency noise can be selectively smoothed and partial restoration can take place.

The data obtained in this project are rather nearer the latter case; full restoration is not possible due to noise - so in effect the restored image is still broadened slightly by the smoothing function. However, unlike the instrumental profile, the smoothing function only affects high frequencies, so intermediate and outer regions of the small objects dealt with are well restored. Another advantage is that the instrumental profile and noise level are different for each plate; the smoothing function can be chosen to be the same. Thus all plates

processed can give final images of identical quality, i.e. a homogeneous data set is obtained. This is most important when results from one cluster are compared with those from another, or when obtaining colours from different plates of the same cluster. For example, fig. 3.7 shows the measured magnitude within an aperture for each object in the field of cluster 3 in R from restored data plotted against the corresponding aperture magnitude from unrestored data. The line of equality is shown, and it can be seen that the restoration has had the effect of brightening the aperture magnitudes by between 0.0 and 0.5 magnitudes. (N.B. the magnitudes are instrumental).

The Fourier Transform.

The main technical requirement for image enhancement is the capability of performing two-dimensional Fourier transforms and inverse transforms. The definition of the two-dimensional discrete Fourier transform is

$$F(u,v) = \sum_{x=0}^{N-1} \sum_{y=0}^{N-1} f(x,y) \exp[i2\pi(ux + vy)/N]$$

in the case of an NxN square data set, and the inverse Fourier transform is

$$f(x,y) = \frac{1}{N^2} \sum_{u=0}^{N-1} \sum_{v=0}^{N-1} F(u,v) \exp[-i2\pi(ux + vy)/N]$$

i.e. the inverse transform is the transform of the conjugate of the transform scaled by the total number of data points, so the same

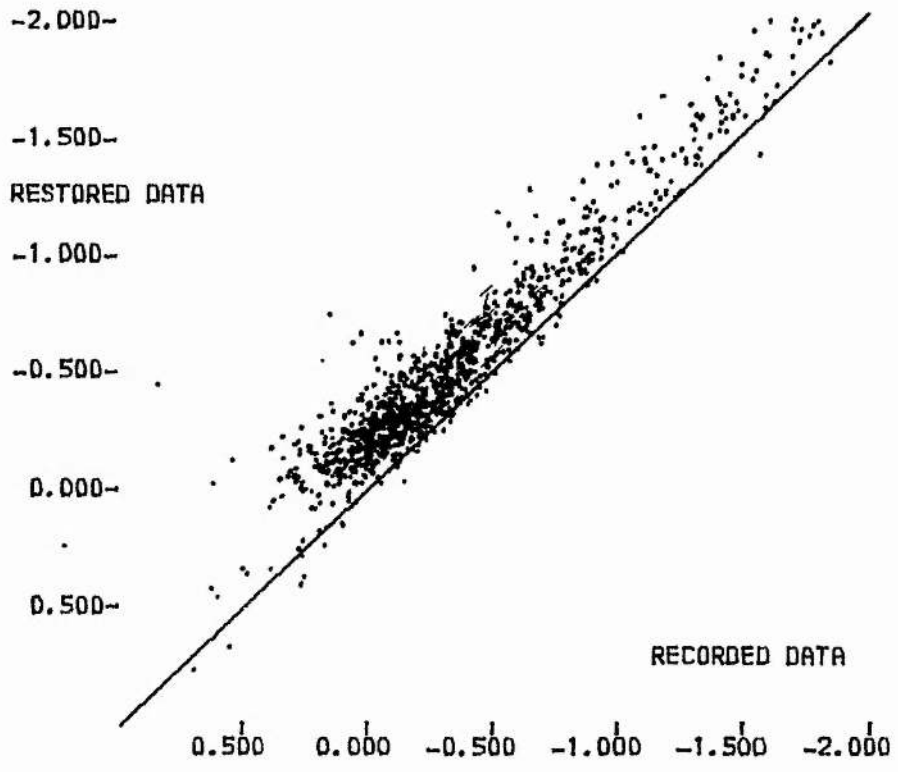

Figure 3.7: The effect of restoration: the same data when restored gives brighter V magnitudes.

routine is used for both forward and inverse transforms. Furthermore, the above equations are separable, and in practice a two-dimensional Fourier transform is achieved in two steps by repeated application of a one-dimensional transform. For example, first all the rows are transformed then all the columns.

Fourier Transform Algorithms.

The algorithm originally chosen is by Singleton (1963), based on the Cooley-Tukey algorithm, a multivariate transform capable of handling n dimensions of any size, and specially written for a virtual memory system, e.g. such as Forth where data are kept in arrays which behave as if permanently in core but which in fact normally reside on disk.

The Singleton routine is written in Algol, so once the author had chosen to use it, he had to translate it into Forth, meanwhile adapting it slightly to take advantage of Forth's parameter stack, etc. The two-dimensional transformation of a 512 square complex array took of the order of five hours on the Nova 820.

Since the Singleton routine is rather large, the Forth version was split into three components which are overlaid when the programme runs. More recently, because of increasing restriction on core space, a further two-dimensional Fourier transform routine was written based on the one-dimensional FFT Fortran subroutine given in Gonzalez & Wintz (1977). Although it is very slightly less efficient and can only handle dimensions in powers of two, it uses a fraction of the core space and, unlike the Singleton routine, requires no intermediate work area.

Restoration Procedure.

The procedure for the restoration of a two-dimensional image

follows that used for one-dimensional spectrum data (e.g. Gray 1976, Brault & White 1971) extended to two dimensions. A simplification can be made if all functions involved are circularly symmetric; plate noise is certainly non-directional, and the stellar profiles can also be taken to be circularly symmetric. The UKST plates are so well guided that no trailing is detectable, and the diffraction spikes caused by the plate holder supports contribute negligible energy. The justification for the latter claim is that on star images faint enough to be integrated, i.e. unsaturated, spikes are not visible. Finally, the optics of the UKST are such that asymmetries in the aberrations are within the seeing disk.

Degradation.

In order to perform reconstruction, it is first necessary to understand the degradation process. As stated in the photometric calibration section, it can be considered that there is a single broadening function, b(x,y), consisting of the convolution of seeing, aberrations, etc. The recorded image is then

$$d(x,y) = f(x,y) * b(x,y)$$

where '*' denotes convolution and f(x,y) is the unbroadened image. In the Fourier domain,

$$D(u,v) = F(u,v) \times B(u,v).$$

The image can then be reconstructed from

$$F(u,v) = D(u,v) / B(u,v)$$

and f(x,y) recovered by the inverse transform of F(u,v).

In fact, this procedure cannot be used unrestrainedly due to noise, but first the treatment of the instrumental profile is considered.

The Instrumental Profile.

The total broadening b(x,y) can be divided into two components: one part due to telescope aberrations, scattering in the emulsion, etc., which will be constant, and the other due to seeing and the random arrival of photons, which will have a statistical distribution. By averaging the images of several stars, the mean broadening effect can be determined. In practice, the weighted mean centre of a star image is computed (which will be to a fraction of a sample step) and the Fourier transform computed. Then the transform is phase-shifted to effect a real-domain spatial shift, using the weighted mean centre to place the star at the origin. The phase change required is such that

$$d(x-A,\ y-B) = D(u,v)\ \exp[-i2\ \pi(Au + Bv)]$$

Phase shifting in the frequency domain is preferred to actual spatial shifting since non-integral shifts are applied and 'wrap-around' is taken care of, i.e. that part of the image shifted off one edge reappears at the other.

When a collection of zero-centred star transforms has been obtained, they are averaged. It is possible to average Fourier transforms since they are linear, i.e. the transform of A plus the transform of B equals the transform of A plus B.

Finally the mean stellar transform can be retained to be used in the restoration process, or its inverse transform can be produced to

obtain the mean stellar profile.

A practical drawback to using a numerical model of the profile in this way is that a transform the same size as the data transform is required; this is both time consuming and inconvenient from the point of view of storage space.

It would be much simpler if the instrumental profile could be adequately approximated by an analytical function, particularly if that function had a straightforward analytical Fourier transform.

The most obvious function to use is a Gaussian; if the seeing is the dominant part of the broadening function, and seeing is a random effect when integrated over a reasonably long time, such as the typical exposure times of astronomical plates, then the probable distribution of intensity within a stellar image might be expected to be normal. A further simplification is obtained if the profile is circularly symmetric; then a one-dimensional function can be used. The broadening profile must have unit volume (or unit luminosity) since it does not alter the energy in the image; therefore the amplitude of the Fourier coefficients at zero frequency of its transform is required to be unity; and if the profile is circularly symmetric, its linear cross-section will be unity at zero frequency, thus it will have unit area in the spatial domain.

The form of Gaussian used is

$$g(x) = \frac{1}{\beta\sqrt{\pi}} \exp(-x^2/\beta^2)$$

and its Fourier transform is

$$G(u) = \exp(-\pi^2\beta^2 u^2)$$

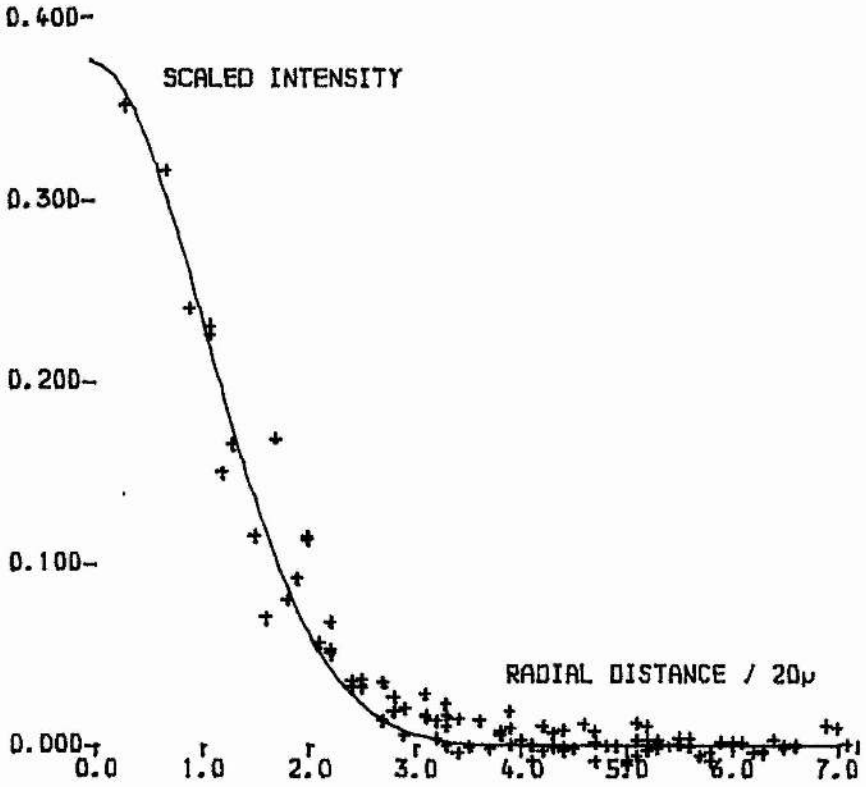

Figure 3.8: Stellar profile fitted with Gaussian.

It can be seen that at zero frequency, G(0) = 1.0, so the area under g(x) is 1.0; further, if G(u) is rotated about the origin in two-dimensions,

$$G(R) = \exp(-\pi^2\beta^2 \ R^2)$$

and G(0) is still 1.0; then the corresponding real-domain g(r) must have unit volume.

The Gaussian is fitted interactively; a star image is selected, and its weighted mean centre is found as before. The areas under the cross-sections in the x and y directions are calculated and averaged; using this value as a normalising factor each data point is plotted as a funtion of radius. Then the only free parameter needed to fit g(r) is β ; g(r) is plotted over the star data and β found by interactive iteration. This is performed for several stars and and an average β determined.

An example showing the adequacy of fit is shown in fig 3.8. The accuracy of the assumption of circular symmetry is visible from the amount of scatter in the horizontal direction in the star profile.

Noise.

Fig. 3.9 shows the amplitude of the first row of a 512 square Fourier transform of one of the clusters of galaxies in this study. Superimposed is the Gaussian restoration function, which is the inverse of the Fourier transform of the instrumental profile, I(u,v), and fig. 3.10 shows the effect of unrestrained application of this function. Clearly the high-frequency noise must be filtered. The optimum filter minimises the square of the errors between the true transform and the

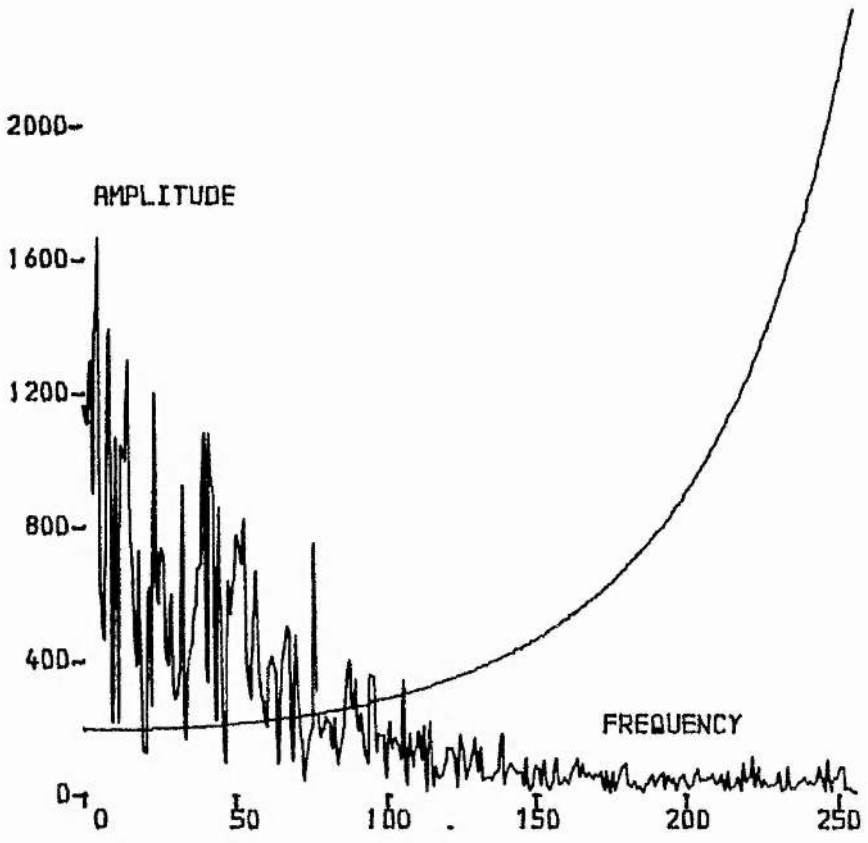

Figure 3.9: The amplitude spectrum of the transform of a cluster-field image. Superimposed is the required Gaussian restoration function.

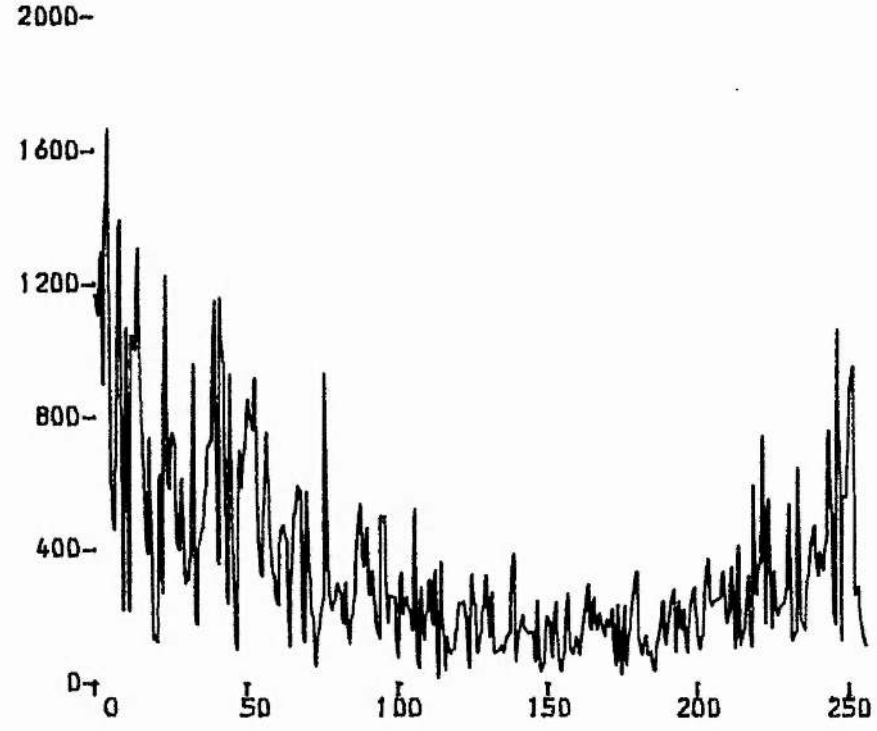

Figure 3.10: The effect of unrestrainedly applying the above restoration function.

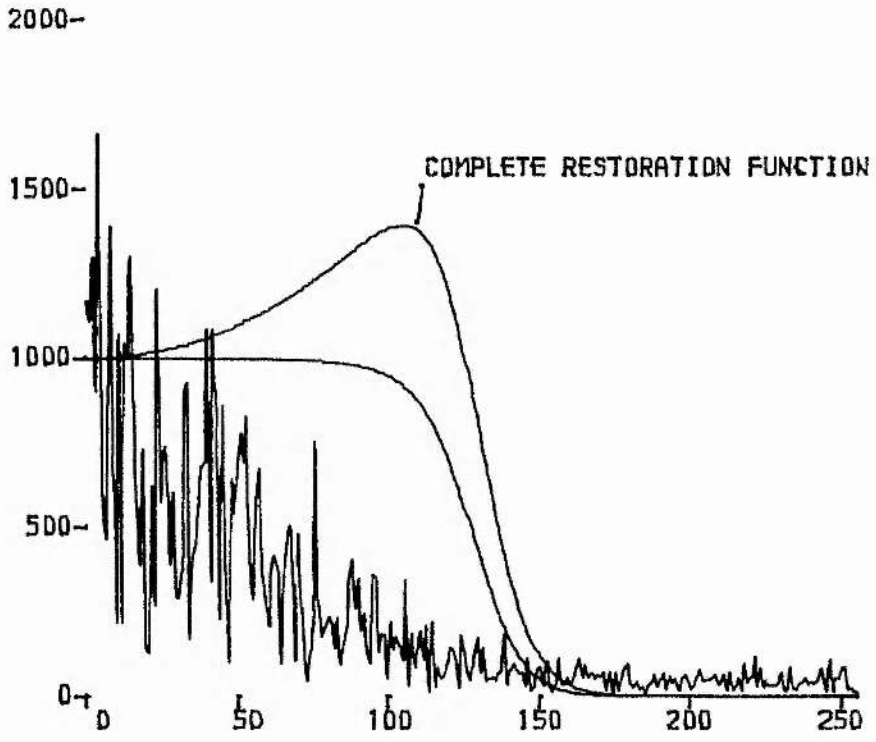

Figure 3.11: As figure 3.8 but with the noise filter plotted, and the combination of filter and restoration function.

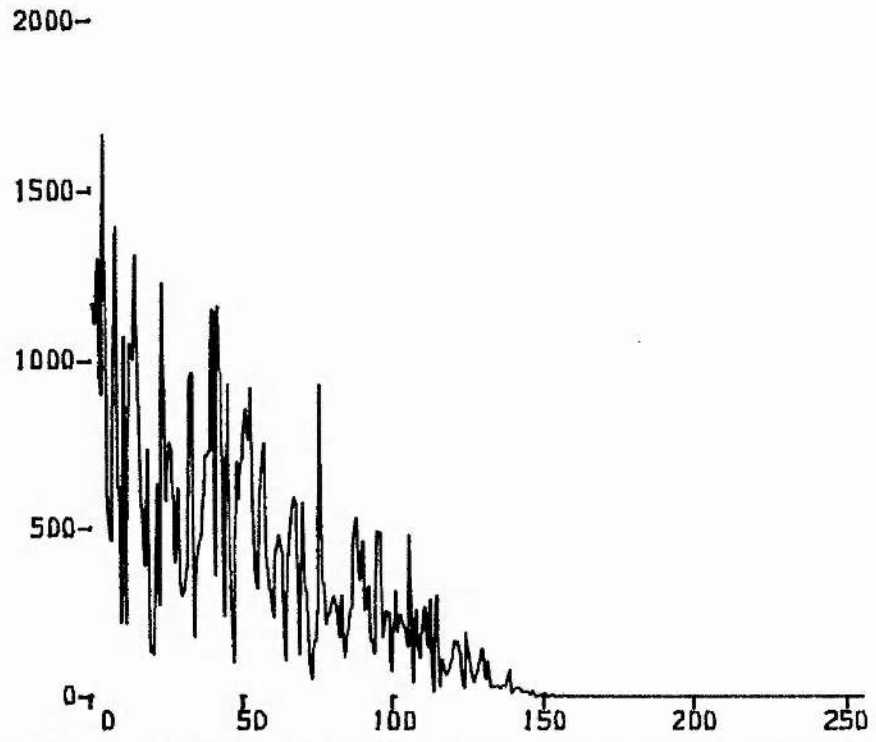

Figure 3.12: As figure 3.9 but with the filter included to restrain the high frequencies.

restored-filtered transform.

Let the transform in fig. 3.9 be written

$$D1(u,v) = D(u,v) + N(u,v)$$

where N(u,v) is the noise, and define the filtered reconstructed transform to be

$$F2(u,v) = \frac{D1(u,v)\ \ \Phi(u,v)}{I(u,v)}$$

where $\Phi(u,v)$ is the filter. The optimum filter can be shown to be (Brault & White 1971)

$$\Phi(u,v) = \frac{1}{1 + [N(u,v) \ / \ D(u,v)]^2}$$

N(u,v) can be taken to be white noise, and is then a constant, being the noise level determined from the high-frequency end of fig. 3.9. D(u,v) is not known beforehand, but a convenient approximation for many D(u,v)'s is the Gaussian, say

$$D(R) = A \exp[-(\pi\beta R)^2] \equiv A.10^{-\alpha_o^2\sigma^2}$$

again assuming circular symmetry. Then

$$\Phi(R) = \frac{1}{1 + (B/A)^2\ 10^{2\alpha_o^2R^2}}$$

makes a reasonable filter (Gray 1976). The ratio B/A is the noise level divided by the zero ordinate of D(u,v). The fitting parameter, α_o, is chosen initially interactively at the fig. 3.9 stage by choosing the cutoff and solving for α_o such that at the cutoff $\Phi(R) = 0.5$. Then in the region where $0.0 < \Phi(R) < 1.0$, i.e. where

its shape is most important, the corresponding Gaussian is found to fit the data reasonably well.

Fig. 3.11 shows the same data as fig. 3.9 but with the filter and the combination $\Phi(R)$ / $I(R)$ also plotted. Finally fig. 3.12 shows the combined effect of the restoration function and the filter on the data. The inverse transform of this result would now give an optimally filtered reconstructed image.

Derivation of Image Parameters.

Interactive Graphics.

The project lends itself to the use of interactive graphics in that the fields studied are small with a high density of objects.

The main graphical aid is an iso-intensity map which plots values above a chosen threshold, using the sequence of line, double line, space, to indicate increasing intensity levels analogous to an isodensitracing. The cross-hair cursor on the Tektronix 4010 can be used to pick off a rectangle around an object or area of interest. The data in that area can then be processed, or perhaps re-displayed on a larger scale. An automatic object finding algorithm would not only be large in size, take a long time to execute, but would also make some erroneous assessments, particularly toward the cluster centres where objects are either very close or actually overlapping. Then some interaction would be needed in any case. In fact the "Maximum Search" algorithm of Newell & O'Neil (1977) has been tried on the data of this project. The criteria these authors use to determine a practical solution are that the search algorithm be (1) as simple as possible to minimise computation time, and to enable its response to a given situation to be predicted accurately, (2) utilise the smallest possible space in the computer, to maximise core-space available for data arrays

and to minimise the impact of the complete reduction system on the computing facility, and (3) operate reliably despite changes in the character of the data arrays. In practice, it was found that the maximum search produced so many multiple hits that much interaction was needed anyway. Furthermore, an algorthim would then have to be used to determine the extent of the object when found to enable reduction to proceed. In conclusion the three criteria above are found to be mutually incompatible.

Another way of displaying data are a hidden-line isometric plot, giving a three-dimensional like projection. This is often used in a qualitative way, for example to see if an object such as a cD galaxy has a double nucleus. Using the iso-densi-tracing map such features are not necessarily definite.

These displays can be used at all stages of data processing, from raw Joyce Loebl data to final restored images; they can also be used to display two-dimensional Fourier transforms.

Sundry other routines are also available; e.g. spot co-ordinates and intensity heights can be picked off; random cross sections can be extracted; rows and columns of data can be displayed as one-dimensional traces. One-off special plots can be easily implemented - for example for use in fault tracing, recovery from system crash, etc.

As well as the objects themselves, working interactively allows a local area of sky free from objects to be measured whenever necessary. Finally any emulsion defects can be detected and either avoided or interpolated.

When analysing, for example, the large cD galaxies at the cluster centres, the many overlapping small objects must be removed. Two routines were written to do this, both requiring the objects to be 'boxed' using the graphics cursor: (i) the area containing the object

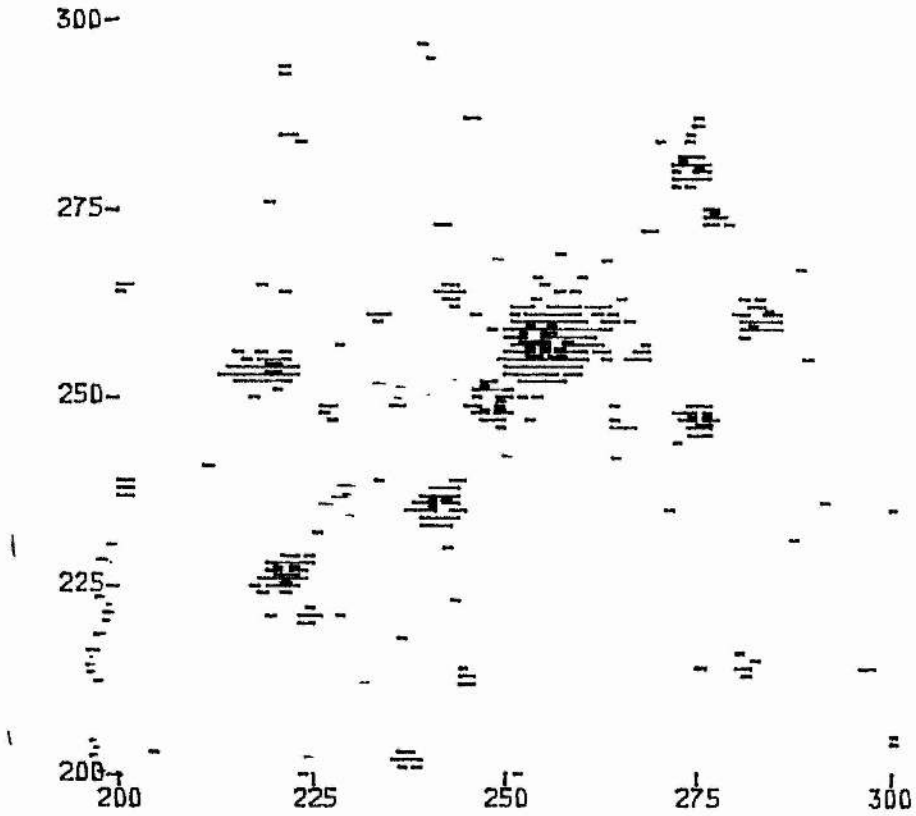

Figure 3.13: Example of graphical display: An "isodensitracing" of a small region.

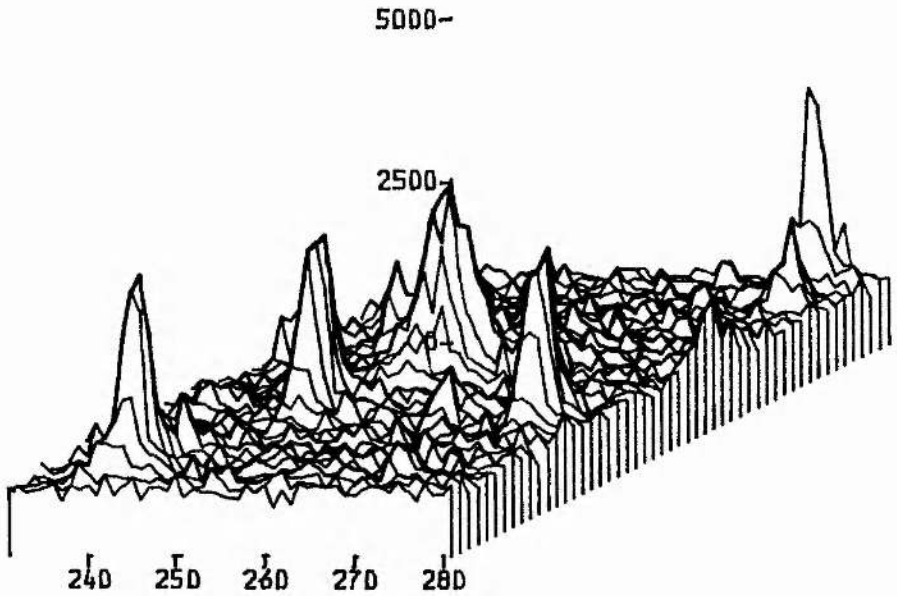

Figure 3.14: The same data as above using an isometric plot.

is replaced by a plane fitted by least squares to the perimeter of the box; and (ii) in inner regions where even a small plane region would be an intolerable distortion, each data point within the box is replaced by the value from the same position diametrically opposite the centre - axial symmetry in the image is assumed.

Derivation of Photometric Parameters.

Various reduction techniques have been tried with varying degrees of success. All begin by displaying a section of a scan, and 'boxing' an area of clear sky. The data within is averaged to provide the local sky area, which fluctuates over the whole scan area. Due to prior processing as described, the sky level is always approximately 1.0. Then an individual object is boxed. The box is drawn as wide as possible, depending on neighbouring objects.

The first reduction method tried was to sum the total luminosity, then numerically work down the profile finding the radius at half the total luminosity, i.e. the effective radius.

The idea failed because (a) the total luminosity was not found - since no extrapolation correction could be determined, (b) the effective radii of small objects are still not properly resolved after processing and (c) the number of samples in an object is so small that the effective areas often turned out to be 1,2, or 3 square units - a sampling quantum effect destroyed the determinations.

The other main scheme finally rejected was to use the standard intensity profile for elliptical galaxies:

$$\log I/I_e = -3.33[(r/r_e)^{\frac{1}{4}} - 1]$$

where I_e and r_e are the effective intensity and radius. A

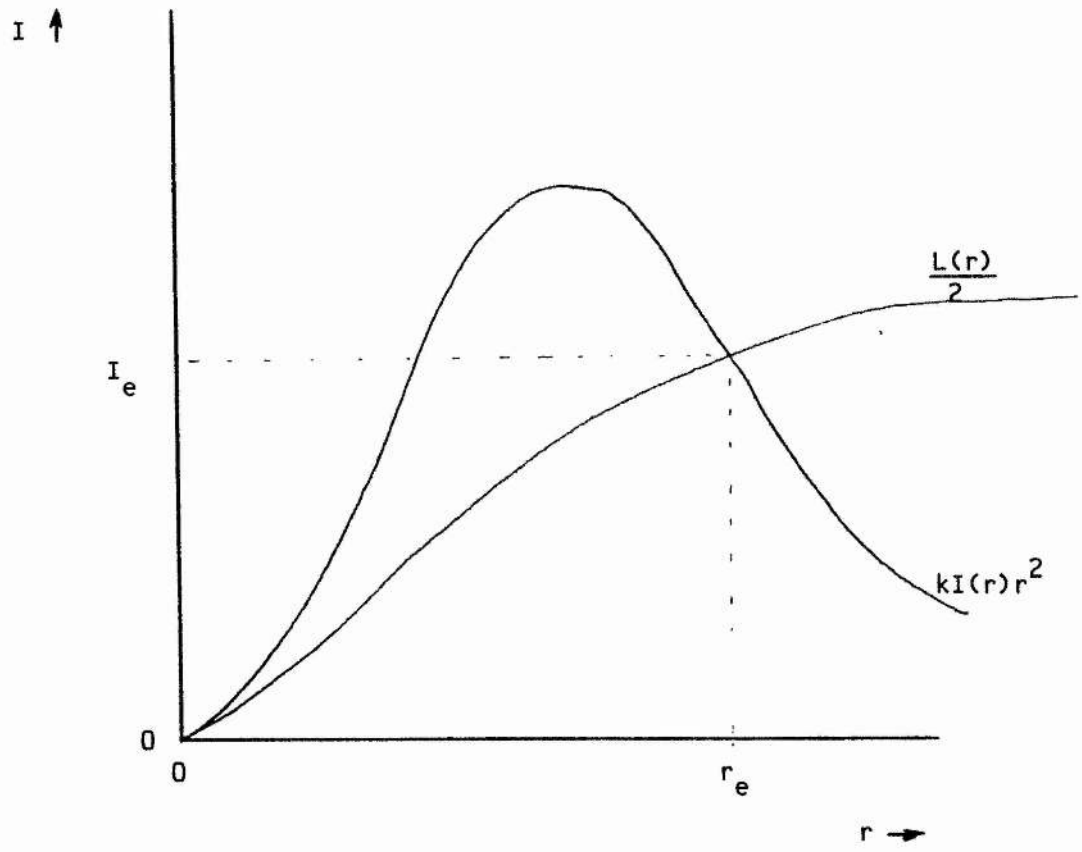

Figure 3.14: Scheme for deriving total luminosity by use of de Vaucouleurs' law for ellipticals.

plot of 0.5 x L(r) superimposed on a graph of $kI(r)r^2$, where k is a constant derived from integration of the above equation to infinity, gives two curves which intersect at the origin and at the effective radius and intensity, since $L(\text{total}) = kI_e r_e^2$. The constant could also be derived from observational material of nearby ellipticals. Schematically, the results in a 'good' case are shown in fig. 3.14. The scheme looked quite promising but again failed due to lack of resolution at and within the effective radius.

V26 Magnitudes.

The V26 magnitude of an object can be defined as:

$$V26 = -2.5 \log \iint I(\geq I26)\ (x,y)\,dxdy$$

where I26 is the intensity corresponding to 26 magnitudes per square arcsec. Similarly the V26 radius can be defined as:

$$r(V26) = \left[\frac{1}{\pi} \iint dxdy(I \geq I26)\right]^{\frac{1}{2}}$$

where dxdy(I≥I26) is the area of a surface element whose intensity is greater than I26.

Operationally, the above definitions must be modified: (1) the integration is performed over a finite box defined such as to be as small as possible to exclude neighbouring objects but so that all $I(x,y) \geq I26$ is included; (2) Noise in the data must be accounted for. Even when the high frequency noise has been filtered, mid and low frequency noise will be present. The problem and its adopted solution is perhaps best explained by reference to a diagram. Figure 3.15 shows a simulated one-dimensional object. Summing directly all

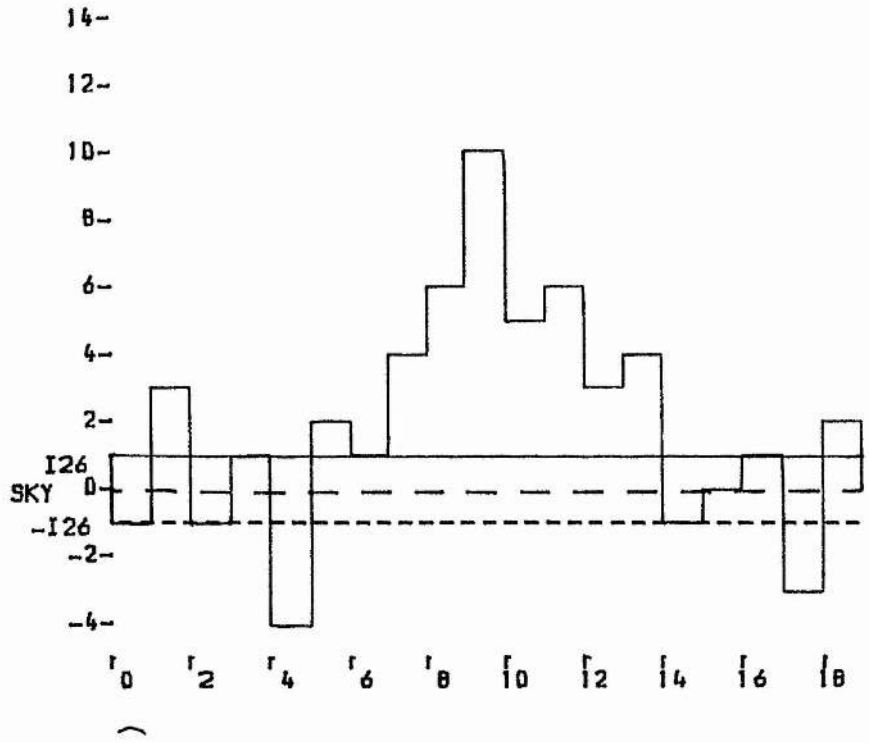

Figure 3.15: V26 simulation to demonstrate noise compensation.

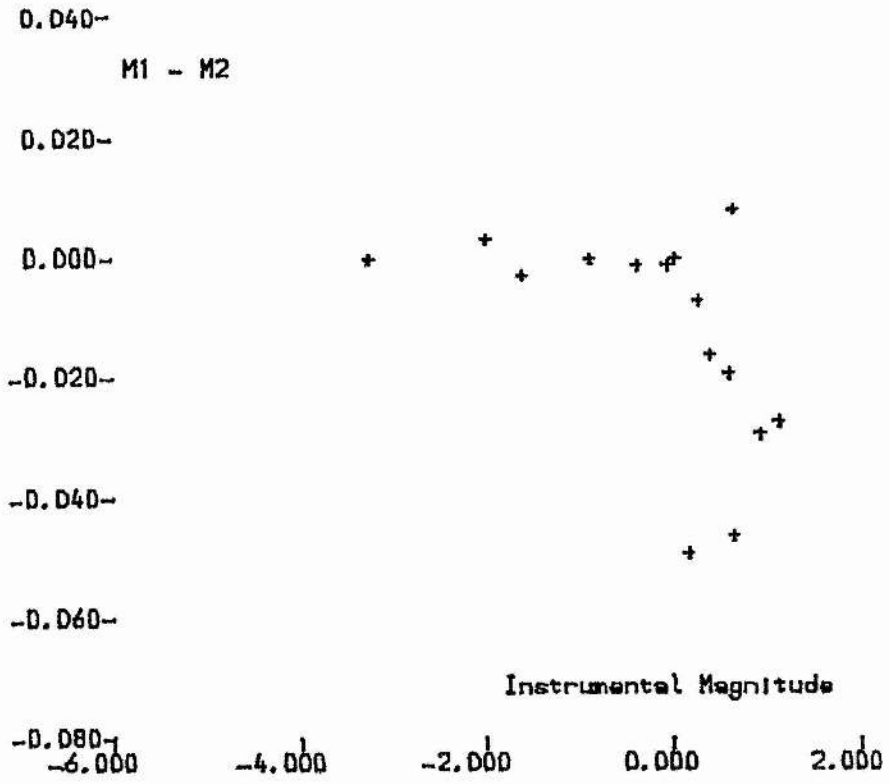

Figure 3.16: Effect of inaccurate z on V26 determination

intensity >I26 gives L = 45 units. However the summation has included any noise spikes which happen to be brighter than I26. If it is assumed that the noise is normally distributed about mean sky level, then the contribution of positive noise can be estimated by summing all negative points below -I26. In the diagram this gives L(<-I26) = -7 units. L26 is then taken to be 45 - 7 = 38 units. Similarly, the total isophote area initially adds up to 10 units; by subtracting the number of points whose intensities lie below -I26, the resulting A26 is 8 units.

In practice, the main difficulty is in setting the level of I26. First, the data must be calibrated in the manner already described; then the I26 intensity must be taken outside the galaxy and redshifted to the distance of the cluster. Galactic absorption is obtained by the method given in RC2 (de Vaucouleurs 1976); the K-correction is taken from Pence (1976). Since at the time of measurement the redshifts of the clusters were only known to lie somewhere in the range .12 < z < .16, an experiment was performed on some of the data to test what effect this had. The result is shown in figure 3.16. Fifteen images were reduced using z = .12 and again with z = .16. The difference in resulting magnitudes is shown plotted against the magnitude for z = .12. As can be seen, the effect is very small indeed for $m_i < 0$ (corresponding to V = 21.5) with rather more scatter at fainter levels. The worst case, however, is still only a twentieth of a magnitude in error.

Repeatability of Magnitude Determinations.

The only colour in which two plates were available was B; thus, to test the stability of the calibration and reduction system, "B26" magnitudes were derived for cluster 1 on two B plates. The

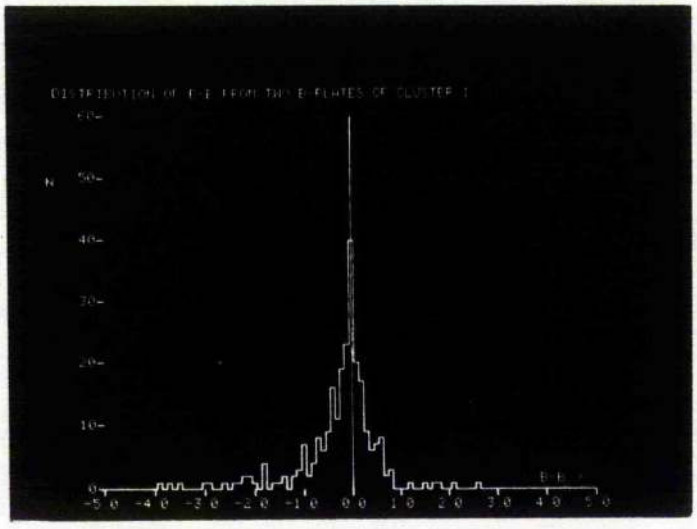

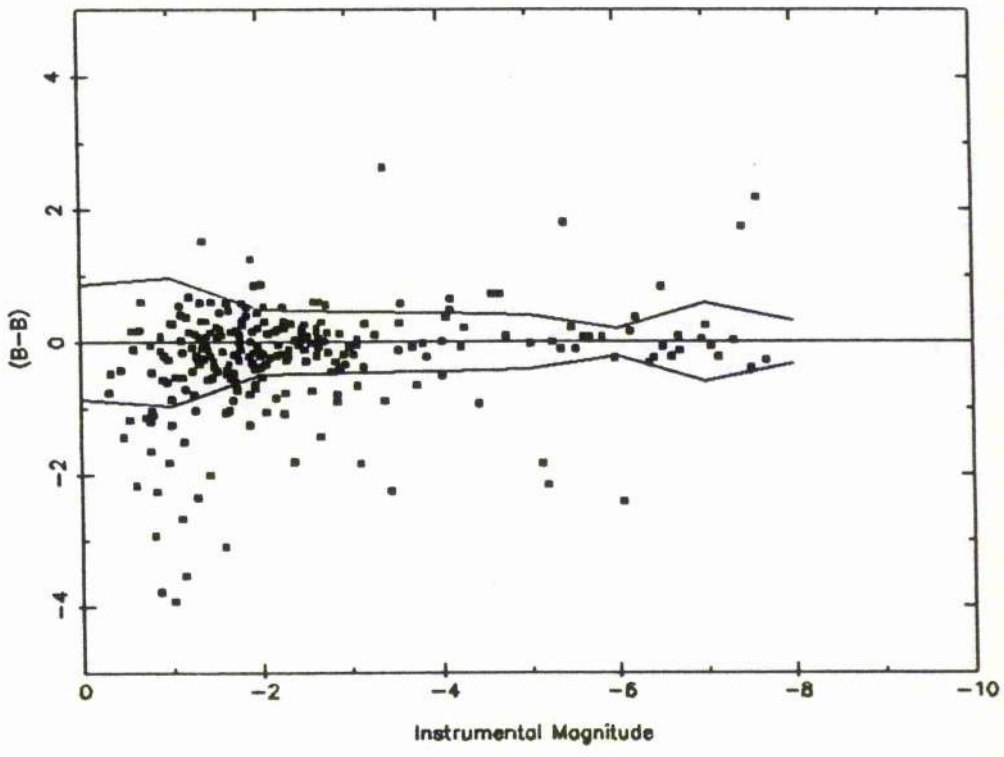

Figure 3.17: Comparison of magnitudes derived from two different B plates. Top - histogram of magnitude differences: σ = 0.4 magnitudes. Bottom - magnitude differences as a function of instrumental magnitude, m_i, where $B \approx m_i + 22.0$. The 1σ envelope is shown.

comparision of the results is shown in figure 3.17. The scatter compares favourably with similar photographic results, for example Dressler (1978). The overall standard deviation (σ) of the distribution is 0.4 magnitudes. As a function of magnitude, σ increases slowly with decreasing brightness except at the very faint end, where differences in plate limits become important. The mean is essentially zero, and bearing in mind that each plate was calibrated separately, this result confirms the validity of the photographic calibration procedure.

Colours.

Because isophotal magnitudes refer to different extents of an object for different colours, the luminosity within a standard central aperture is derived. The aperture used has an effective diameter of 4.5 arcsec. This value was arrived at by operational constraints as follows: D had to be > 2-3 arcsec so that image smearing effects would not affect the result; D had to be < 6-10 arcsec otherwise overcrowding would occasionally invalidate results; and finally within these limits it was convenient to use an area of 9 square raster units, which leads to the above effective diameter.

Colours are then derived later by combining the aperture magnitudes.

Image Centres.

Although the location of an image is given to the reduction procedure by its having had a box drawn around it, the box is not necessarily centred exactly on the object. As long as all parts of the box are outside the V26 radius, this does not affect the results. Also the box must be drawn along integral pixel positions; images are

invariably placed at non-integral positions. Thus for each image, the weighted mean centre is derived, defined as:

$$X_o = \frac{\Sigma I(x,y)x}{\Sigma I(x,y)}$$

$$Y_o = \frac{\Sigma I(x,y)y}{\Sigma I(x,y)}$$

In fact, for a galaxy with no features such as dust-lanes, and with either constant or axially-symmetric mass to luminosity ratio, X_o and Y_o corresponds to the direction of the actual centre of mass of the system.

Storage of Data.

One more parameter per object, the value of the pixel with the maximum intensity, is also derived. It was hoped to use it in star/galaxy separation, but unfortunately as it depends on only one data point, it was found to be a very imprecise parameter.

To summarise, for the image of every object in a scan, the following parameters are derived:

V26 (for V plate scans)
r(V26) - the radius of the V26 isophote
X_o, Y_o - the image centre
I_{max}
M(a) - the magnitude within a 4.5 arcsec aperture.

As each object is analysed, its parameters are stored in a catalogue on disk. The catalogues can (usually) hold ten

floating-point (32-bit) quantities per entry, the current number of entries is kept and a string of up to 38 characters is allowed as a title. Routines have been produced to plot any pair of parameters on a scatter diagram, either normally or logarithmically, and the scan can be mapped by plotting a circle at the x,y positions of the objects using either the V26 radius or setting the radius proportional to the logarithm of the luminosity. These reproduce quite well the appearance of the original scene.

Catalogue utilities include the capability of sorting by any chosen parameter, deleting a particular entry and hard-copy listing.

It is easy to extract a particular parameter or combination of parameters for subsequent analysis.

Collation.

Having reduced scans for a particular cluster in UBVR, the next problem is to determine colour indices from the aperture magnitude. A pair of catalogues of reduction, say in B and V, will not only be in different order but, especially at the faint end of the magnitude range, there will be some objects appearing in one but not the other. In fact, in the knowledge that collation would occur, even the smallest images were analysed since any that were actually noise fluctuations would have no match in the other colours, and so could be rejected.

When scanning the plates on the Joyce Loebl, a particular plate is oriented such that the nearest plate edge to the field to be scanned is placed nearest the pillar, to allow sufficient room for movement. This procedure means that not all scans have the same orientation. However, any rotation is always a multiple of 90 degrees, so it is very easy to transform the coordinates to a different aspect.

To determine any rotation, two catalogues are displayed side by side and inspected. In practice, the orientation of the V scan was taken as standard. When the two scans are at the same orientation, they are sorted into increasing x-position using a fast "Shellsort" routine. This is to facilitate both automatic and manual searching.

A routine was written to use the cross-hair cursor to find the catalogue number of a particular image. The cursor is manoeuvred to the centre of the image's representative circle and a key struck. The routine then finds the catalogue object with co-ordinates closest to the cursor co-ordinates. The result of the search is marked by a "+" for visual confirmation. In this way, the image of the same object in each catalogue can be matched. The catalogue number of an object in the left-hand catalogue is stored in the corresponding entry in the right-hand catalogue.

The procedure could be used to collate every object, and indeed was so used in the analysis of the short-exposure plates. However, for the deep plates some catalogues would have 1200 objects within them, and the task was impracticable.

Instead, 10-20 objects were collated manually, in order to determine the rotation and translation between the two scans. Since the residual rotation was obviously quite small (in fact, it was found to be never more than 1 degree), the small-angle approximation holds, i.e. $\sin x = x$ and $\cos x = 1.0$. Then it is found that plots of Y against X and X against Y are linear, where X and Y are the differences in coordinates of the same object from each catalogue. The data are fitted by a linear least-squares solution, from the results of which the coordinates of one scan can be transformed into the coordinates of the other. Now the main search routine moves consecutively through the left-hand catalogue, transforms each pair of co-ordinates, and

searches the right-hand catalogue for the nearest match. If a match is found within 7 arcsec, it is counted as a "hit". Often if there are for example a close pair of objects in the left-hand catalogue but only a single image in the right-hand, the single image is hit twice. Such an event is flagged, and in that case the situation is reversed: the left-hand catalogue is searched for the nearest fit to the left-hand's coordinates.

The benefit of having sorted into increasing x-position is that an object being searched for will be close to the last object to be found. Thus only a small portion of the catalogue is searched each time, a marker for the next search region being updated whenever an object is found.

After using this procedure, several hundred coordinate pairs are available, and so the solutions for rotation and translation are re-run. It was found that, although the solutions change slightly and the standard errors improved dramatically, on re-running the collation procedure the difference in the number of hits was only one or two. However, no check was made to see if the matches were still the same as from the first run. Incidentally, a typical root-mean-square deviation in the linear least-squares solution was 1.7 arcsec; this represents the expected deviation in position of an object as measured by the weighted-mean centring routine between two scans.

The contents of the V catalogue are collated with R,B, and U. Initially, corresponding catalogue numbers are stored into the V catalogue. At a later time, actual derivation of colours takes place, and a master catalogue is generated containing the original information of the V catalogue plus V-R, B-V and U-R colour indices.

At this stage, spurious entries are eliminated. An object is deemed to exist if it appears in both the V list and at least one other

colour. Any object not fulfilling this criterion is deleted.

Automatic Separation of Stars and Galaxies.

Since it is impracticable to manually identify each image as either a star or a galaxy, some preferably simple combination of the available data is sought as a criterion to automatically separate the two classes of object.

Visually, one identifies the "fuzzy" images as galaxies and the "point-like" images as stars. The quantitative analogue of this criterion is that images with a low luminosity/radius ratio are galaxies, and those with a high ratio are stars. After reduction, magnitudes and V26 radii are available for all the objects. Figure 3.18 shows a plot of the V26 radius vs instrumental magnitude from the V catalogue of cluster 1. Although this diagram shows 1200 points, the division of the two trends is set by visually identifying a small number of images. After choosing a divider, the criterion can be checked against a print by using a display such as figure 3.19. Those objects above the line in figure 3.18 are classed as galaxies and those below as stars; in figure 3.19 the "galaxies" are plotted as circles with their V26 radii, and the stars are plotted as pentacles proportional in size to log luminosity. In fact, it can be seen that the automatic separation must be monitored; the large circle to the right of centre is in fact a star; this star, though, is of magnitude 12.12 in V (it is star No.1 in the photo-electric sequence) and is saturated; because it has a flattened top, the shape of its image is galaxy-like according to the separation criterion. Since such cases are very few in number, they are handled individually. Also, as can be seen, the two trends are not completely separate, and some objects near

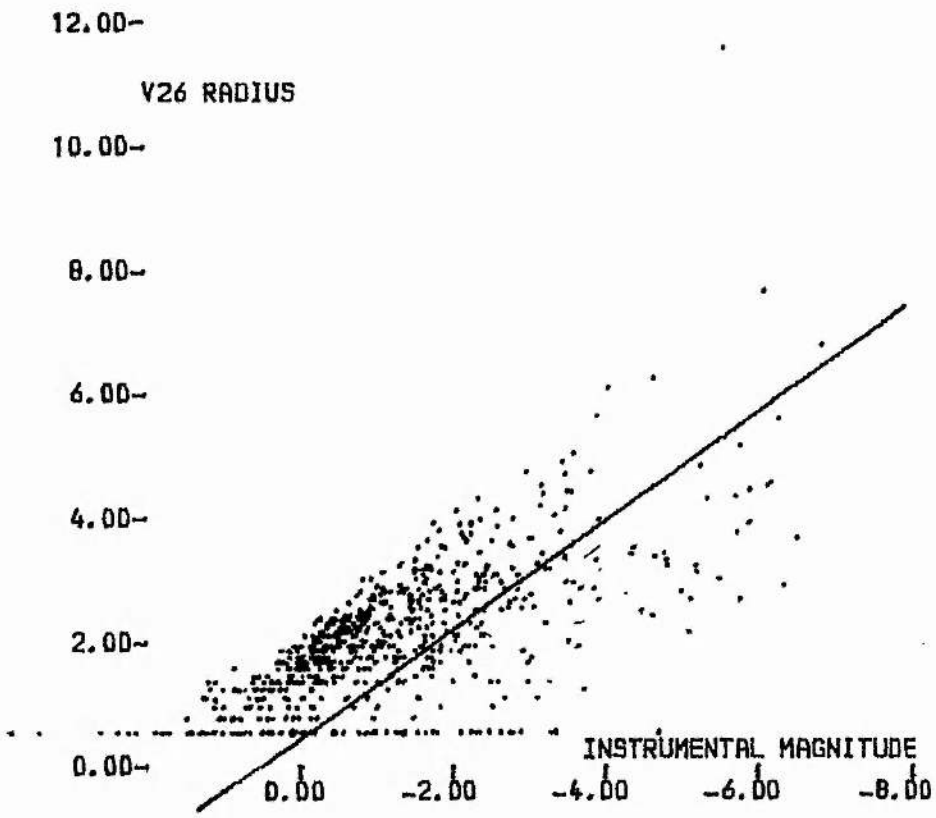

Figure 3.18: Star/galaxy separation.

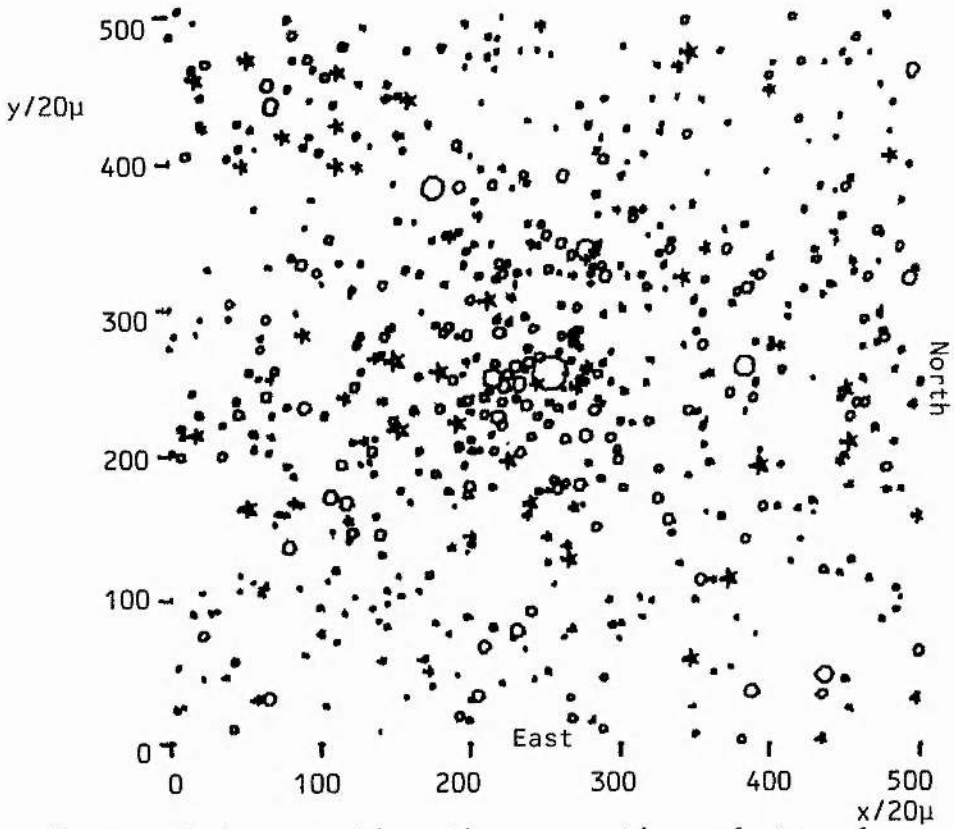

Figure 3.19: Cluster 1 demonstrating the separation of stars from galaxies.

the borderline will be mis-identified. However, if the line is in the best mean position, the gains should equal losses on both sides. Since by definition this traffic consists of images of very similar characteristics the overall statistical results will be unaffected.

The quantisation towards small radii is caused by the fact that the area of the V26 isophote is always an integral number of samples; the smallest permissible area is one sample, leading to a radius of 0.56 sample steps. The next largest radius is 0.78 steps.

Field Corrections.

The difficulty in separating a cluster of galaxies from the general field in which it is apparently embedded is one of the major problems in this work. Strong fluctuations in the number density of background galaxies and practical limitations on the area which can be studied make it very difficult to infer accurately the contribution of background counts in the vicinity of the cluster.

Oemler (1974) concludes that there is no advantage in determining the background correction in the immediate vicinity of each cluster. He derives a combined mean background relationship from regions near several clusters supplemented at the bright end with counts in a few fields by Zwicky. Dressler (1978) has checked this result and in the main uses Oemler's field distribution in his work. Therefore, background corrections for this present study are taken from Oemler's (1974) figure 2, using his quoted relation $J = V + .35(B-V)$ to transform it to V magnitudes. Of course, this correction is only statistical; a selection of objects representative of the field distribution is being removed, not necessarily actual field objects. In fact, as there is a greater concentration of cluster members than field objects, the objects removed will actually tend to be cluster

members. However, the brightness distribution of remaining objects should be very similar to that of 100% true cluster members.

CHAPTER IV

Plate Digitisation and Data Reduction on the Automatic Plate Measuring Machine.

Introduction.

APM uses a different philosophy to that of the Joyce-Loebl style of scanning and reduction. The Joyce Loebl microdensitometer produces accurate densitometry by using projection optics and a mechanical aperture to define a very precise "spot" and converting the optical transmission through the plate within the aperture into density by balancing the transmission through a pre-calibrated density wedge using a mechanical servo. The plate-holding table is stepped to each sample position and halted each time. This results in very slow operation (about 3Hz). An advantage of this slow speed is that the scanning of an area of plate can be run by a background task in the control computer which stores the raw data for later reduction, and may meanwhile be used simultaneously for other computing tasks.

The APM is designed with whole plates in mind. To achieve the implied speed, a flying spot is used. Sampling is effected by deflecting a laser beam with an acousto-optic deflector over a two-millimeter scan line divided into 256 pixels at 7.5 micron intervals, and moving the table continuously in the perpendicular direction. The light transmitted by the plate is collected by a low-gain photomultiplier and digitised to twelve bits (0-4095).

Introduction

AUTOMATED PHOTOGRAPHIC ANALYSIS

Only a fraction of the information stored on photographic plates is ever analysed. A single photograph from a Schmidt telescope will record a million images of stars and galaxies in an hour's exposure but may take months to analyse by eye. Automated photographic measurement can produce accurate photometric, positional and shape information of all objects on the photograph in only a few hours. These measurements are unaffected by observer fatigue and are already in a format suitable for further processing by computer.

Automated measurement is a two stage process – the conversion of the fluctuations of transmission of the photograph that make up the image into a grid of numbers (pixels) and the analysis of this digital image by computer. The computer analysis itself may consist of the study of a few images in great detail or the study of the statistical properties of all the images on the photograph. Often these two approaches are combined. All the images on the photograph are measured and objects of specific interest are automatically selected for study in greater detail.

If automated analysis is to match the performance of a skilled observer, the photograph must be digitised with the highest precision and many calculations performed on every pixel.

The Automated Photographic Measuring facility at Cambridge is a fully integrated system designed to be used by working scientists for all types of photographic measurement. It consists of a very fast accurate microdensitometer to digitise the photographs, a series of powerful on-line computers and the software to run the system and analyse the data off-line.

The Microdensitometer

In the past the main limitation in machine measurement of photographs has been the ability to digitise the fluctuations in plate transmission that make up the photograph accurately and at high speed. These problems are overcome in the APM system by using a laser beam scanner to digitise the photograph. This is more accurate and faster than conventional microphotometers.

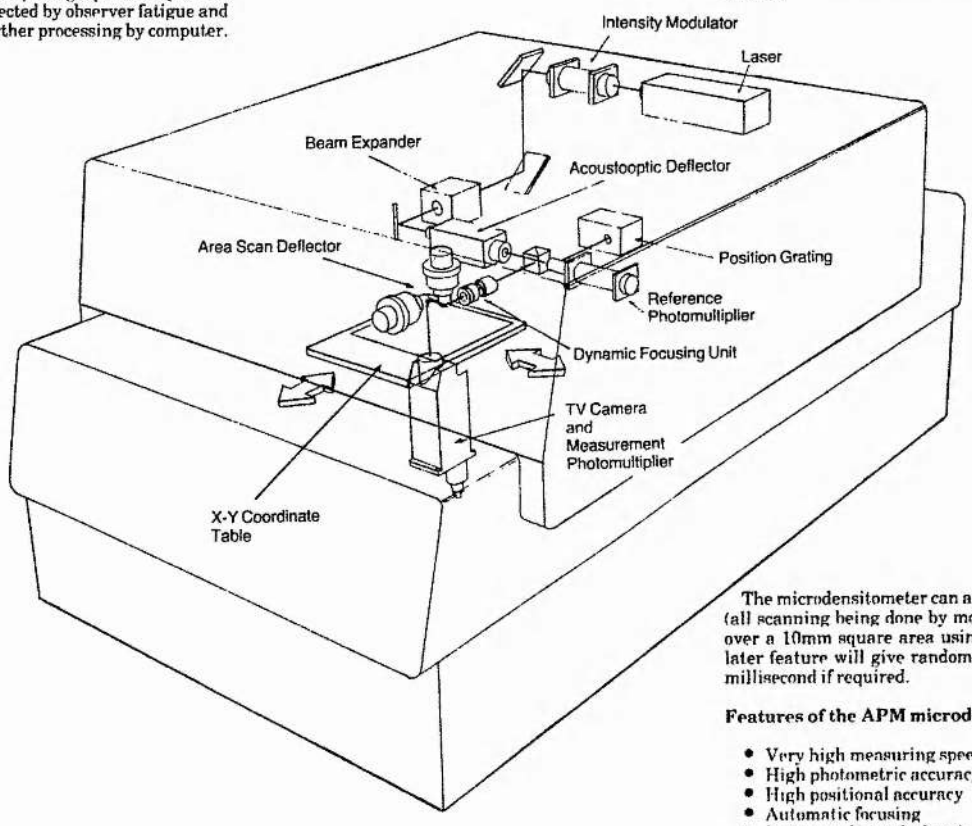

All the energy in the laser beam can be focussed onto the photograph eliminating photon noise problems that arise when conventional microdensitometers are run at high speeds. **Other advantages of the laser beam are:-**

- Small spot sizes
- Gaussian spot profile
- Maximum depth of field
- Accurate Intensity control of the spot.
- Strictly linear microdensitometer response even with small scanning spots

Photographs up to 355mm square are mounted on a massive X-Y table of high thermal inertia to minimise the effects of temperature. An active servo loop is used to continuously control the laser beam intensity to a fraction of a percent. The laser beam itself is deflected over small angles with a non-mechanical scanner which is highly reliable and very fast. Areas of plate are therefore scanned in a series of adjacent strips by moving the laser beam in a linear scan and slewing the photograph under the scanner at a constant speed in an orthogonal direction.

The microdensitometer can also be used with a fixed position scanning spot (all scanning being done by movement of the table) or by moving the beam over a 10mm square area using a precision mirror deflection system. This later feature will give random access capability with access times of a few millisecond if required.

Features of the APM microdensitometer are:-

- Very high measuring speed
- High photometric accuracy
- High positional accuracy
- Automatic focusing
- Reference Point finder giving absolute positions
- Computer controlled Platen rotation
- TV Camera for remote viewing of the photograph

Figure 4.1: This description of the APM microdensitometer is reproduced from a publicity pamphlet published by the APM group.

Unfortunately, the photomultiplier collects not only the light transmitted by the particular pixel but also all the halo of the spot and light scattered by the emulsion. This means that when sampling high-density regions of plates (such as image centres) the measured transmission is higher than it "should" be; i.e. the density measured is lower. The distortion in photometry produced by this feature can easily be calibrated out of stellar photometry since the same thing happens to all similar images; however photometry of extended images is difficult and, in particular, calibrating density step wedges which have large flat areas of density do not relate to the densities measured on the sharply-sloping profiles of stars and small galaxy images.

However, in the context of this work, the individual galaxies in the clusters are of similar dimensions to faint stars, and so photometry calibrated via the photo-electric stellar sequence will be valid.

With a Joyce Loebl the raw pixels are reduced to image parameters using the off-line techniques described in chapter III. Because the APM scans whole or large parts of whole plates, the raw data cannot be kept. Instead a series of on-line special-purpose processors carry out transmission to density conversion, smoothing, image recognition and parameterisation. APM is well described in Kibblewhite, Bridgeland, Bunclark and Irwin (1983) and Kibblewhite, Bridgeland, Bunclark, Cawson and Irwin (1984).

APM Output

Plates are scanned twice; on the first pass, background processing hardware produces histograms of 64 x 64 pixel (0.5 mm x 0.5 mm) areas, and a modal estimate of each histogram is taken as the background value of the corresponding area. A typical 25cm x 25cm scan conveniently

Image Processing Computers

Most other photographic analysing systems use magnetic tape as a temporary storage medium for the raw pixel data before they are processed off-line on a computer. The APM system uses specially designed on-line computers to process the data at the same time as it is being digitised from the photograph This computer consists of a series of hardwired processors which perform standard tasks such as calibration, smoothing background and noise removal plus a fast programmable processor which will compute the positions, shapes and profiles of all images on the photograph or will analyse, in more detail, individual images or objective prism spectra.By using a parallel processing arcitecture a very high speed throughput is obtained - equivalent to 30 million instructions per second

A single astronomical photograph has 2 billion pixels which must be analysed in detail before the properties of the images can be obtained. The APM computer allows this to be done at economic cost.

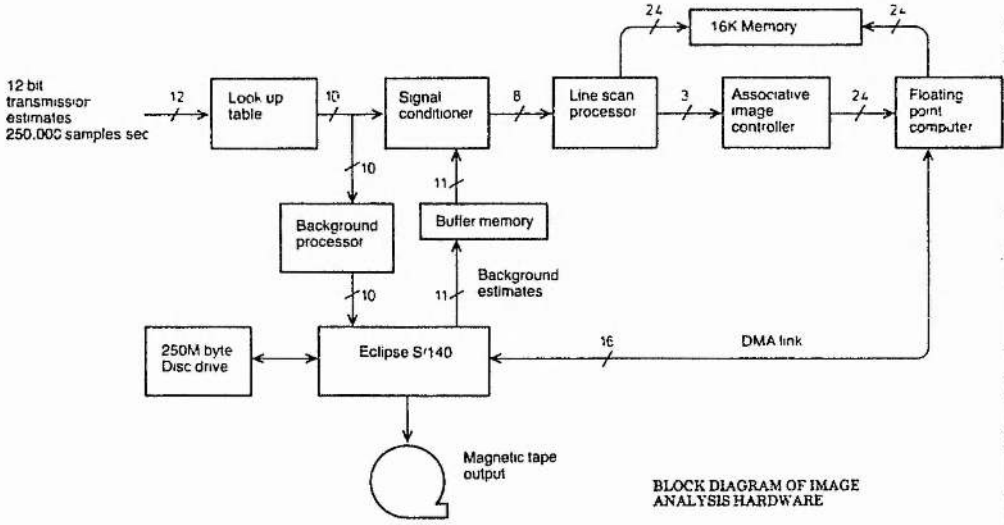

BLOCK DIAGRAM OF IMAGE ANALYSIS HARDWARE

Figure 4.2: Outline of APM image processing hardware.

produces a 512 x 512 point map of raw background values which is filtered and smoothed in the Data General Eclipse S/140 control computer. The resulting global background map is fed back into the scanner during the second pass when an interpolator produces a background value for each pixel position.

On the second pass, the image processing hardware has background-removed data available. A threshold value chosen by the user is further subtracted so that any remaining pixels are potentially part of images. A 'spike remover' recognises regions of connected pixels in groups of usually sixteen or less and rejects them as too small to be genuine images. By now the unwanted majority of the data has been removed. A sophisticated combination of hardware and software then collates remaining groups of connected pixels, assumed to be astronomical images, and computes a series of parameters for each image, defined as follows:

Parameter	Description
1	Integrated intensity (or density, depending on how the hardware look-up table was programmed)
2	The y-coordinate in units of pixel size (7.5 micron) defined as $$Y = \frac{\Sigma y I(x,y)}{\Sigma I(x,y)}$$ where y is the y-coordinate of a pixel and I(x,y) is its intensity;
3	A running count.
4	The x-coordinate, X, defined analogously to y;
5	The second moment in x defined as

Specification Summary

APM MICROPHOTOMETER

X-Y Table

Travel each axis: 355mm
Positional accuracy ± 0.3 micron
Repeatability: ± 0.1 micron
Resolution: ± 0.1 micron
Maximum velocity: 30mm/sec X axis
80mm sec Y axis
Platen Rotation. ± 4°, Resolution 2½ arc second

Laser beam Scanner

Spot Size. 8 micron nominal, 4 micron or 16 micron available
No. of samples scan line. 256
Positional accuracy of sample: ± 0.3 micron
Resolution in transmission: ± 0.025%
Photometric stability. ± 0.002D
Scanning speed. 250,000 samples sec (maximum speed 10^6 samples/sec)

APM SOFTWARE

A full software package is provided for the interactive control of the APM microphotometer and the image processing computer.

Specific features include:

- Automatic orientation of photographs using reference stars from a catalog stored on floppy disc
- Areas up to 355mm square (2 billion samples) scanned in strips 256 samples wide
- 12 bit Transmission measurements converted into true density or intensity estimates via a look-up table
- Digital smoothing of spot to 8,15 or 30 micron in intensity space – this gives increased photometric accuracy for high contrast images
- Background estimated to 0.001D every ½mm over the plate
  Background calculated for evey pixel by linear interpolation
- Small "noise" images can be removed from the data without affecting the real images
- Calculation of accurate positions, integrated intensity, eccentricity and position angle and profile for all descrete images on the photograph

Off-line software for further image analysis includes:

- Image enhancement, contour or grey scale mapping
- Interactive graphics package
- Image classification
- Collation of image parameters from a set of plates
- Automatic detection of images whose properties have moved or changed their brightness over a set of Photographs (e.g. variable, colour excess or proper motion objects)
- Calibration mapping
- Addition or subtraction of digital maps of individual images
- Maximum entropy filtering
- Weiner Filtering

Typesetting & Design: Meridian Typesetters, Stephen Brooks Design Graphic
14d Regent Street, Cambridge, Cambs

Figure 4.3: Specification summary.

$$XX = \frac{\Sigma(x - X)^2 \; I(x,y)}{\Sigma I(x,y)}$$

6 The cross-moment

$$XY = \frac{\Sigma(x - X)(y - Y) \; I(x,y)}{\Sigma I(x,y)}$$

7 The second moment in y defined analogously to that in x

8 The peak intensity of that image;

9-16 The areal profile. The first cut is at threshold, and is simply the no. of pixels with intensity greater than threshold, or the total area of the image. The further seven levels are spaced logarithmically to give good coverage of both faint and bright images at 1, 2, 4, 8, 16, 32 and 64 units above threshold.

Basic Off-line Reductions.

The set of sixteen parameters for each image on the plate are stored on magnetic tape for further use. It has become natural for all APM data to be passed to the local Starlink Node VAX 11/780 (CAVAD::) for routine first-stage processing which is an obvious next step to the scanning phase. Firstly, a programme called SELECT reads APM tapes into the VAX, performs Data General (IBM) floating point to DIGITAL VAX floating point number format, and checks image parameters for validity (against APM malfunction).

Next JOIN merges into a single VAX file the separate sections of a logically single scan; due to hardware limitations, APM can only scan columns 12.5 cm long, so to scan a whole plate requires two or three sections.

Then SORTOUT corrects a problem with APM; because of the difficulty

of edge-matching images which overlap column boundaries, columns are actually scanned with fifty-percent overlap. There is logic to record images only once, but by noise fluctuations an image just touching the edge of a column may be recorded twice, once on successive columns. Also separate sections are overlapped by a column's width, so there is duplication at section boundaries. SORTOUT rejects these spurious copies.

The programme STATS can then take a global look at the whole set of image parameters. The purpose of STATS is to classify images according to whether they are stellar, non-stellar or noise. The criterion for separating these groups is basically that stars are all similar in shape and so lie in a very well-defined region of parameter space; nothing can have a sharper profile than a star, so such an image must in fact be a clump of grains. Anything less sharp than a star is "non-stellar".

SELECT, JOIN, SORTOUT and STATS were written by M. J. Irwin of the APM group, and an example of STATS as applied to plate V2392 used in this project is shown in Figures 4.4 to 4.7. Classification probabilities are combined from each of these pairs of parameters into a final image classification.

Collation.

As with Joyce-Loebl derived data, results from individual plates must be collated. Since APM scans large areas it is necessary to use a more sophisticated mapping algorithm.

Scans of successive plates are each aligned on catalogue stars which means all scans may be started from the same celestial co-ordinates. Therefore different data sets are fairly closely aligned anyway, and the collation program (COLLATE) can automatically search amongst the brightest objects for matches. By choosing the brighter images which are sparsely spaced out, the probability of a miss-hit is

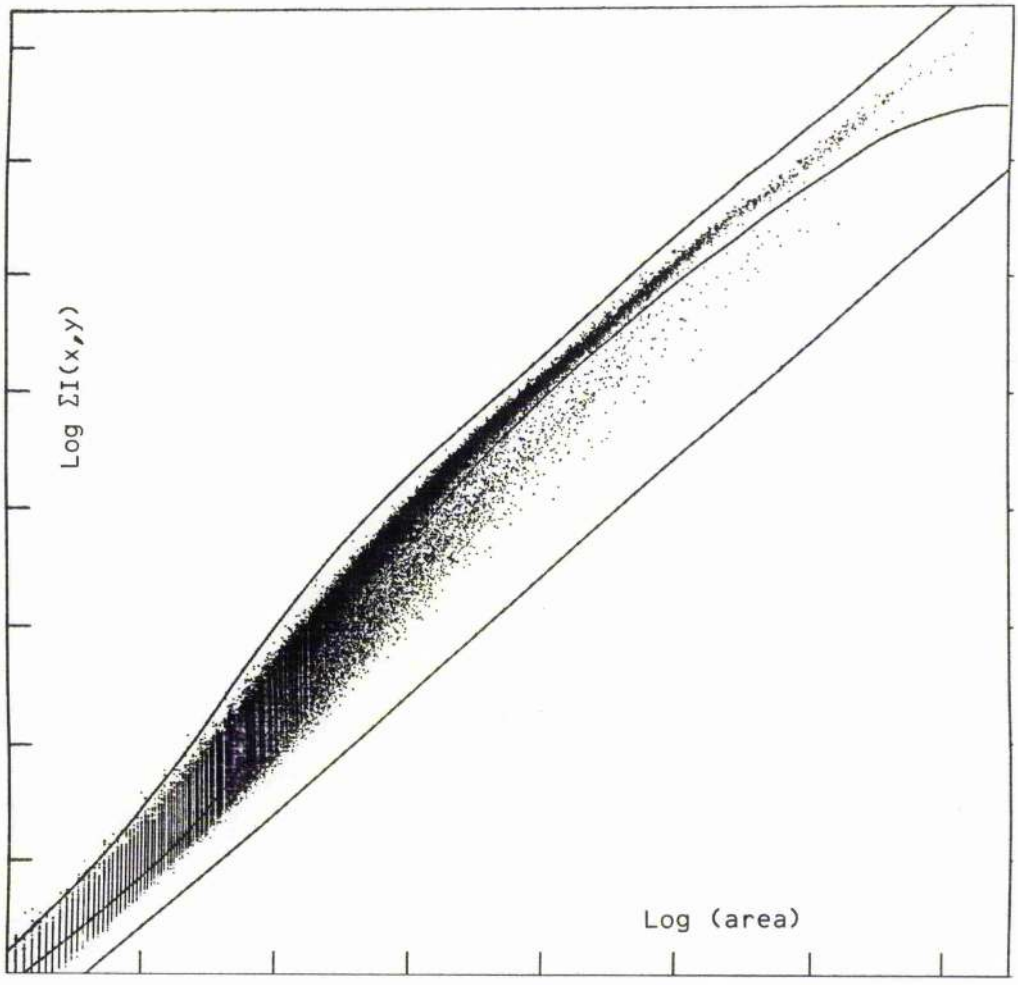

Figure 4.4: Log of integrated intensity (ordinate) plotted against isophotal area. Note the highly defined sequence of stellar images but the confusion at the faint end. Axis tick marks are at magnitude (ie 2.5xlog) intervals.

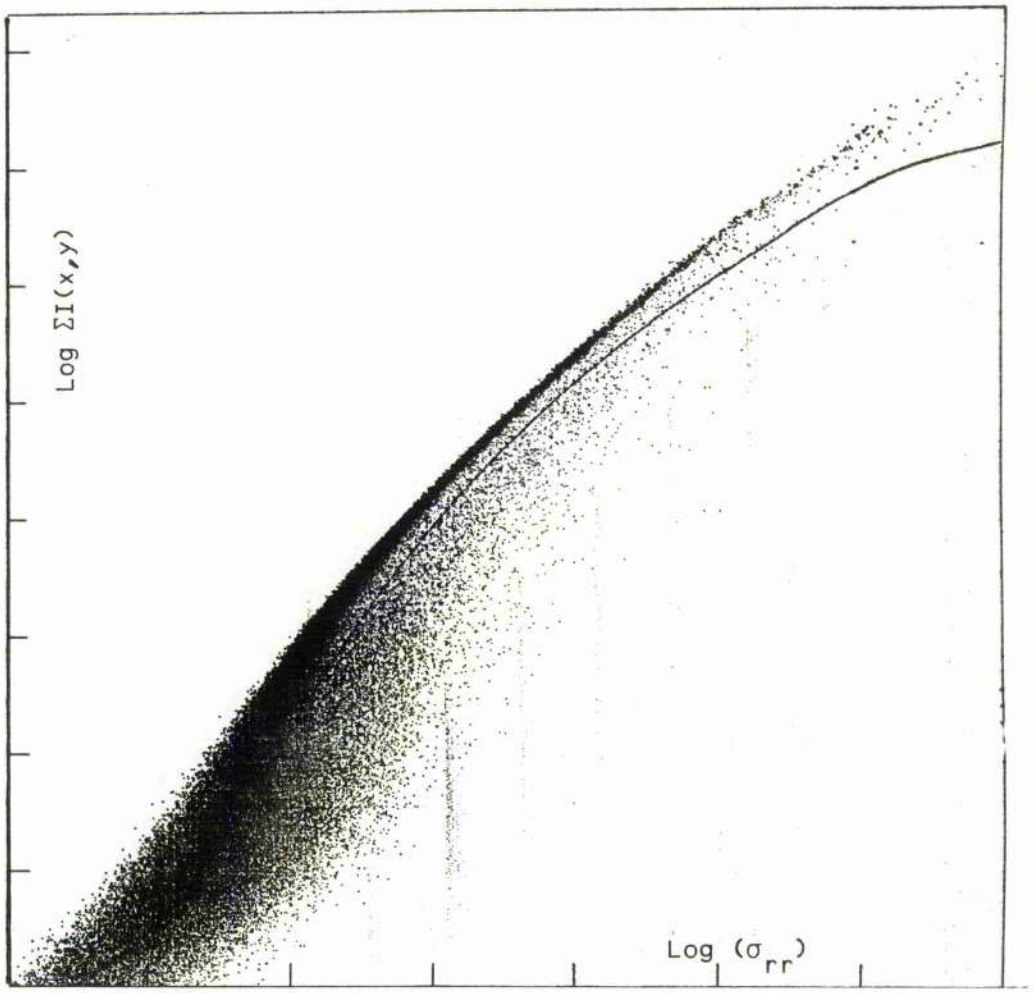

Figure 4.5: Similar to fig. 4.2 except the abscissa is log of total second moment (σ_{rr}).

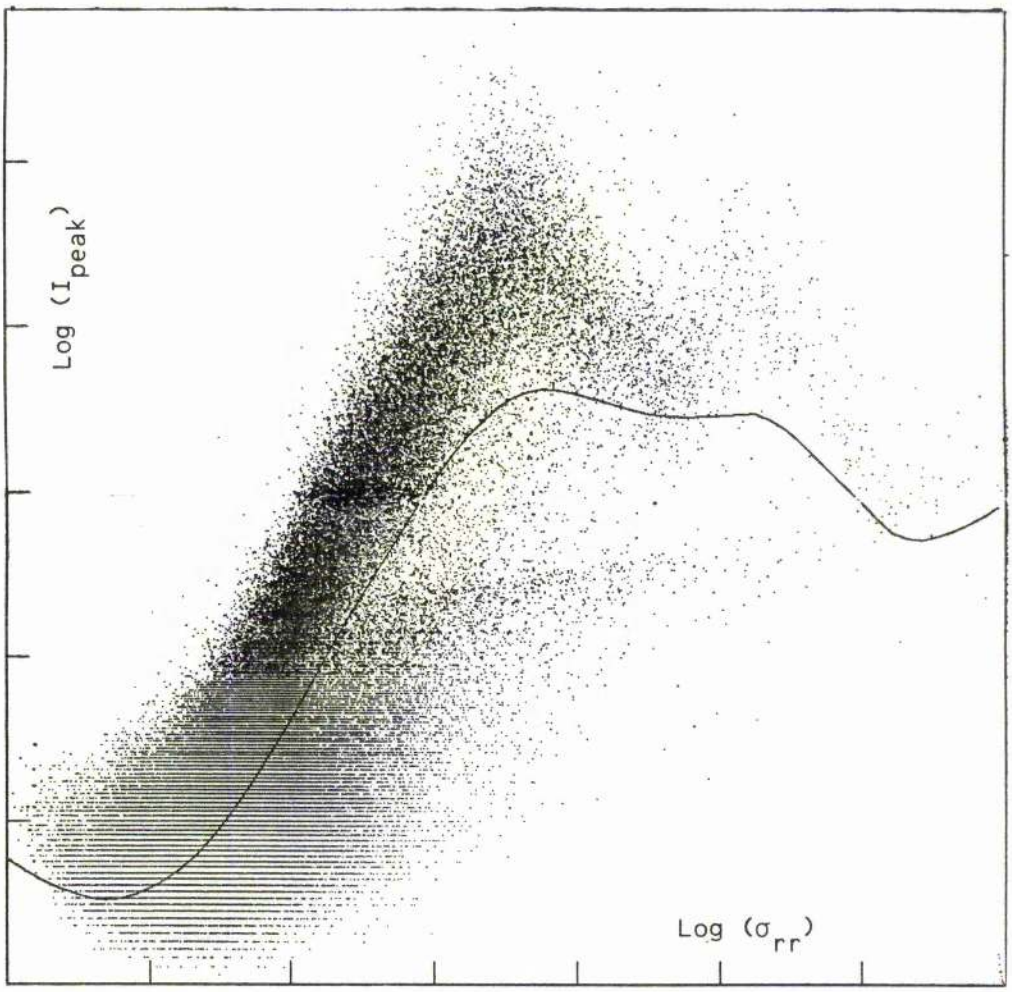

Figure 4.6: Because images saturate at a rather faint limit, the peak (ordinate) ceases to rise with brightness correspondingly early. However this parameter helps separate the faint end.

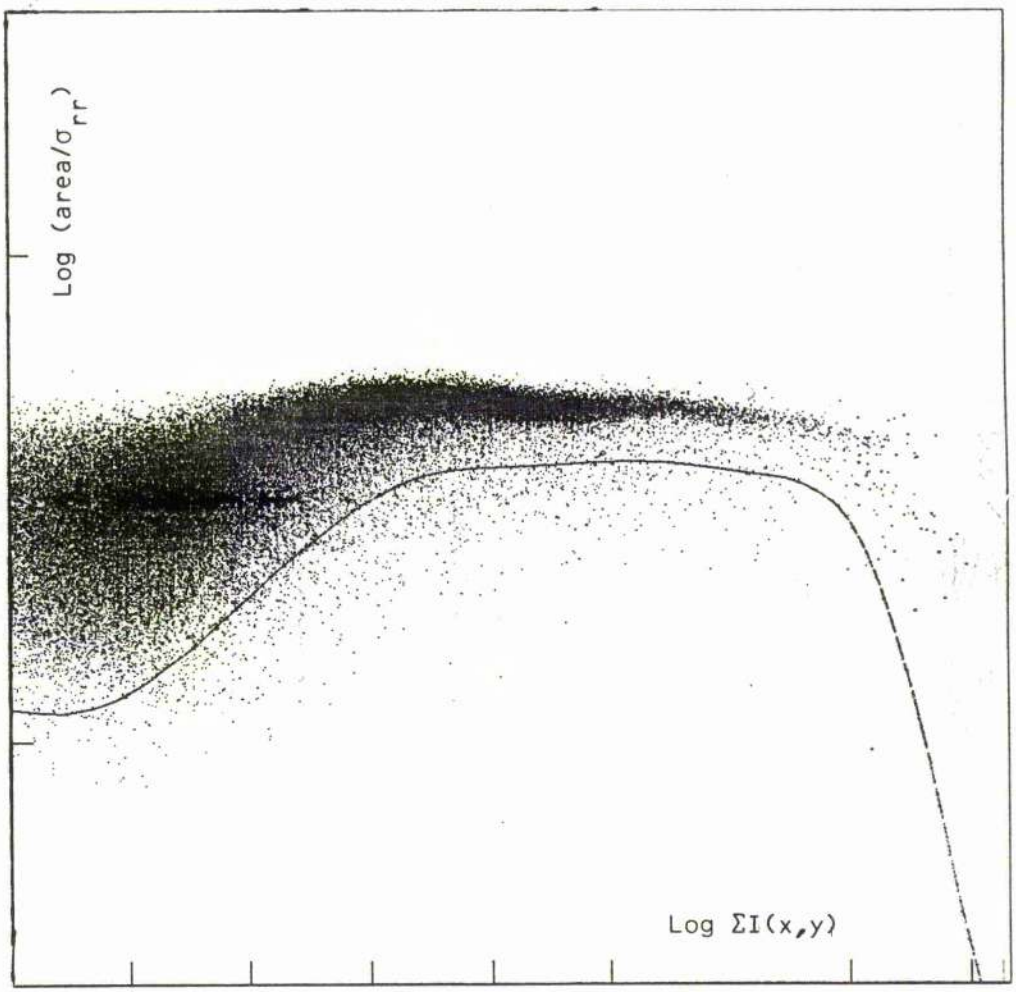

Figure 4.7: Perfectly elliptical images would all lie on a horizontal line in this diagram. It is therefore used as a test of deviations from ellipticity, e.g. the dumbell shape arising when two nearby objects just merge into a single image.

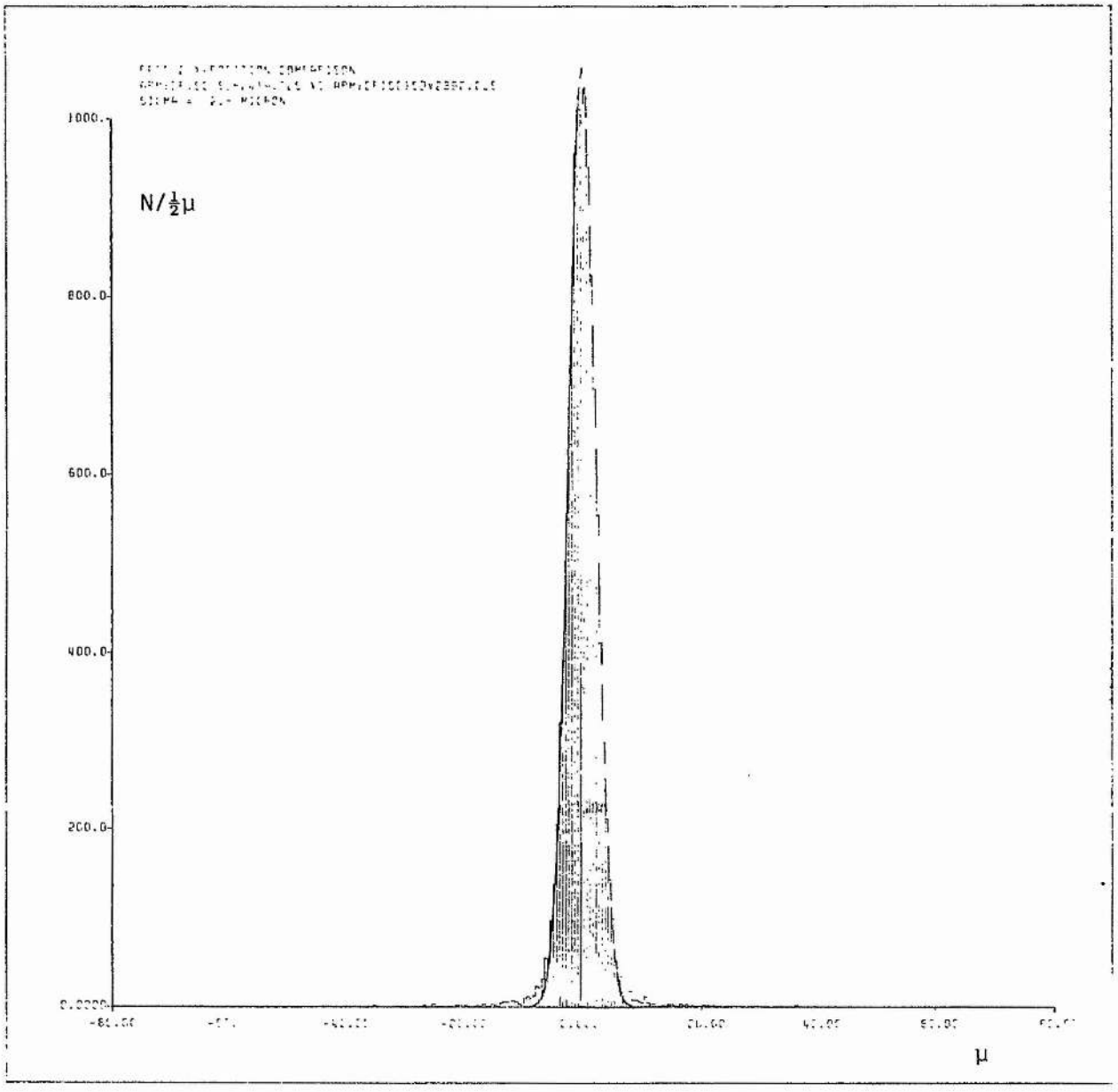

Figure 4.8: Residual errors in x after merging data from V2392 with data from R2419. Note the combined rms residual is 2.3 micron, or 0.15 arcsec.

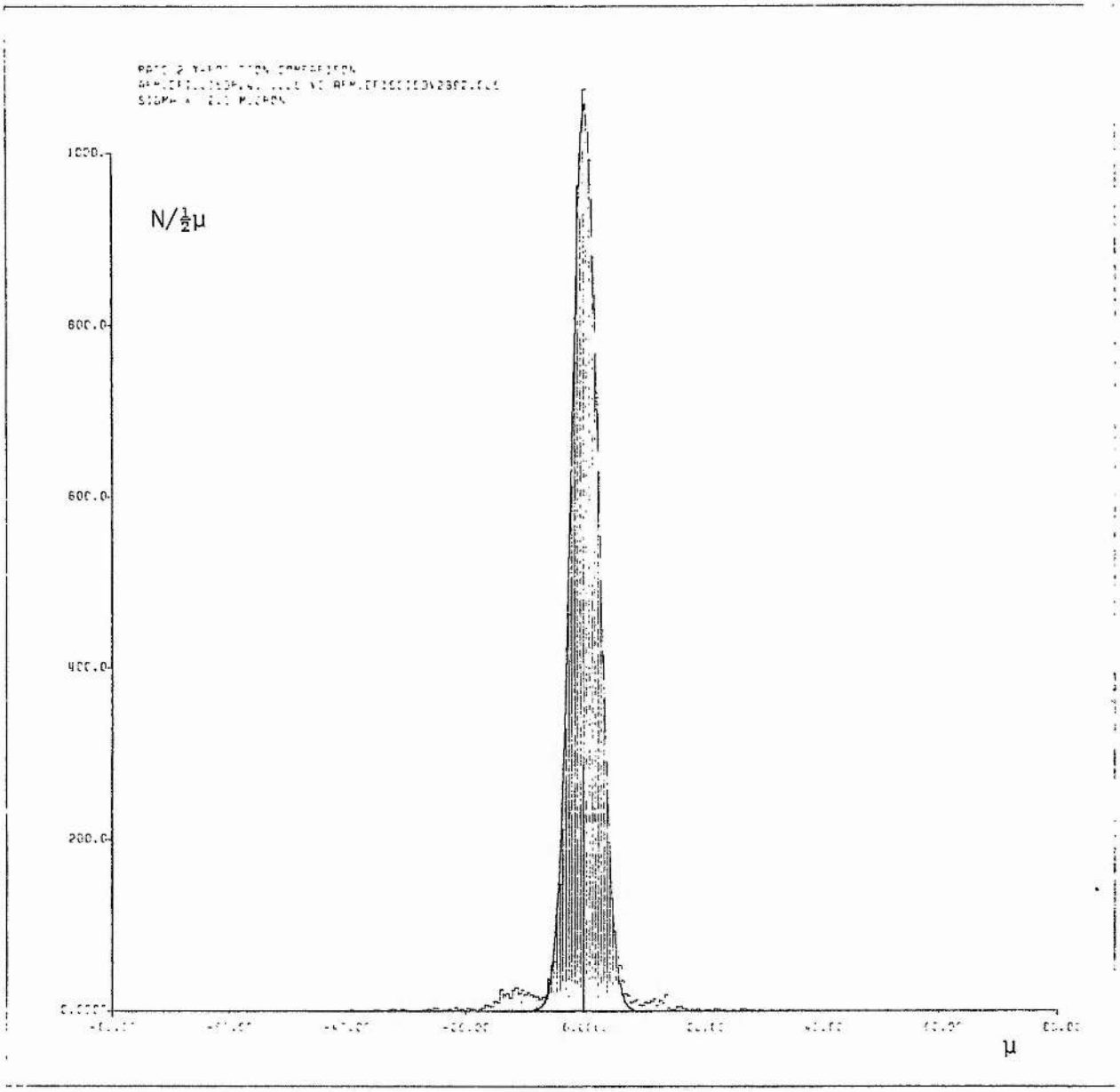

Figure 4.9: As for figure 4.8, but for the y-direction.

low. Then one plate is mapped to the other using relationships of the form

$$x' = ax + by + c$$
$$y' = dx + ey + f$$

where x',y' are coordinates on the second plate, and a, b, c, d, e and f are constants determined by least squares. Now the program has a moderately good prediction of the positions on the second plate and can have a second pass matching all objects and using a second order mapping function:

$$x' = ax + bx^2 + cxy + dy + ey^2 + f$$
$$y' = gx + hx^2 + ixy + jy + hy^2 + l$$

where a through to l are constants determined by least squares. The second-order terms are found to be small but none the less significant. Figures 4.8 and 4.9 show the residual errors for all objects as a result of merging V2392 data with R2419 data. Note the rms error is 2.3 micron, or 0.15 arcsec.

The primary use of collation is of course to enable production of multi-colour photometry but there is a beneficial by-product. By collating a plate with another in the nearest pass band, only images which 'pair up' can be kept, i.e. all spurious images can be rejected. For this purpose U was matched with B, B with V, V with R and R with V. New data files containing only images which collate with ones on this partnering plate were produced, and these files re-submitted to STATS. Using this cleaned up data, STATS is able to produce more reliable star/galaxy separation. A final benefit is that having rejected all noise images the storage requirements are less.

Photometric Calibration.

Using the accurate densitometry of the Joyce-Loebl, it was possible to generate data on a relative-intensity scale, and then directly integrate stellar images so that a linear instrumental/photoelectric magnitude relation was obtained. As noted, APM cannot perform in this way because of saturation problems etc.

The author has developed a method of linearising APM internal magnitudes over a large dynamic range which allows calibration of APM data down to the plate limit using if necessary only a fairly modest photoelectric stellar sequence.

The basic principle is noted in Chapter III, namely that star profiles are intrinsically identical apart from a scale factor. Therefore a calibration curve must be discovered which makes all measured stellar profiles as similar as possible. Whilst something along these lines has been around for sometime, the author has developed it into a demonstrably sound routine which produces values for stars linearly related to actual magnitudes for all plate/telescope/emulsion combinations ever tried.

The heart of the procedure is iterative. Given a calibration curve and a standard star profile, magnitudes could be worked out. Given magnitudes and curve, the standard profile could be computed. Finally, given magnitudes and profile, the calibration curve ensues. So actually, two items are used to calculate the third cyclically, from some first approximations, until no further change occurs.

It is important to obtain the first approximations as globally correct as possible to ensure the iteration converges. This is done by using data as near to sky as possible, where density is approximately linear with intensity. In fact, the areal profile at threshold and that at threshold +1 are used. From a wide range of stars, the quantity

$$\frac{\log I_{t+1} - \log I_t}{r}$$

where I_t and I_{t+1} are the intensities at threshold and at threshold + 1, and r is the radius of a particular star image, gives a value gradient of the logarithmic stellar profile. It has been found empirically that when the inverse of this gradient is plotted as a function of radius, the curve is well represented by a parabola, which can be fitted by least squares. Thus we have:

$$\frac{d \log I}{dr} = \frac{1}{a + br + cr^2}$$

which can be integrated directly to generate a model of the stellar profile:

$$\text{Log } I = (1/cd)\tan^{-1}[(r + b/2c)/d]$$

where $$d^2 = a/c - (b^2/4c^2) \qquad (d^2 \text{positive})$$

Using this curve and having assumed the intensity of the first areal profile, the intensity levels for the other seven areal profiles can be calculated. Magnitude estimates for all stars can be computed and the iteration phase entered.

The technique was first published in Bunclark (1982). Irwin has refined the statistical test for convergence and formalised the rationale of the method, and we have published a definitive description in Bunclark and Irwin (1983).

An example of the internal calibration applied to this work is shown in figures 4.10 to 4.14. In fact, the set of all the stars is divided into 500 bins. The values of parameters for each bin is the median of all images falling in the bin. The median provides a robust modal estimate of the values while rejecting any totally spurious

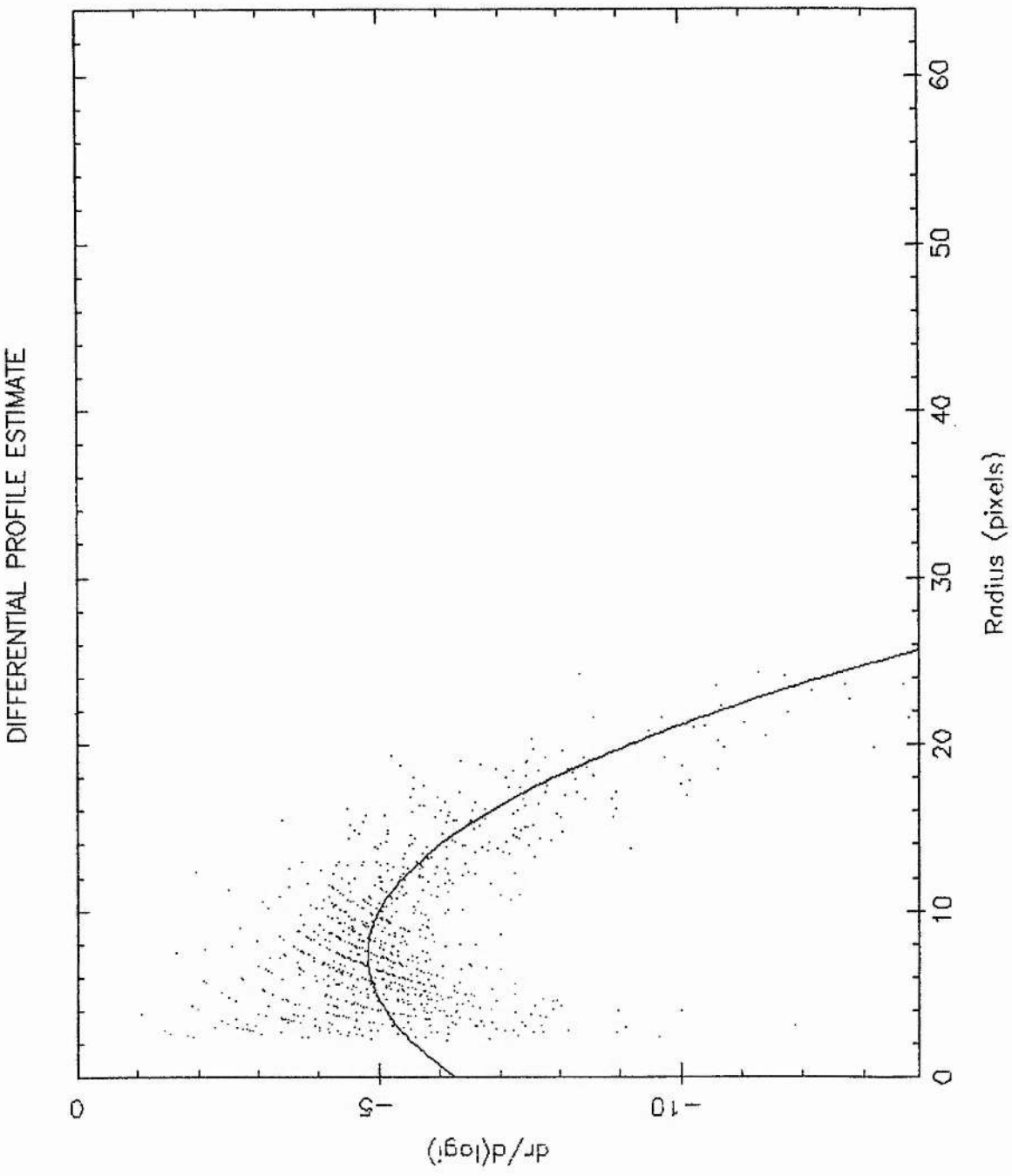

Figure 4.10: Profile gradient values near threshold for each parameter bin.

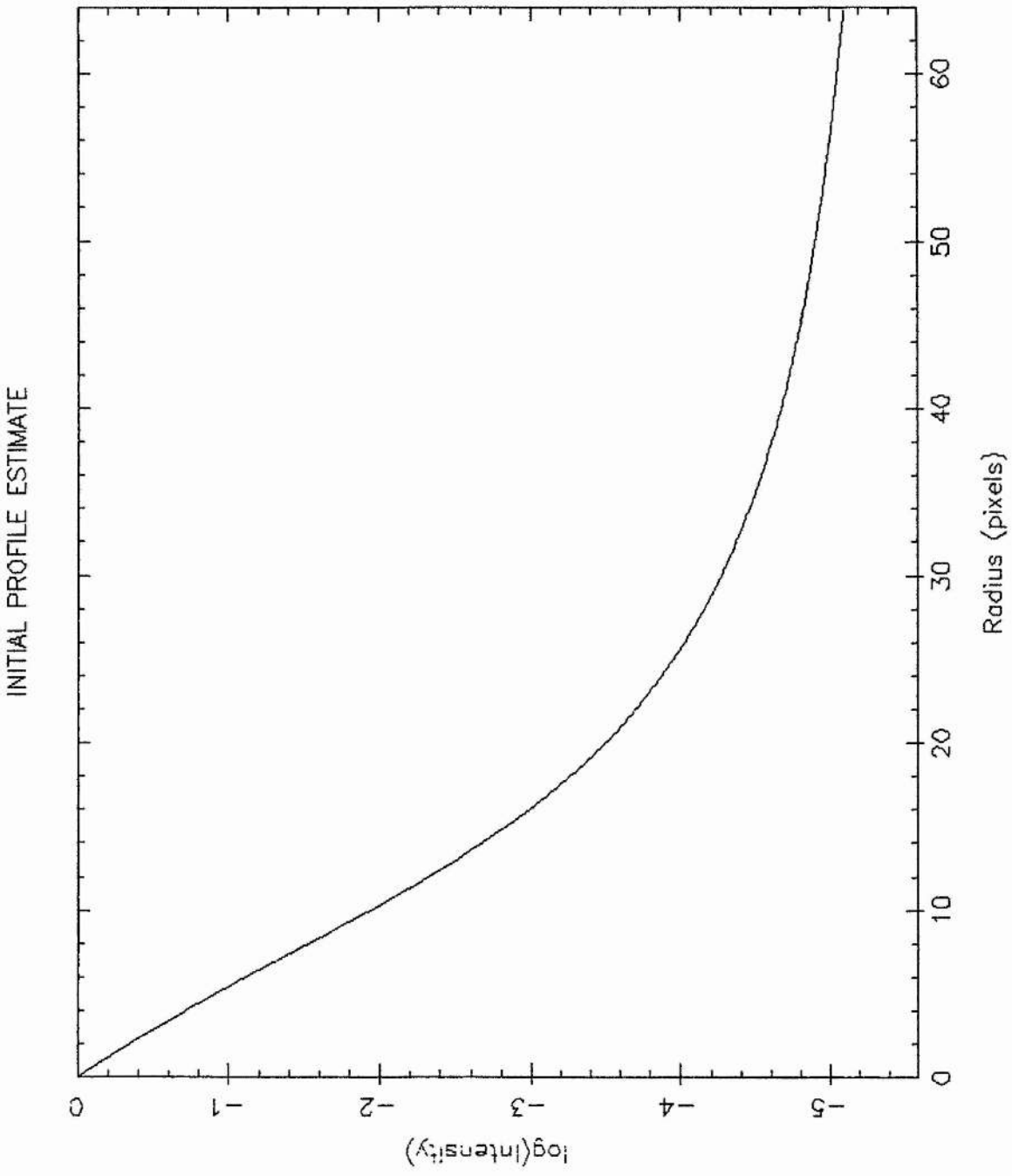

Figure 4.11: Initial profile estimate generated by integrating the inverse of the curve fitted in figure 4.10.

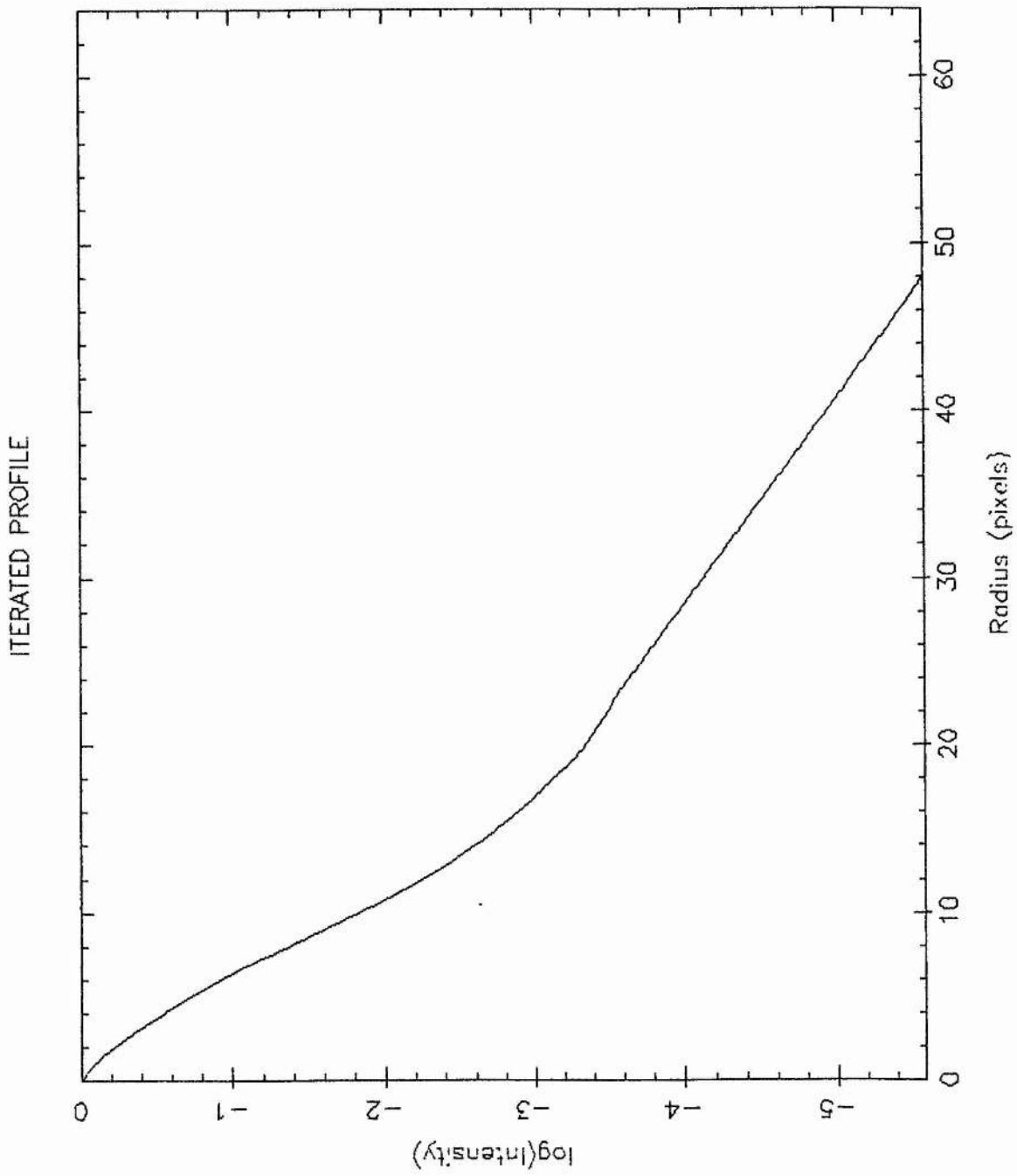

Figure 4.12: Final iterated profile. Note the overall similarity to the initial estimate in figure 4.11, but with small-scale detail added.

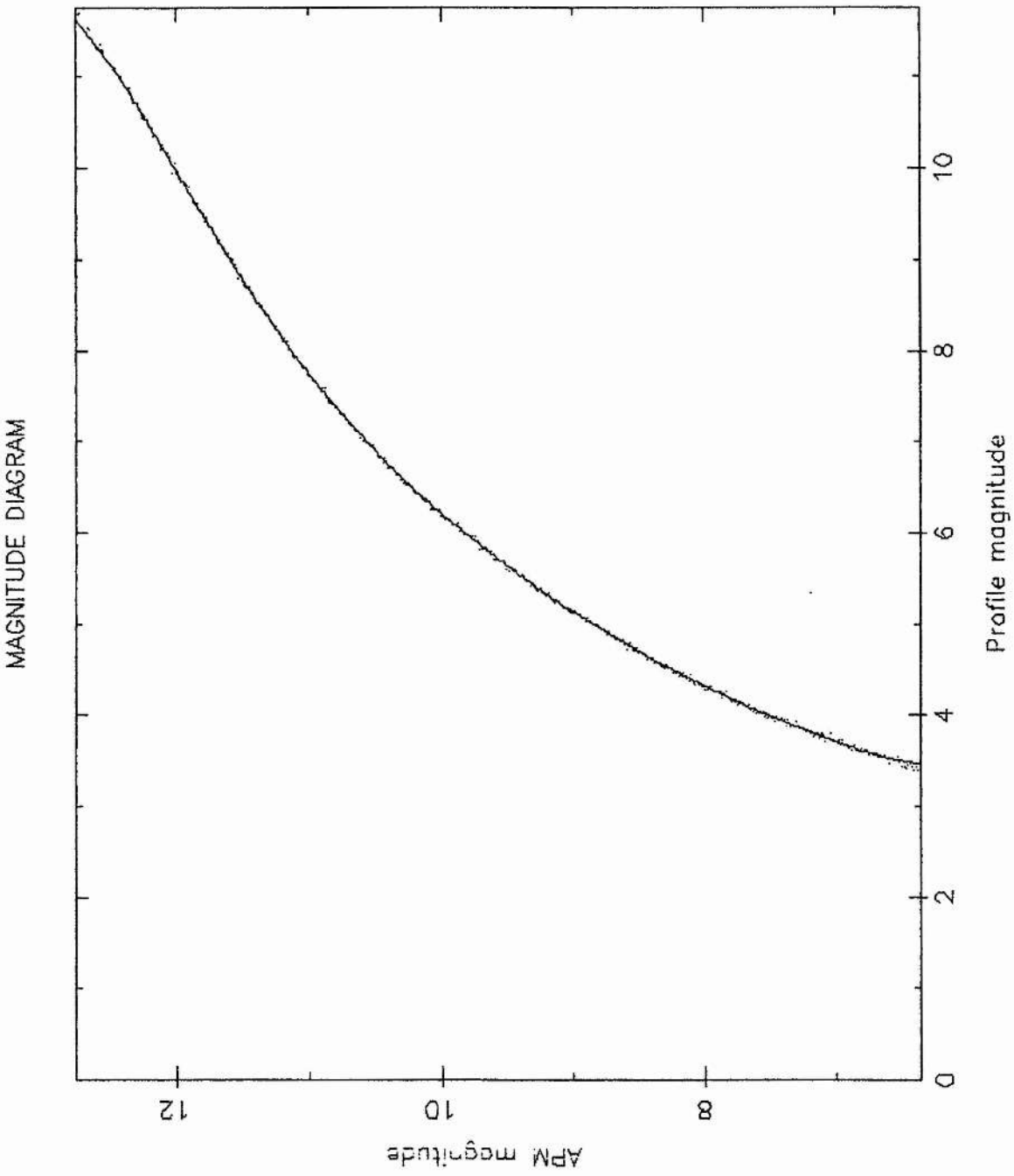

Figure 4.13: The internally generated magnitude for each bin plotted against the corresponding "APM magnitude", which is 2.5 logL. Since L (the integrated intensity) is less noisy than the areal profiles, this curve is actually used to convert the whole data set to internal magnitudes.

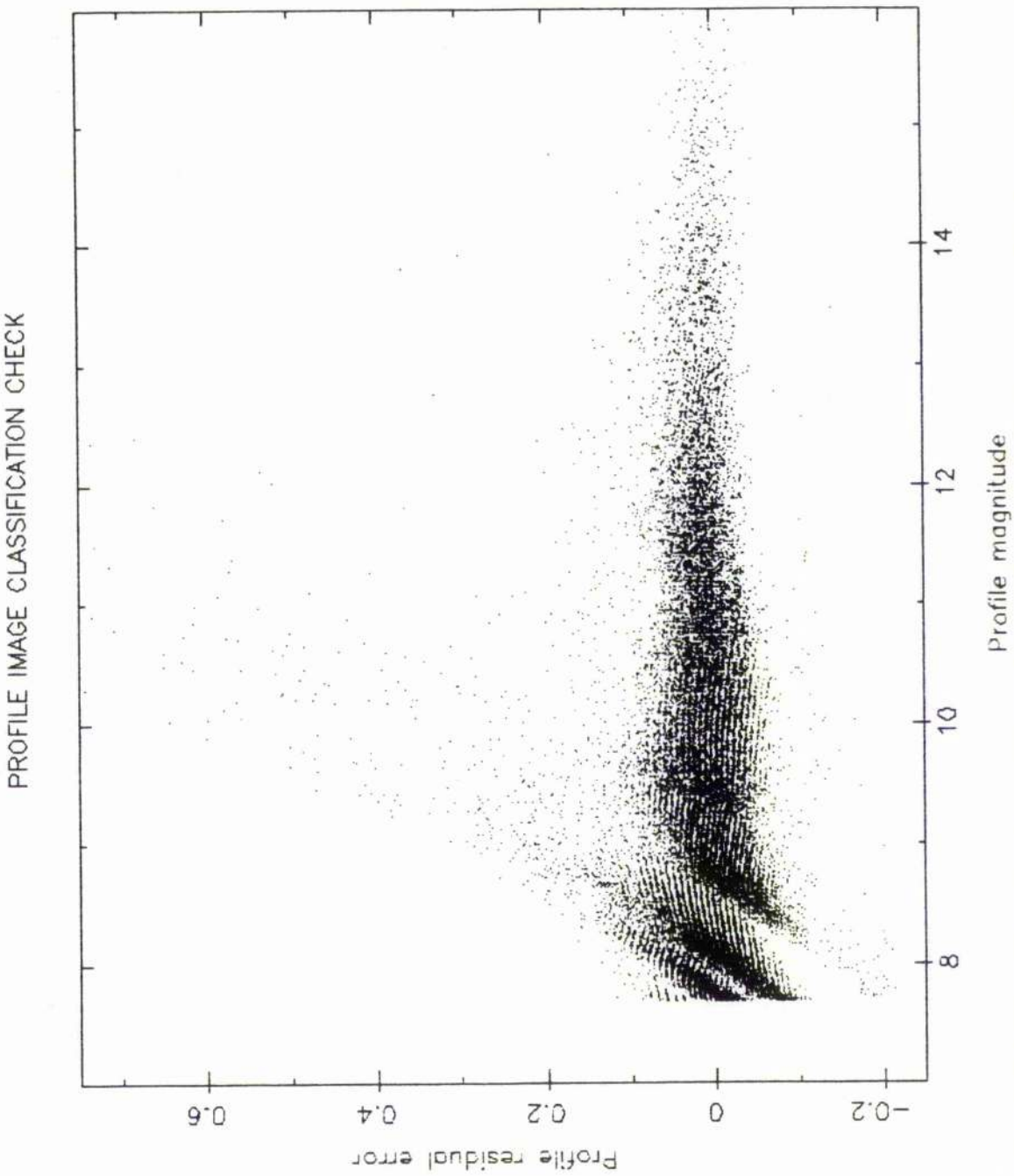

Figure 4.14: Finally the error between an image and the standard profile is an indication of how star-like that image is. There is no advantage over the techniques of STATS (figures 4.4 - 4.7) except at the bright end where saturated stars are better separated from truly extended objects)

values.

External Calibration.

When the internal calibration has been applied independently to each of the U,B,V,R plate data, the COLLATE program is used again, this time to produce a file containing internal magnitudes in each passband for each object. Due to the previous use of COLLATE to reject noise images, all objects in this merged file have V and R values but the faint red objects do not have a match on B and rather less than half of all objects have a U value.

Finally, it remains to calibrate absolutely the internal magnitudes using the photoelectric sequence. The method is essentially the same as for Joyce-Loebl data described in Chapter III, with the important exception that since the whole area is contained in a single homogeneous data set, the whole sequence may be used simultaneously rather than as three sub sequences. Figure 4.15 tabulates photoelectric magnitude and colours, internal magnitudes and colour, and residuals. To summarise, the root mean-square-residual in V is 0.12 magnitudes, in (U-B) is 0.17 magnitudes, in (B-V) is 0.13 magnitudes and in (V-R) is 0.14 magnitudes

A picture of the quality of these reduction procedures can be shown graphically. Figure 4.16 is a map of all the objects detected and matched in both V and R in the 4.6 degree square area scanned. Using stars/galaxy separation, figure 4.17 shows stars only. Note the uniform distribution. Figure 4.18 shows just galaxies. Note the clearly defined clustering all over the field, not just in the three centres of immediate interest to this project.

Further, figure 4.19 shows a colour-magnitude diagram for the stars, and figure 4.20 the two-colour diagram. These pictures are consistent with galactic astronomy, in the sense that this observed distribution is qualitatively what is expected in a direction 56

```
0.9921883    -0.5147181      27.81964

0.9923014     0.1894213       0.43787

0.8416284    -0.2498878E-01   0.63934

0.4572925     0.6137571E-01   1.37344
```

n	V	(U-B)	(B-V)	(V-R)	v	(u-b)	(b-v)	(v-r)	rv	r(u-b)	r(b-v)	r(v-r)
1	9.71	0.01	0.61	0.33	-18.29	3.22	-0.71	0.07	-0.07	0.02	-0.11	-0.03
2	12.12	0.65	0.94	0.53	-15.79	3.27	-0.05	0.17	-0.05	0.03	0.05	-0.01
3	13.25	0.06	0.60	0.34	-14.67	2.77	-0.38	-0.06	0.05	0.28	0.09	0.09
4	13.54	0.77	0.95	0.55	-14.28	3.07	-0.04	-0.05	0.14	0.00	0.01	-0.09
5	13.90	0.45	0.82	0.45	-14.01	2.99	-0.27	0.28	-0.03	0.25	-0.06	0.25
6	13.86	0.80	1.01	0.58	-14.37	3.25	0.18	-0.10	-0.25	0.17	0.14	-0.15
7	15.25	0.75	0.97	0.57	-15.59	2.88	-0.21	0.03	0.06	0.12	-0.19	0.05
8	15.98	1.42	1.52	1.11	-12.07	2.89	0.37	0.13	-0.20	-0.33	-0.27	-0.39
9	12.01	0.71	0.98	0.51	-15.90	3.10	0.01	0.04	0.01	-0.21	0.07	-0.09
10	14.84	-0.01	0.60	0.35	-13.03	2.07	-0.46	-0.08	0.09	-0.05	-0.02	0.17
11	14.89	-0.01	0.56	0.35	-12.93	2.02	-0.40	-0.13	0.17	-0.07	0.07	0.14
12	12.45	0.69	0.92	0.51	-15.37	2.99	-0.06	0.10	0.07	-0.21	0.05	-0.01
13	13.50	0.59	0.88	0.49	-14.20	2.71	-0.33	0.13	0.16	-0.22	-0.16	0.10
14	15.02	0.74	0.95	0.57	-13.03	2.82	-0.05	-0.07	-0.09	-0.04	0.06	-0.04
15	16.06	-0.03	0.52	0.33	-12.09	1.86	-0.21	-0.48	0.01	-0.02	0.24	-0.01
16	16.97	0.02	0.62	0.35	-11.24	1.97	-0.31	-0.46	-0.07	0.18	0.04	0.03
									0.12	0.17	0.13	0.14

Figure 4.15: The calibration of internal magnitudes (lower-case letters) with photoelectric magnitudes (capital letters).

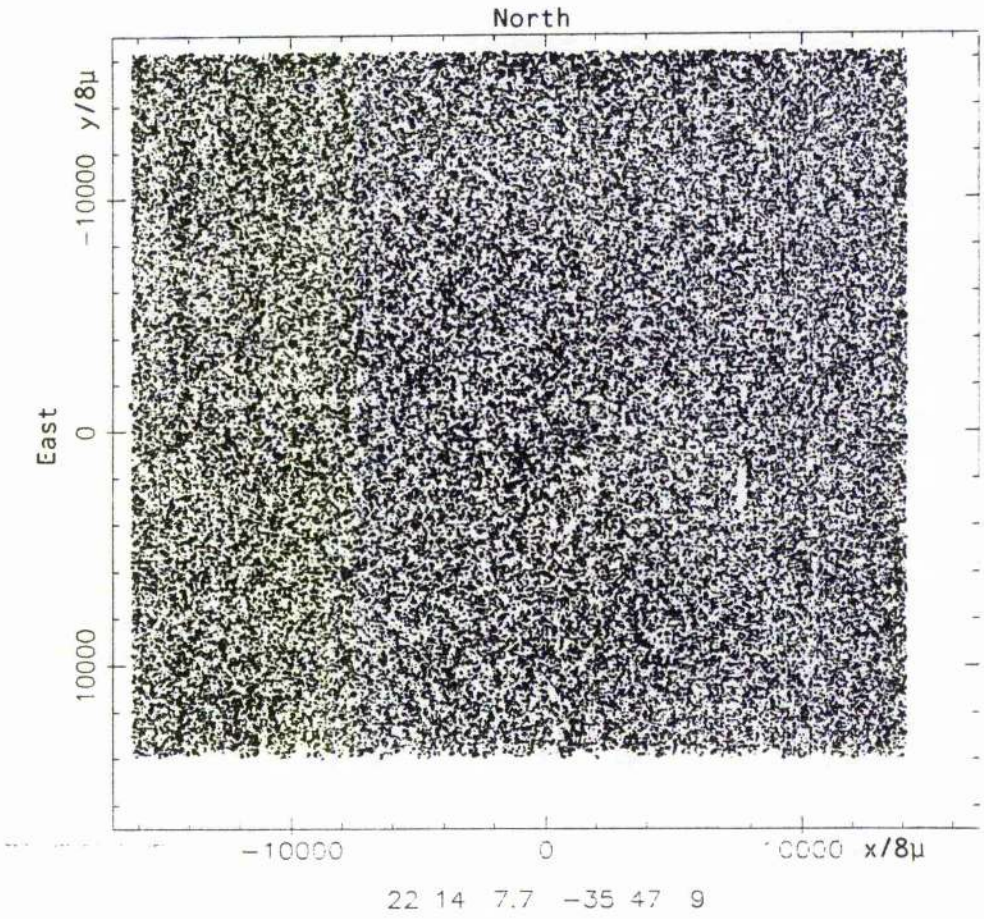

Figure 4.16: Map of all objects down to the limit V = 20 over the 4.6 x 4.6 degree area.

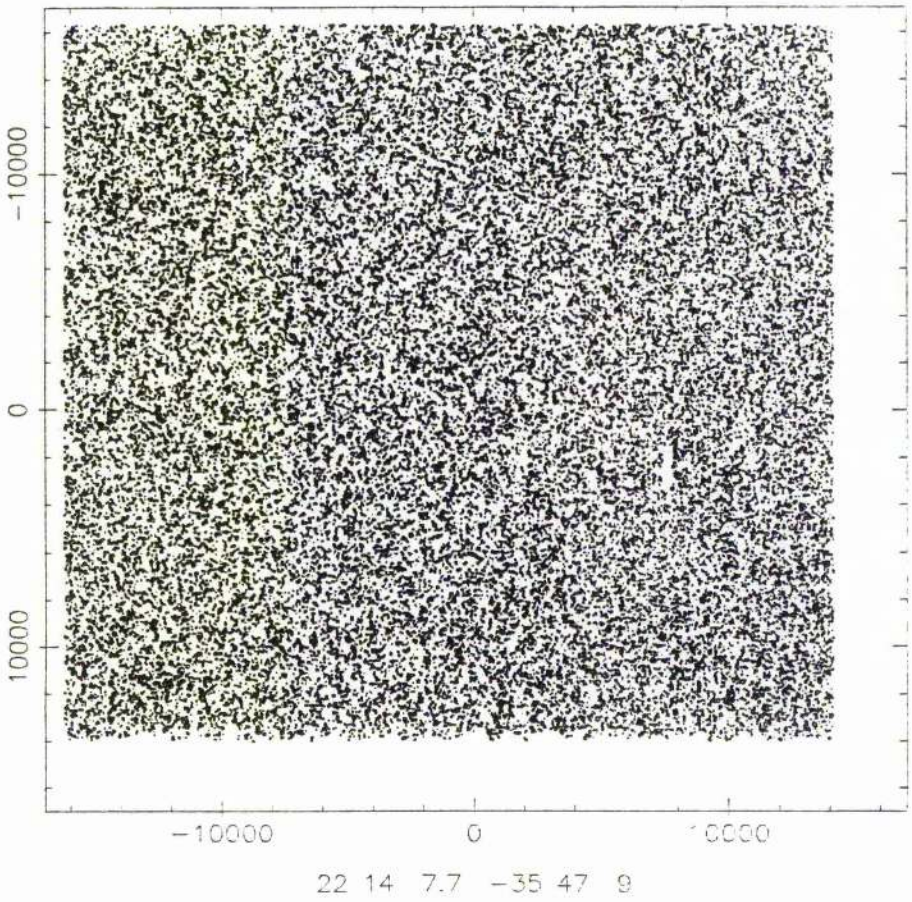

Figure 4.17: Map of stars only.

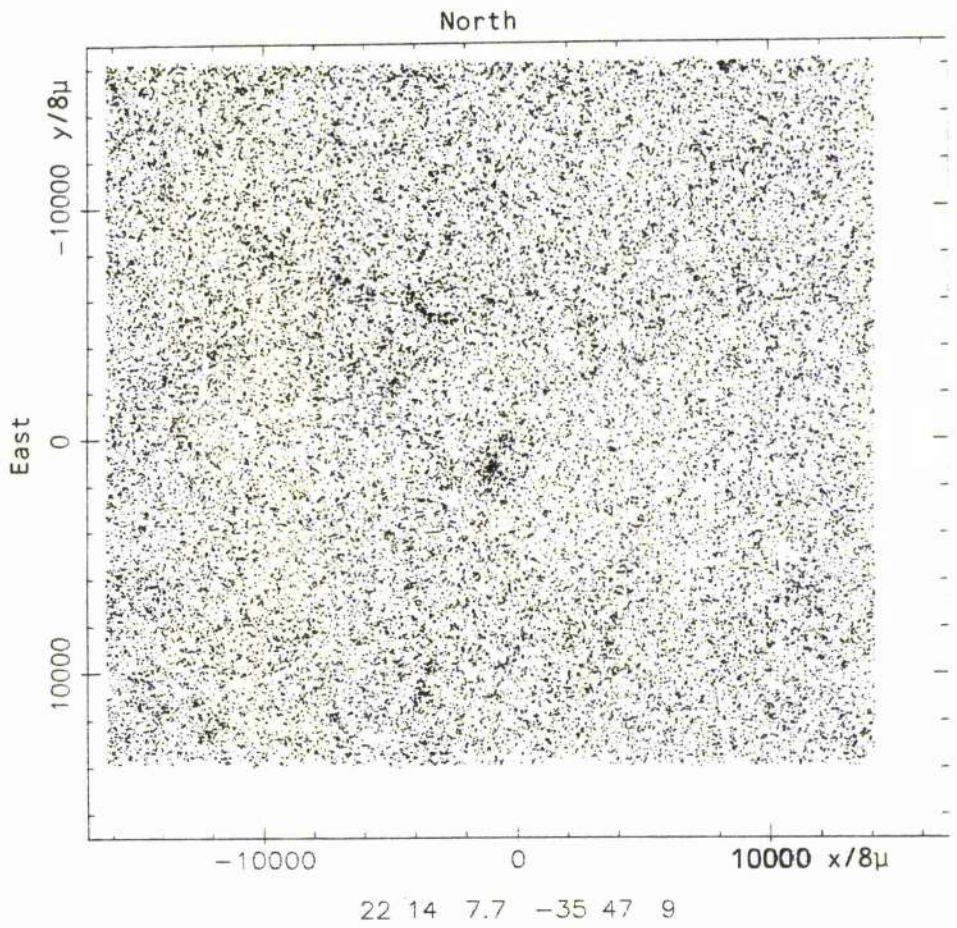

Figure 4.18: Map of galaxies only.

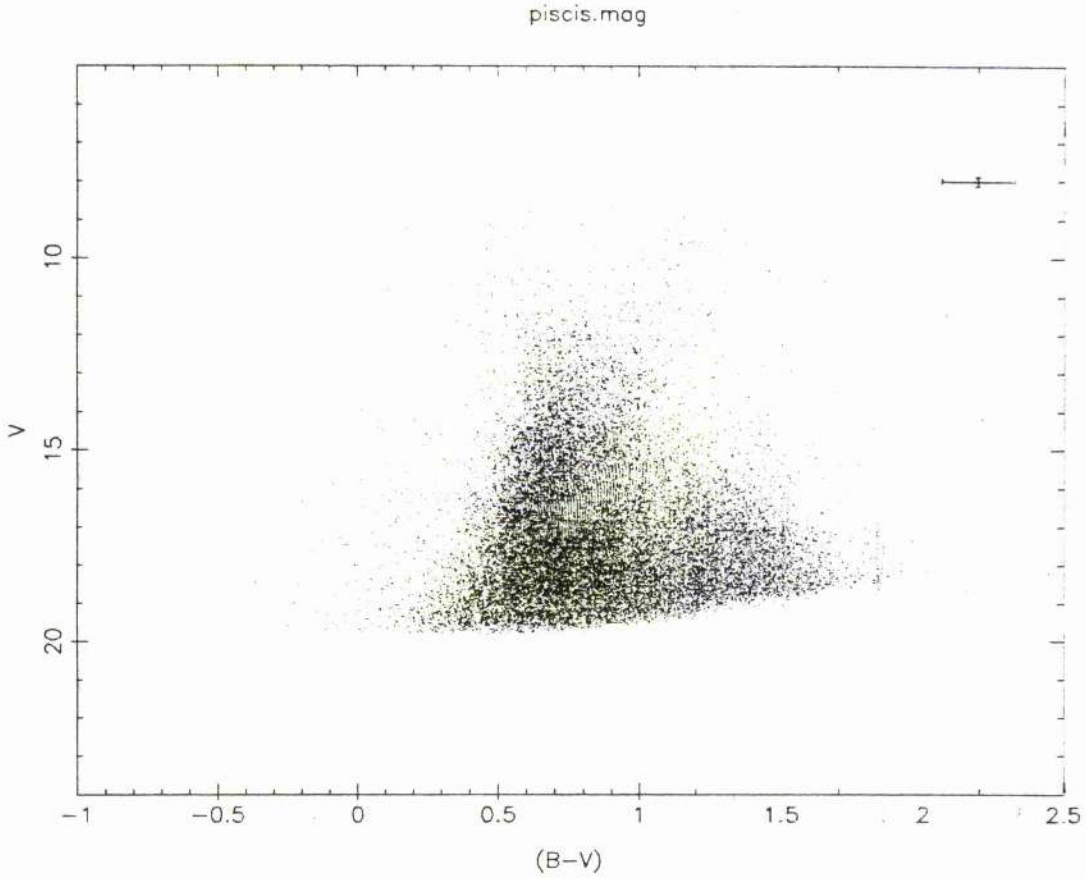

Figure 4.19: Colour-magnitude diagram of field stars.

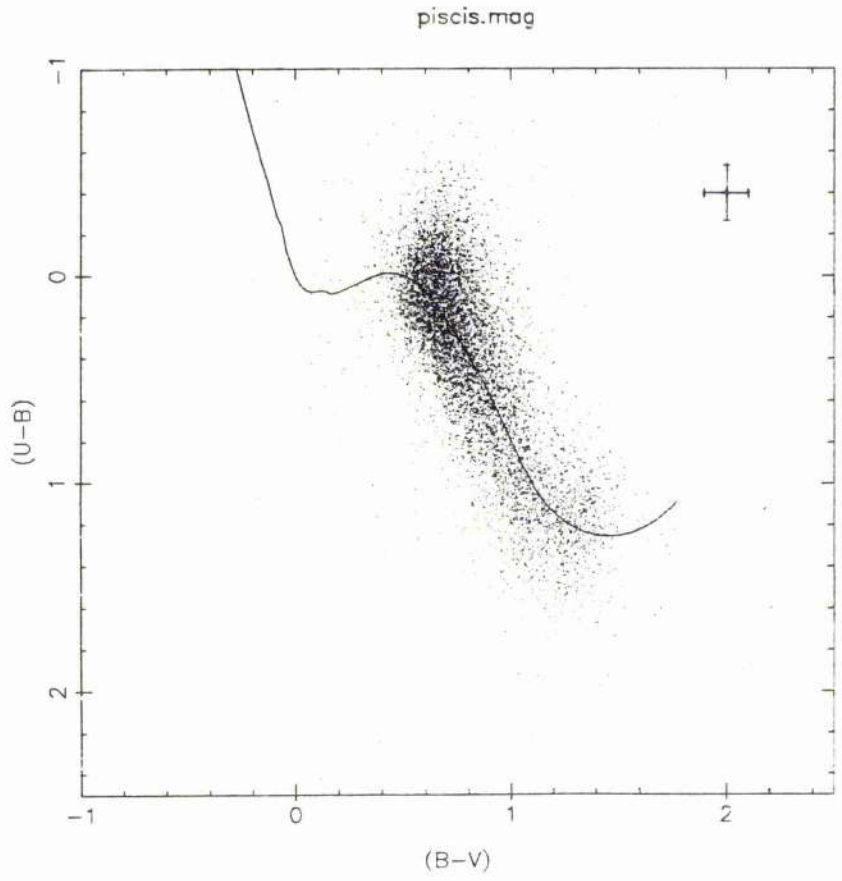

Figure 4.20 The-colour diagram of field stars. The solid line is the main sequence.

degrees from the plane, and could provide interesting results in that field of research which are outside the scope of this thesis.

CHAPTER V

Joyce Loebl compared with APM.

Considering the two machines are both microdensitometers, the Joyce Loebl is very different to APM. Some of the differences have been noted in the preceding chapters, but since it is important to quantify the value of the astronomy produced by these machines, there follows a summary of similarities and differences.

It is stressed that the fundamental difference is in the precision and range of the densitometry. APM uses a flying spot which necessarily has a certain amount of halo causing saturation at around 2.5D above sky, and further, causes problems in regions of differing density gradients. The Joyce Loebl employs projection optics with a mechanical aperture which allows a very sharply defined spot. It can work accurately up to 4D, and is insensitive to density gradients as long as such gradients are small on the scale of the aperture. The density is measured by moving a wedge of continuously varying density in a reference beam until the reference beam balances the measurement beam transmitted by the plate. This system contributes to the extremely slow speed of the machine. The other factor in its slowness is due to the table drive. The table is moved by stepper motors to each sample position, and the position is maintained by 'dead reckoning'. During the course of scanning material for this project, considerable effort was put into modifying the stepper-motor pulse-generation hardware to

prevent electronic noise spikes and pickup causing stray pulses to the motors which corrupt the table position. APM, on the other hand, is built to have high positional accuracy using Moiré fringe encoders with a readout of 0.1 micron. The table is servo driven by powerful motors so it can be moved rapidly over its whole range of travel. This feature coupled with the flying-spot densitometry system enables APM to scan whole Schmidt plates (two giga pixels) in around fifteen hours. The one square centimetre Joyce Loebl scans (262144 pixels) took about seventeen hours. That is to say APM is practically eight thousand times faster than the Joyce Loebl.

The positional accuracy of the Joyce Loebl as determined from collation of the same objects, measured on two (different colour) plates was 1.7 arcsec, or 1.2 arcsec per plate. The corresponding figure for APM, again from two different colours but this time over a 4.5 x 4.5 degree area, was 0.15 arcsec or 0.11 arcsec per plate. Clearly the positional accuracy of the Joyce Loebl is adequate for photometry, since the error is within the seeing disk, but it could not be used for astrometry.

Finally APM has its battery of special purpose processors which produce image parameter data in real time. Joyce Loebl data must be reduced somehow off-line, for example as described in Chapter III. This last difference is actually very important in the context here, i.e. photometry of rich clusters of galaxies. Near the centres of such clusters, most images are partially overlapped. The automatic image-recognition processor of the APM machine treats such joined images as a single large mass, giving spurious results. The interactive technique, although laborious, is the most certain way to treat crowded-field situations. This is a good point to compare the data processing facilities. The Joyce Loebl data was totally reduced on the Nova 820, using software written in FORTH. Although one would now consider this

a slow system, in fact since the reductions were highly interactive, computing speed was not a limiting factor. Interestingly, the other computer accessible at that time, the University of St Andrews Computing Laboratory's IBM 360, could not hold the 512 x 512 raster scans in core, nor was there disk space available for such an amount of data! The situation has now of course changed with the coming of STARLINK and the network of VAX's. The post-scanning reduction of APM data is carried out on these powerful, general-purpose computers.

Photometric comparison.

The Joyce Loebl data, then, is practically free of crowding problems. The photometry of uncrowded images can be compared firstly by looking at the rms residuals in the fit between the photo-electric sequence and the corresponding photographic data:

	V	U-B	B-V	V-R
Joyce Loebl	0.13	0.26	0.02	0.07
APM	0.12	0.17	0.13	0.14

Remembering that the objects involved here are stars, it is not too difficult to understand why the residuals in V are similar. Although APM is not performing such accurate densitometry, the inaccuracy is very systematic in the case of stars as they all have identical profiles, and the calibration procedure described in chapter IV caters for this systematic effect. Note that no slope fitting was necessary to fit the Joyce Loebl data to V magnitudes; this is due to the use of the calibration curve to produce data on a true relative intensity scale.

Similarly, it is not difficult to understand why the U-B fit is worse for the Joyce Loebl data - the reason is the reliance on a

calibration curve derived from about three very faint calibrations steps.

The remaining two colours, B-V and V-R, are apparently much better determined from Joyce Loebl data. The B,V, and R plates had well-defined calibration curves, which explains why these two results are better than in U-B, but not why they are better than V. The explanation may be that the colours were allowed to have an arbitary slope whereas V was solved only for zero point.

Apart from U-B, it is encouraging to obtain as good or better results from the Joyce Loebl data, since this was obtained by directly integrating stellar images, and this is the way of obtaining magnitudes for the galaxies.

It is now instructive to compare reduced photographic data. Figure 5.1 displays comparisons of the four derived quantities, ie. V, (U-B), (B-V) and (V-R).

(i) V magnitudes: Note the complete correspondence down to V = 17, then the APM results are systematically brighter. Remember that the APM calibration used star-profile fitting, whereas the Joyce Loebl reduction procedure integrated intensity down to the V26 isophote. Therefore the APM data overestimates the brightness of galaxies, effectively adding wings and a non-existent brighter core. The Joyce Loebl data, on the other hand, gives meaningful V26 magnitudes to resolved galaxies but underestimates star brightnesses since all the part of the image below V26 is ignored. The effect is more serious the fainter the star, for example the extreme case is a very faint star whose image has a central brightness below V26 and is totally ignored. In fact, it is probable that this underestimation affects faint, partially-resolved or unresolved galaxies, and this might be borne in mind when interpreting the final results.

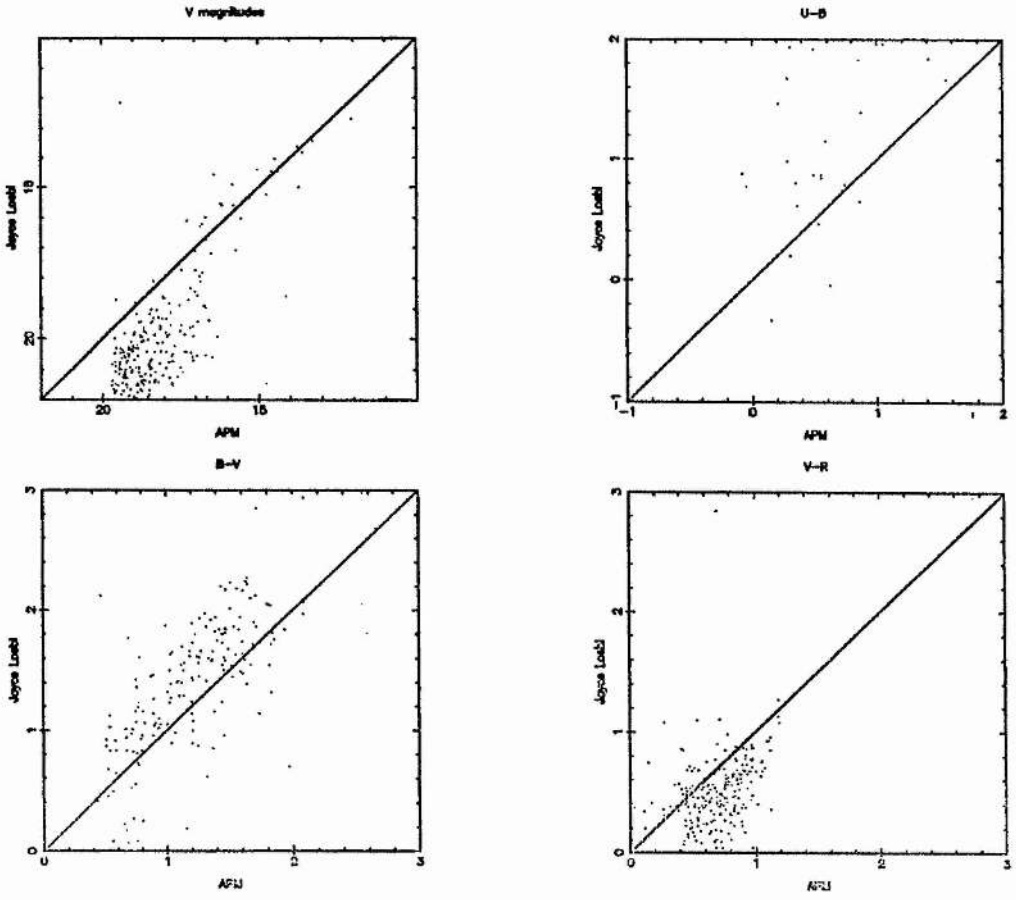

Figure 5.1: Comparison of Joyce Loebl with APM photographic photometry in cluster no. 1 field.

(ii) (U-B) colour: Both machines may have produced poor values for (U-B). The problem with the Joyce Loebl reductions is that the calibrating step wedges are extremely faint; on the other hand although APM does notmake use of the wedges, the U magnitudes of the objects in the cluster field are on the faint limit of detection and are inaccurately determined.

(iii) (B-V): The correspondence here is satisfactory. The difference is again because of the APM data being from star-profile fitting, although this would give correct total colours if the seeing was identical on both the B and V plates. However, the Joyce Loebl reductions employ aperture colours.

(iv) (V-R): The same comments apply as for (B-V).

Image Classification.

A further comparison is in the image classification, including the problem of separating galaxies from foreground galactic stars. Figure 5.2 shows a map of cluster no. 1 from the Joyce Loebl reductions and the same area extracted from the APM data, both star/galaxy separated using the techniques described in chapter III and chapter IV. The first impression is that the APM map is sparser; this is for two reasons. Firstly, because APM automatically detects images, less are picked up then by interactively handling the data with better densitometry provided by the Joyce Loebl. Secondly the centre of the cluster contains closely-packed, overlapping images. Whereas these have been mostly separated during the Joyce Loebl reductions, APM has either merged some into single images or has been unable to handle the situation at all, leaving blank areas which should in fact be densely

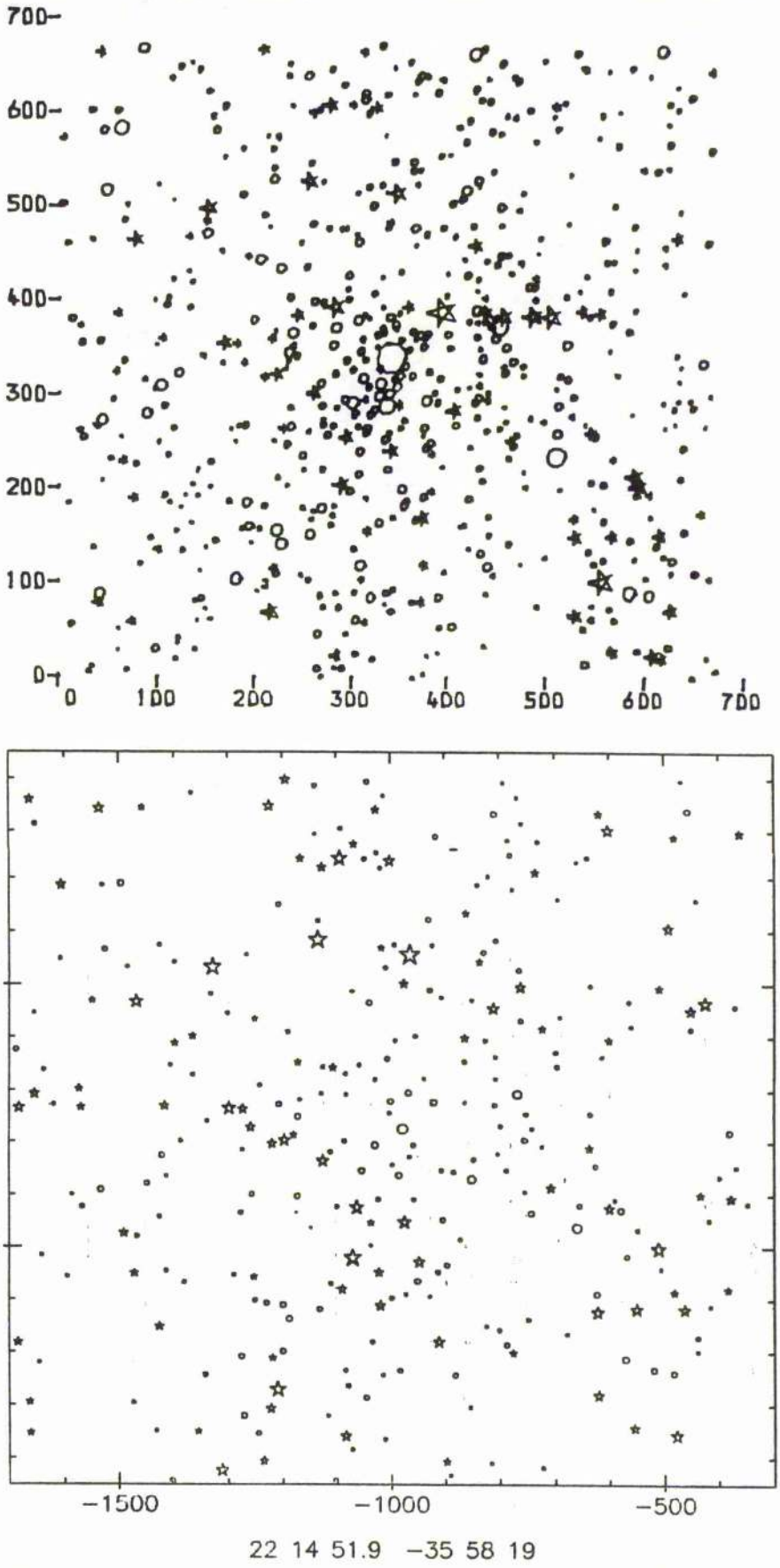

Figure 5.2: Map of cluster no. 1 produced from Joyce Loebl data (top) and APM (below).

populated. The latter effect may arise in two ways:

(i) The edge problem - objects touching the edge of a two millimetre wide scan column are ignored. To overcome this limitation, plates are scanned with a 50% overlap, so that successive columns are started one millimetre apart. Thus objects less than 1mm wide are always measured; objects greater than 2mm are always ignored; and objects between 1mm and 2mm will be measured if they happen to fit between the edges of some column. In the crowded cluster centre, merged conglomerate images may easily be greater then 1mm wide.

(ii) The buffer size problem - at each scan line, slices of any image crossing that line are parameterised. When an image termination is detected, all blocks of slice parameters belonging to the terminated image are passed on for integration. The processor can only buffer 2^{10} (1024) slices, and so for example a vertical scratch 8mm long will fill the buffer and effectively cause that part of data to be lost. In the case of a crowded field, this is less likely than problem (i) (since the conglomerate would have to be 8mm long but less than 2mm wide) but it still may occur.

Completeness.

The APM data, then, suffers from some incompleteness even above the faint magnitude limit. On the whole, the Joyce Loebl data should not suffer any similar problem. However, the Joyce Loebl data does have a different problem at the faint end. Due to the subjective choosing of possible "real" images, then at some faintness level, objects will be wrongly ignored. This problem was tackled by deliberately measuring very faint objects which would probably be noise, then later rejecting objects which did not have corresponding partners on another plate, as described in chapter III.

The APM has a completely objective way of choosing the faintest

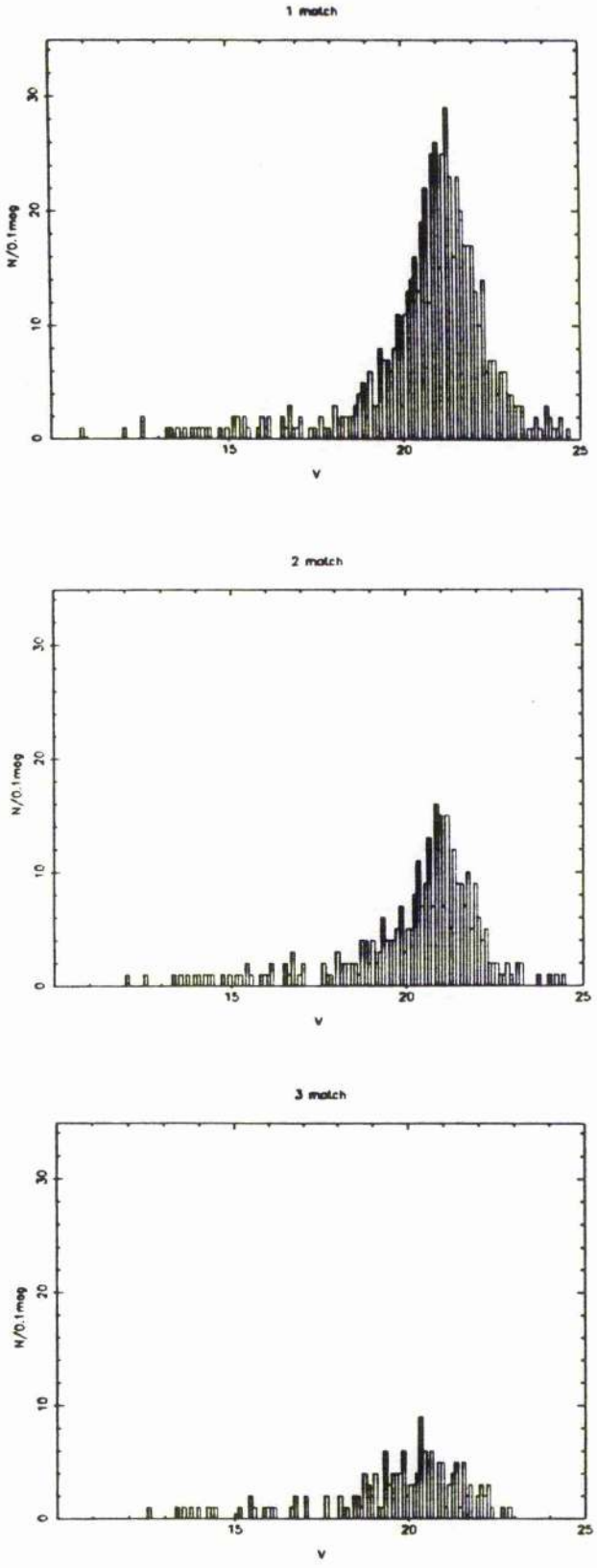

Figure 5.3: Histograms of V_{26} data for all objects in the cluster #1 field obtained from Joyce Loebl data. Top - objects matching with V on at least one of U, B or R; centre - objects with at least two matches; and bottom, objects matching on all three.

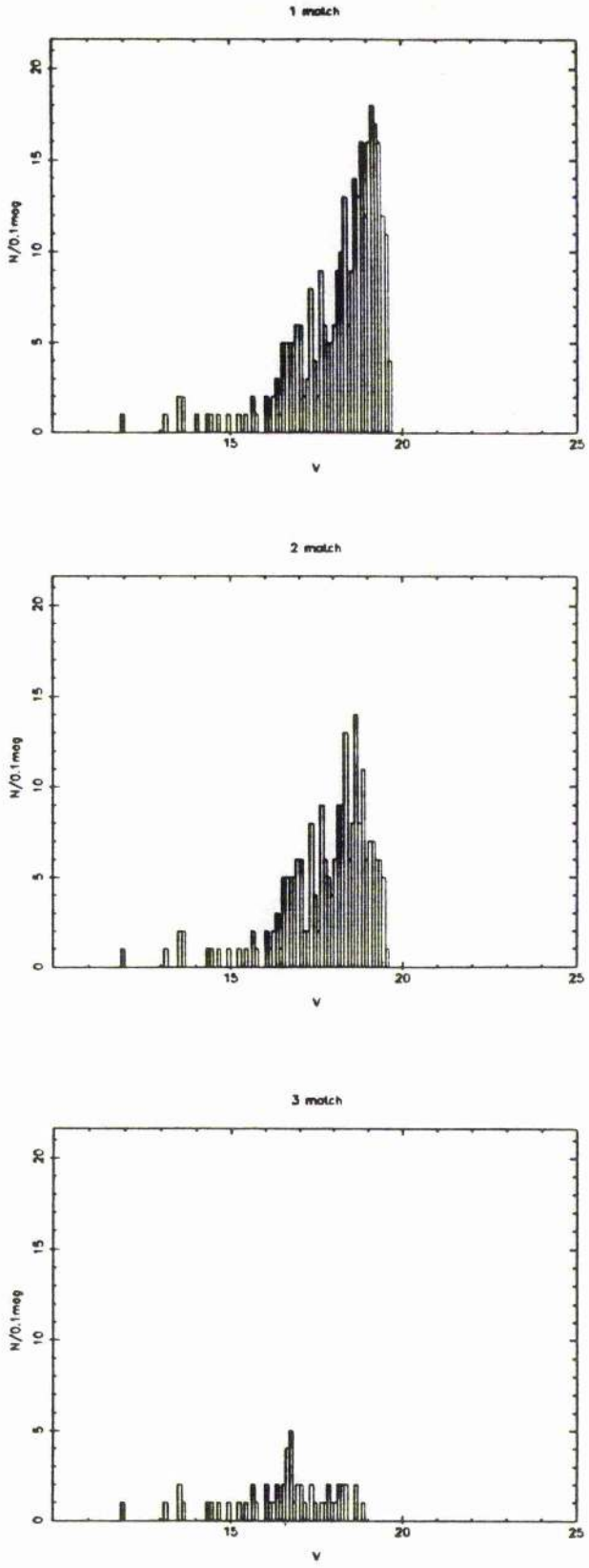

Figure 5.4: Histograms of V_{total} data for all objects in the cluster #1 field obtained from APM data. Top - objects matching with V on one at least one of U, B or R; centre - objects with at least two matches; and bottom, objects matching on all three.

images to be measured, but the APM scans too were made deeper than could really be expected. Spurious images were similarly rejected, using the slightly more stringent condition that an image had to be specifically on both the V and R plates, as described in chapter IV.

Now, figures 5.3 and 5.4 show histograms of the V magnitudes of all objects found in the cluster #1 field. The Joyce Loebl/interactive analysis found 616 objects satisfying the match criterion; APM found 304. Referring to figure 5.1 and comment (i) in the text regarding V magnitudes, it can be seen that APM cuts off (figure 5.4) fairly sharply at a $V_{total} \approx 19.5$, corresponding to a $V_{26} \approx 22.0$ (figure 5.1). Now, the Joyce Loebl data (figure 5.3) peaks at $V_{26} \approx 22.0$ but does not tail off until $V_{26} \approx 24$ ($V_{total} \approx 22$). Of course, without some yet deeper data it is impossible to say what the completeness limit is, but there are substantial numbers of objects pairing up in the Joyce Loebl data some two magnitudes below the APM cutoff, and the total number detected by the Joyce Loebl is double that by APM.

Conclusion.

The APM machine is unsurpassed for scanning whole or large parts of plates. It can generate a huge amount of data which can be calibrated from a single stellar sequence. Positional measurements can be made to high accuracy.

The Joyce Loebl and associated interactive reduction procedures are ideal for dealing with small (eg. 1cm x 1cm) areas. Plates can be seeing compensated to give accurate isophotal magnitudes and aperture colours, to a fainter magnitude limit, and these can be obtained in crowded fields.

CHAPTER VI

Radial Velocities.

Objective Prism Spectra.

The source for measurement of redshifts for this project is a UKST low-dispersion objective-prism plate. In order to plan the approach to extracting a spectrum from an objective-prism plate and subsequently producing some physical measurement of that spectrum, it is necessary to discuss the generation of the spectrum image on the plate.

Basically, all the broadening processes applying to direct images as discussed in chapter III are combined with the dispersive effect of the objective prism. Images are broadened by atmospheric seeing and then dispersed by the prism. The dispersed light is imaged by the normal telescope optics, introducing more broadening due to residual optical observations, and the focussed spectrum suffers scattering in the emulsion. The intensity distribution of the spectral image is added to "white" sky illuminations, and finally the photographic emulsion records the light.

Three factors complicate the recovery of incident intensity from a measurement of resultant density. Firstly, the dispersion of a prism is not linear. It is well described by the Hartmann formula (Hartmann 1898):

$$\lambda = \lambda_o + \frac{C_o}{(x - x_o)}$$

where λ_o and C_o are constant for a particular telescope/prism combination, and xo depends on the origin chosen to make linear measurements of a particular spectrum. The effect of the variable dispersion is to "squeeze" the light at long wavelengths, by an amount proportional to the gradient of the dispersion.

$$\frac{d\lambda}{dx} = \frac{-C_o}{(x - x_o)^2}$$

Secondly the atmosphere and telescope have a finite transmission window, and thirdly the emulsion also has a finite window inside of which the sensitivity is non-uniform, so the calibration curve is effectively a function of wavelength.

To summarise, the recorded spectrum is the true spectrum distorted by the non-linear dispersion, convolved with the profile of the source object blurred by seeing, added to sky light, and registered irregularly by the emulsion.

The dispersion curve may be derived from a suitable stellar spectrum. Figure 6.1 shows the spectrum of an A-type star scanned on the Joyce Loebl. The intensity has been obtained from the calibration curve (without regard to wavelength) with sky subtracted. The abscissa is in sample steps of 20 micron using a scanning aperture of 15 x 45 micron. The continuum is produced by selecting points on a graphics terminal and interpolating between them with a cubic spline function. The useful part of the data normalised to the continuum is shown in figure 6.2, where the position of the absorption lines can be more

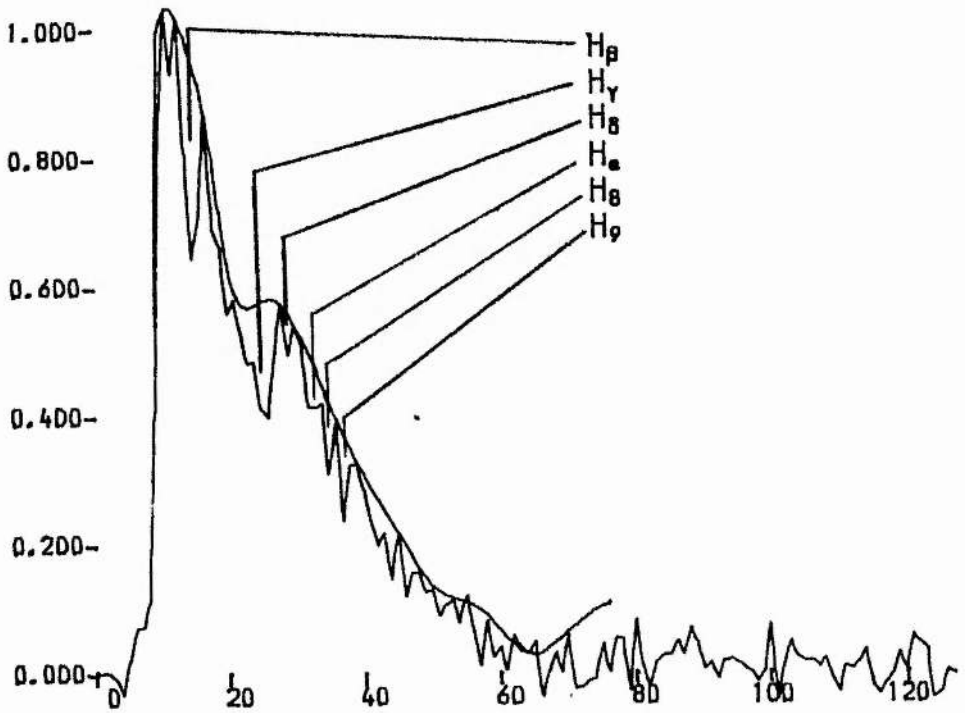

Figure 6.1: Scan of an A-type star, with relative intensity plotted against sample stars (20 micron).

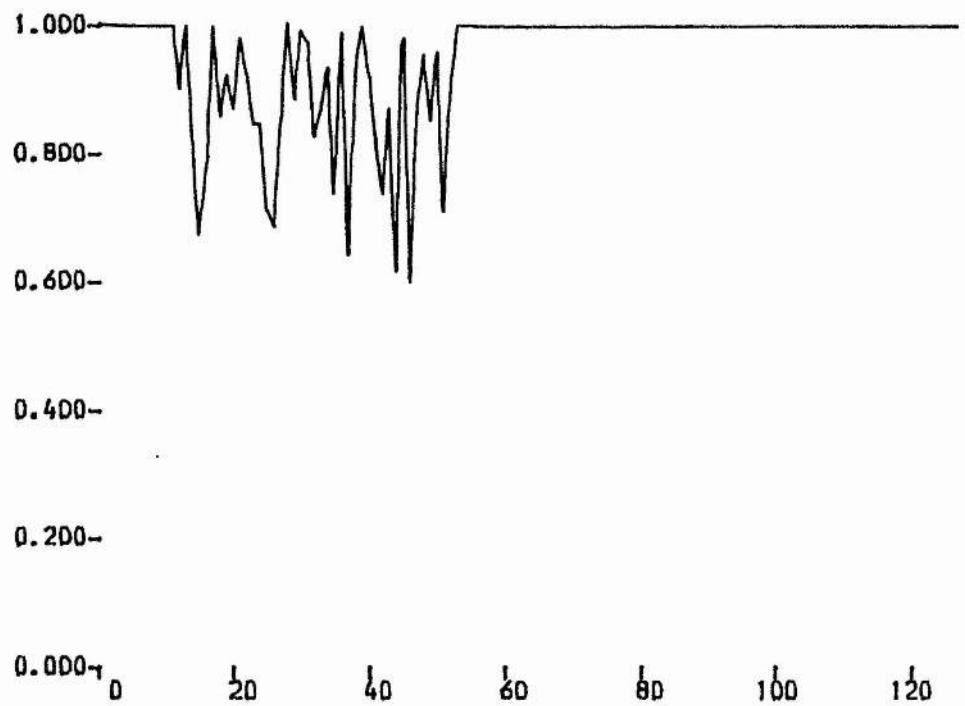

Figure 6.2: Rectified version of figure 6.1.

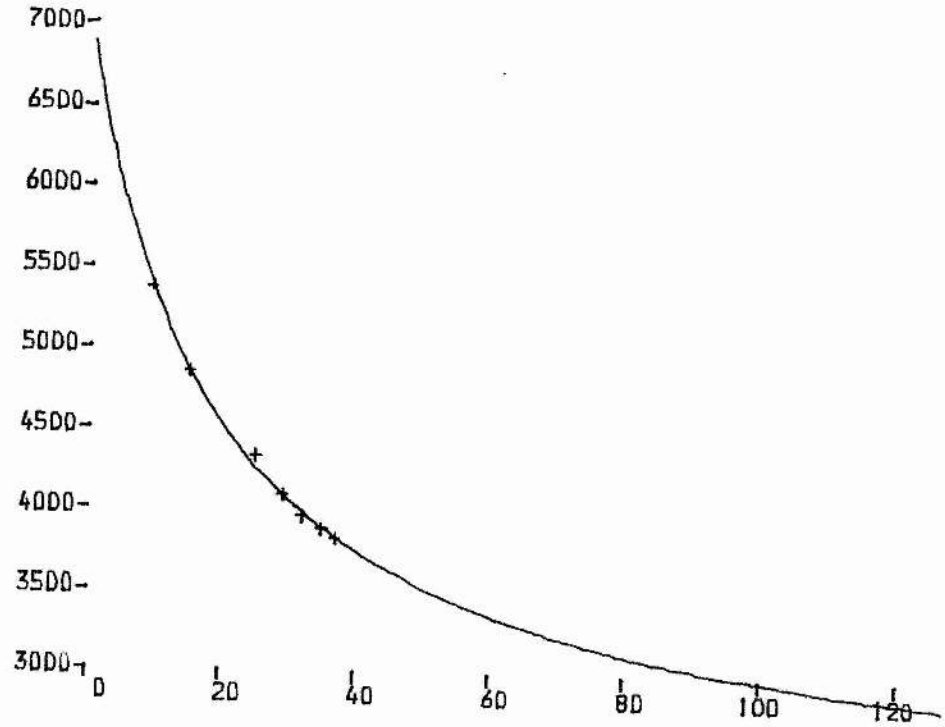

Figure 6.3: Dispersion curve derived from six hydrogen lines and green cutoff.

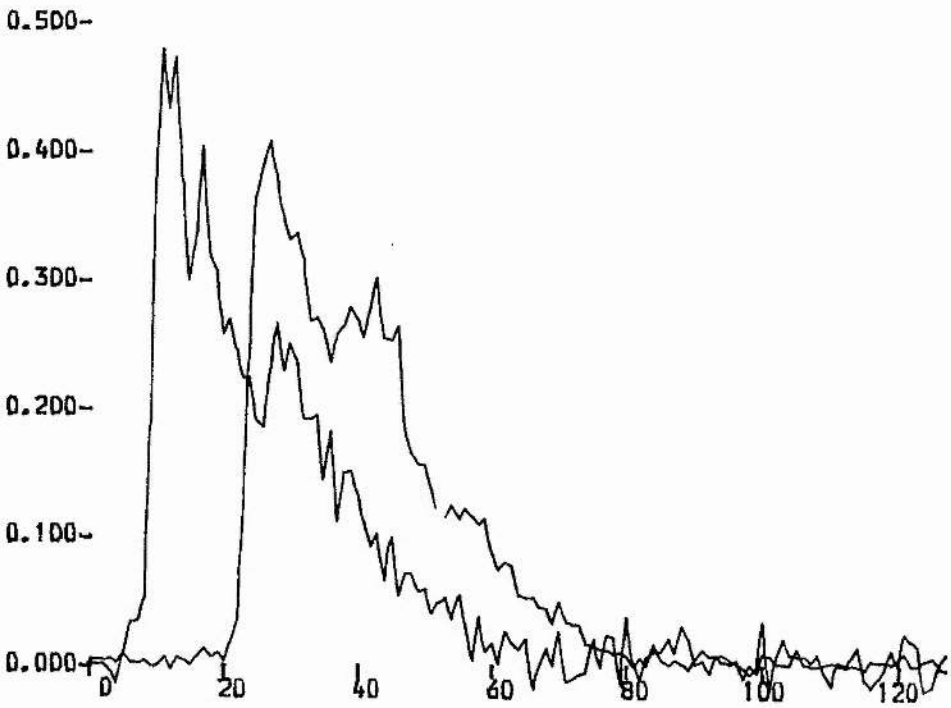

Figure 6.4: As figure 6.1 with galaxy spectrum superimposed.

accurately measured - note for example H_ε. Six hydrogen lines from H_β to H9 can be identified, and the green cut-off, as defined by Nandy et al (1977) is also used to plot the dispersion curve shown in figure 6.3. This Hartmann curve differs from the true dispersion by less than the errors in the measurements.

Da Costa et al (1977) have demonstrated the use of cross-correlation techniques to determine very accurate radial velocities. It is this technique which is used here not only to determine actual redshifts, but also to establish the zero point of the spectrum image.

Figure 6.4 shows the spectrum in figure 6.1 superimposed on that of a member of cluster no. 1. The overall profile of an image as an objective-prism plate is dominated by the plate response, particularly at the green cutoff. The relative shift between the two images may be obtained accurately using the cross-correlation of the two profiles.

The Fourier transform version of the cross correlation is used as it is convenient and computationally efficient:

$$C(\Delta) = \text{const} \times \Sigma_k \tilde{S}_1(k)\tilde{S}_o(-k) \exp(i2\pi k\Delta/n)$$

where $\tilde{S}$ denotes transforms. Because low frequency filtering is unnecessary, since the images fall to zero at each end and the high frequencies are retained (the green cutoff is a high-frequency feature), no filtering is used. The resulting cross-correlation function from this example is shown in figure 6.5. The actual maximum found by interpolating the differential with respect to Δ around the peak to the point where it passes through zero (figure 6.6) which, in

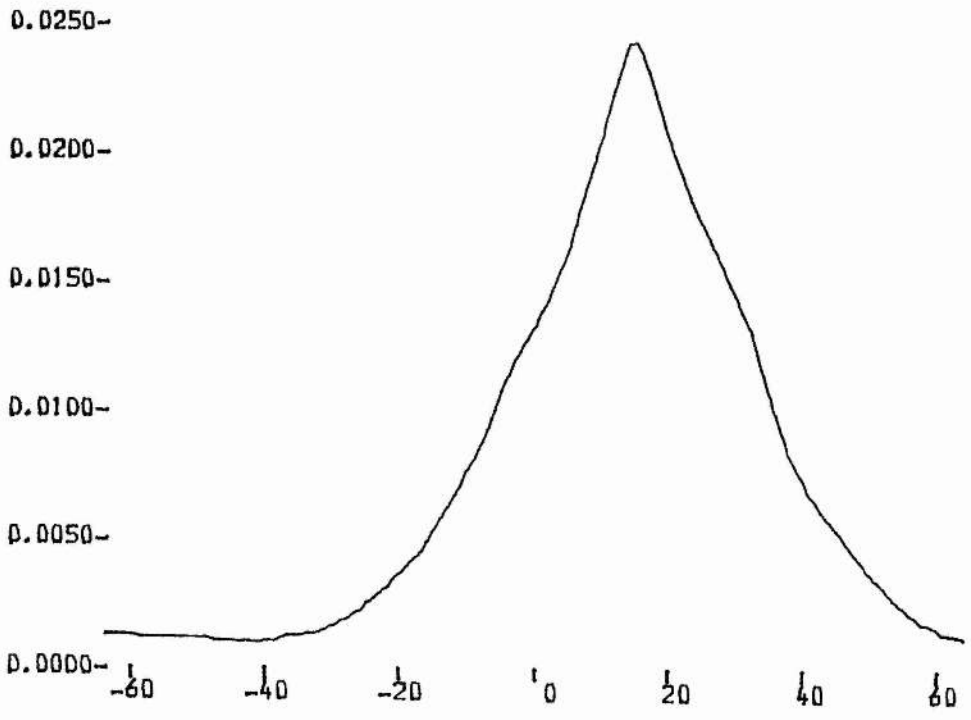

Figure 6.5: Cross Correlation of the images in figure 6.4

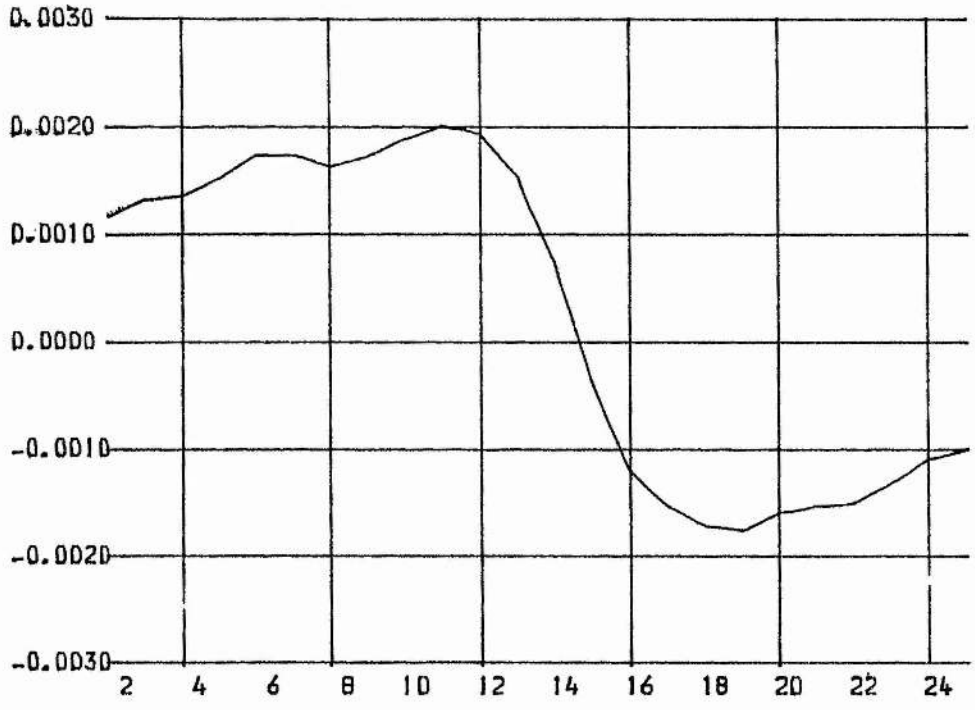

Figure 6.6: Differential of the peak of figure 6.4.

this case, gives a Δ of 14.7 sample steps. Figure 6.7 shows the superposition of the two spectra using this shift.

To measure the radial velocity, the galaxy spectrum is transformed into logarithmic coordinates, so that the whole spectrum is shifted by a constant log (1+z). The image of the galaxy shown in figure 6.8 has been processed as follows:

(a) it has been normalised to the continuum, with all non-significant signal replaced by horizontal continuum,

(b) the value of 1.0 has been subtracted to produce a zero-level continuum, with all the resulting information solely in the form of absorption features, and

(c) the data has been transformed to the log (λ) domain by converting a point on the logarithmic scale to wavelength and determining the corresponding x-position; the intensity at that point is derived from linear interpolation between the two adjacent data points. The logarithmic interval is chosen to match the resolution of the original scan.

The zero-velocity comparison data is derived from Pence (1976) and his mean E-S0 energy curve is similarly transformed. The cross-correlation function is computed (figure 6.9) using only the wavelength ranges common to both data sets and its peak, determined as before, leads to a value of Z = 0.159.

The power of this technique is that it maximizes the amount of

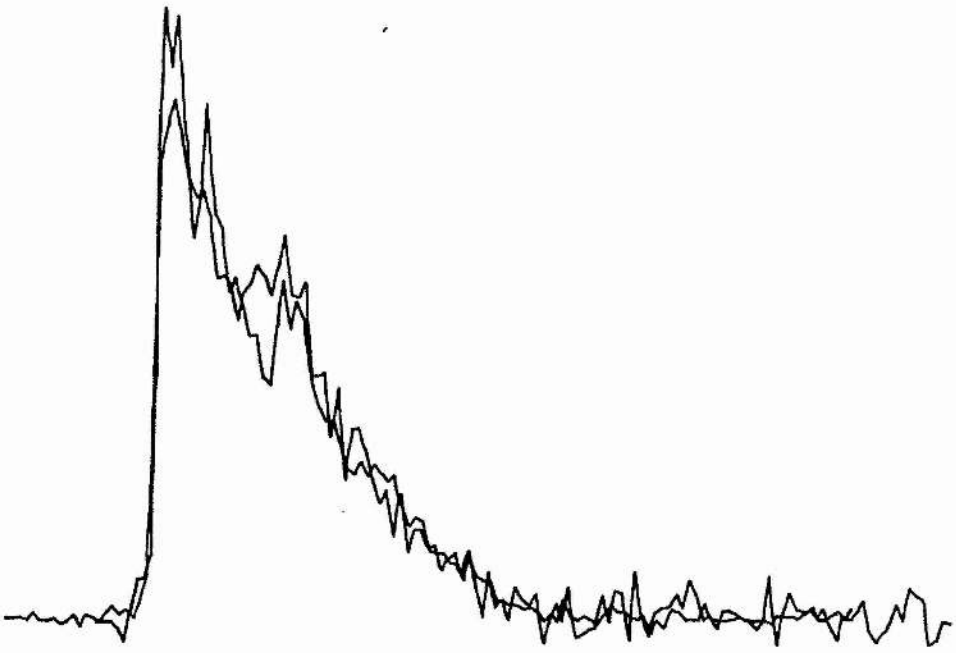

Figure 6.7: Images of figure 6.4 shifted by the value Δ found from the correlation function.

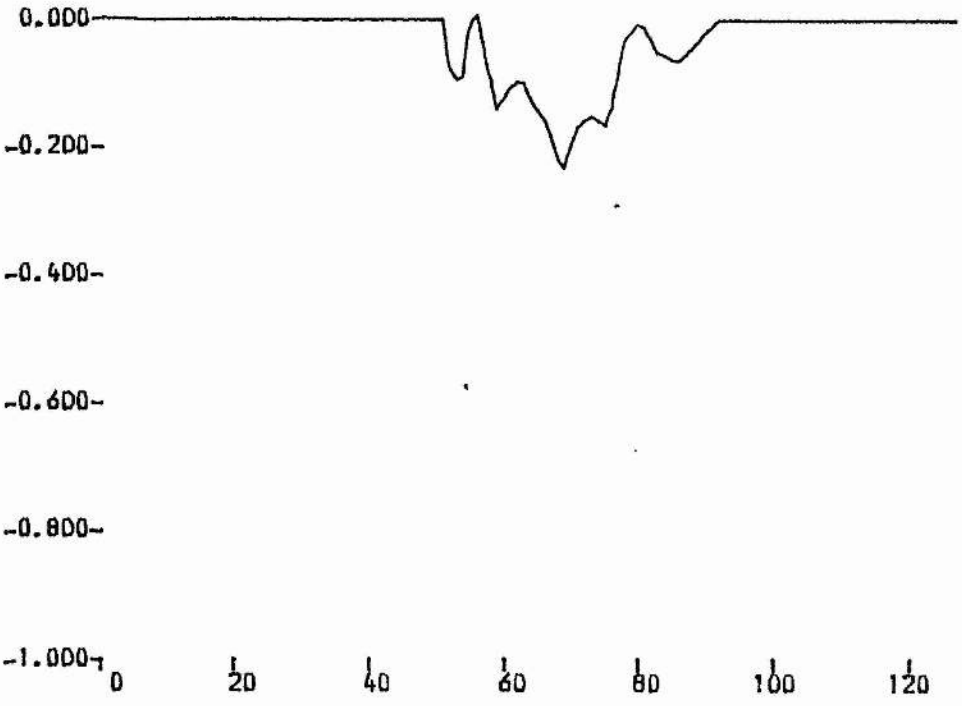

Figure 6.8: Processed image of the galaxy shown in figure 6.4.

data used in the radial-velocity determination. The main weakness in this argument lies in the dispersion curve. However, a periodic variation in the curve would normally average out, but a shift would give a systematic error. A pessimistic value for the error would be the equivalent of half a sample step, 23 Å at H_γ or z = 0.005. The precision may be greatly improved if the cross-correlation technique is applied to two similar spectra of similar radial velocity. A systematic shift in the disperison curve would then cancel out, and the errors would depend mainly upon the errors in the two cross-correlations involved. Typical errors in the relative redshift would then be equivalent to about 0.1 sample steps, or 300 km/sec. This accuracy is sufficient to investigate the internal velocity dispersions in clusters.

Consider a particular spectral feature whose rest wavelength is λ_o which appears in two redshifted spectra at observed wavelengths of λ_1 and λ_2:

$$z_1 = \frac{\lambda_1 - \lambda_o}{\lambda_o} = \frac{\lambda_1}{\lambda_o} - 1$$

$$z_2 = \frac{\lambda_2 - \lambda_o}{\lambda_o} = \frac{\lambda_2}{\lambda_o} - 1$$

hence $$\log\lambda_1 = \log\lambda_o + \log(1+z_1)$$

$$\log\lambda_2 = \log\lambda_o + \log(1+z_2)$$

so $$\log\lambda_2 - \log\lambda_1 = \Delta = \log(1+z_2) - \log(1+z_1)$$

giving $$10^{\Delta} = \frac{1+z_2}{1+z_1}$$

so that $$z_2 - z_1 = (1+z_1)(10^{\Delta}-1)$$

The quantity $z_2 - z_1$ is not seriously affected by an error in the absolute value taken for z_1; in the case here, where z_1 will be approximately 0.15, a 100% error in z_1 contributes only an 8% error to $(z_2 - z_1)$.

Figure 6.10 shows the cross-correlation function for the galaxy already displayed with another from the same cluster, producing a value of $z_2 - z_1$ of 0.0107, or 3200 km s^{-1}.

As acknowledged by Cooke (Cooke 1981) in his paper on redshifts from objective prism data, he made use of the St Andrews Joyce Loebl to scan a few galaxies in A2670 which already have accurately determined redshifts by Oemler. This author took the opportunity to use some of the data to check the techniques just described. The results are as follows:

Oemler km s^{-1}	Measured km s^{-1}	test-Oemler
23200	23640	440
23670	28580	4910
22700	22330	-370
23460	23540	80
23400	11565	-11835
22350	23100	-750
21430	39850	18420

The results are either as good as claimed or spectacularly wrong. The non-Gaussion error distribution results from the case where two different features 'lock on' in the cross-correlation procedure. This

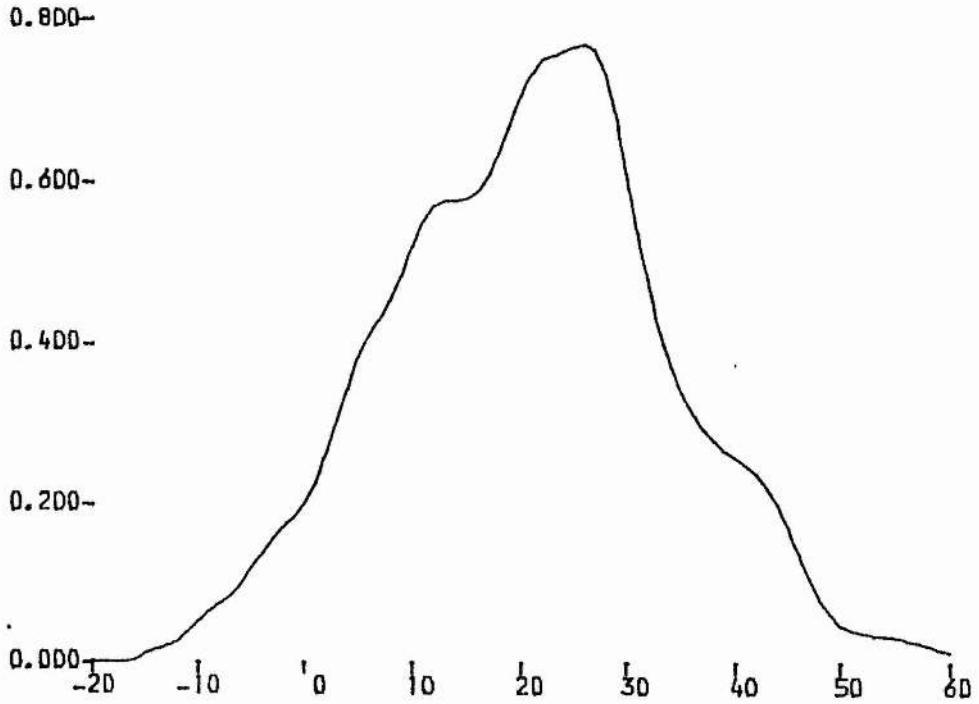

Figure 6.9: Cross correlation function of figure 6.8 with a similarly processed version of the mean E-SO energy distribution.

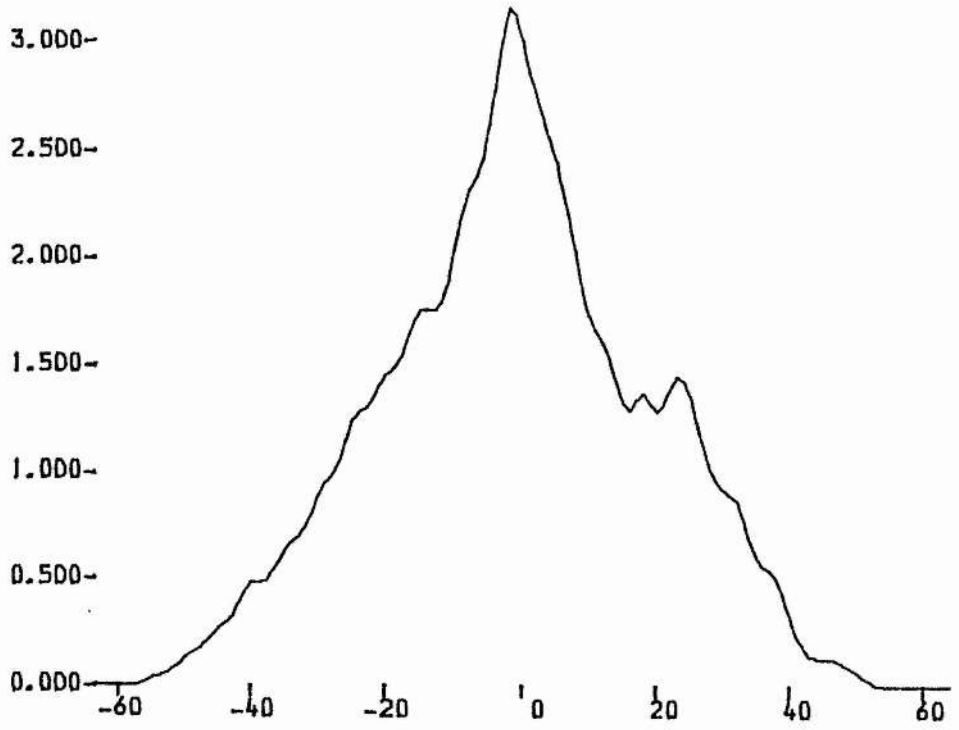

Figure 6.10: Cross correlation of two galaxies in the same cluster.

kind of error is unavoidable and means that the whole technique of using low-dispersion objective prism plates to measure redshifts cannot give reliable results for particular objects; however, it is most useful in determining statistical properties of clusters of galaxies. The rms of the four low-error results above is 470 km s^{-1}, whereas the rms of all seven errors is 8500 km s^{-1}.

APM Method.

The semi-interactive techniques just described and developed using Joyce Loebl data and reduced in the Nova 820 have been automated on the VAX to allow reduction of large numbers of spectra obtained from APM spectra-scanning mode. The APM method of scanning objective-prism spectra is described in Hewett, Irwin, Bunclark, Bridgeland & Kibblewhite (1985). Briefly, a co-ordinate list of all objects in a field is generated from a scan of a direct plate. The machine can accurately zero-point each spectrum from this data. A two-dimensional image of a spectrum is scanned, and the image data summed along the direction of the spectrum to obtain its mean cross-sectional profile. This profile is fitted by least squares at each point along the spectrum, a system which maximizes the signal-to-noise ratio. Conversly, attempting to reduce noise by using a slit across the spectrum gives too much weight to the wings, where transmission is highest.

For this project the brightest 30000 images in this 4.4 degree (giving a faint cutoff of V = 18.0) were scanned. The raw spectra are on an arbitrary scale, so were calibrated by matching B-magnitude for

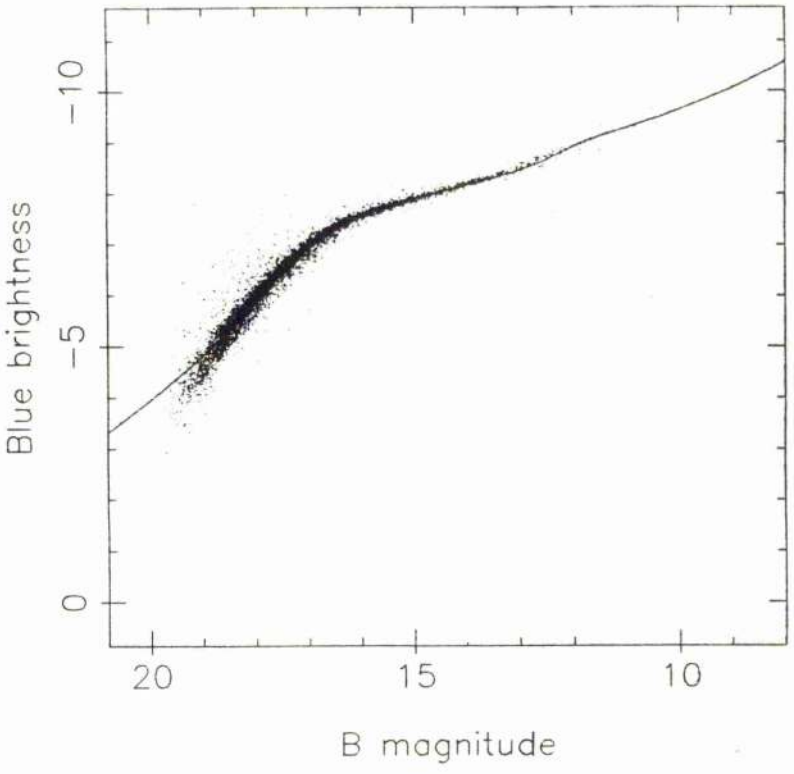

Figure 6.11: Intensity calibration of spectra data.

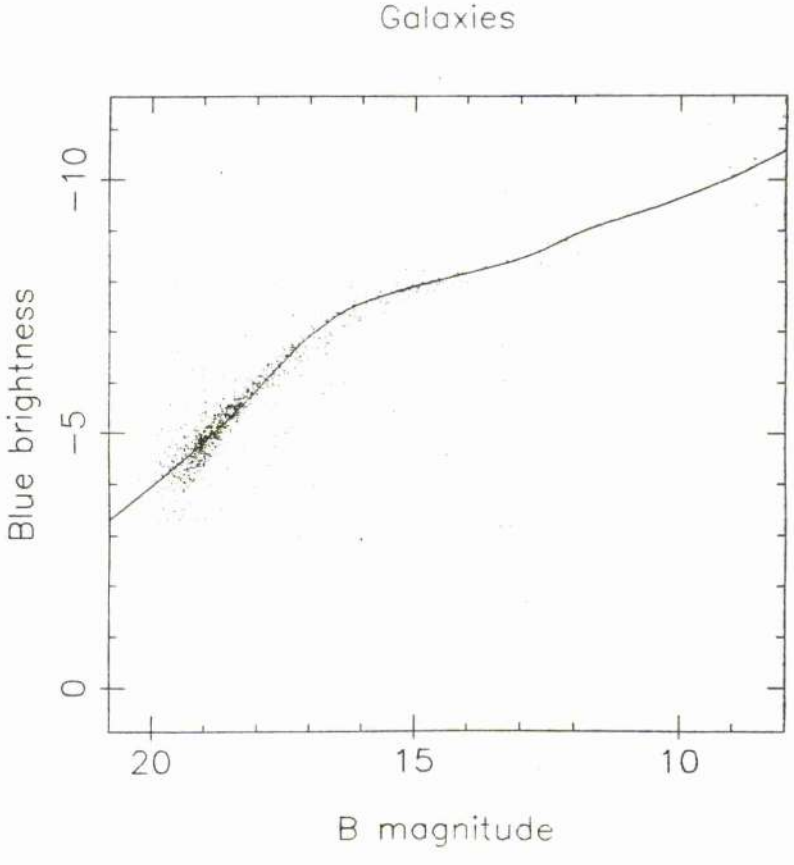

Figure 6.12: Calibration curve plotted on galaxy data.

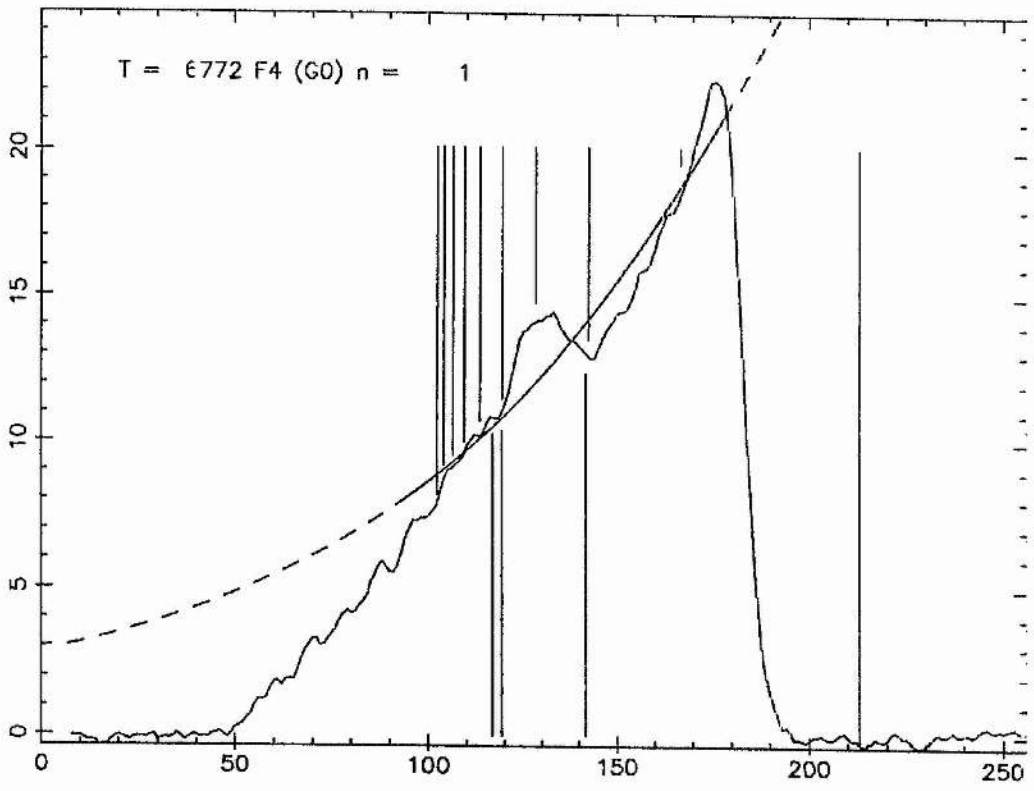

Figure 6.13: Mean G0 spectrum photometrically classified. Spectral type corresponding to effective temperature is F4

each object to the sum of the data in the corresponding region of each spectrum. Actually, the data for the stars (figure 6.11) was used to obtain a mean calibration curve, and figure 6.12 shows that curve superimposed on the galaxies. This calibration phase is required to ensure that objects of a similar nature but of different apparent magnitude are not mutually distorted. The majority of the spectra obtained were classified as stars in the ratio 23700:6300. As a test of the calibration, and of the emulsion response with wavelength, a black-body curve was fitted over that part of the Paschen continuum before the green cutoff, to a number of spectra pre-classified from (B-V) and averaged (figure 6.13). The near-correspondence shows the IIIaJ emulsion response is fairly flat at least over the range 3700 Angstroms to 5100 Angstroms.

The redshift determinations follow those already described with the exception that continua are computed by fitting the black-body curve (whose temperature is not meaningful but which fits the spectra rather well). On the first iteration, a cluster galaxy is chosen as the "master", and a number of galaxy spectra shifted to a common z are averaged to produce a template for the second iteration.

Test of APM Method.

A general test of the method was performed by using a UKST prism plate of the South Galactic Pole, and comparing the redshift determinations from that with those taken from the Durham Redshift Survey (Bean et al 1983) in the same field.

The test is severe since the comparison is carried out over the whole range $0.0 < z < 0.11$, and on spectra scattered over a large area

of plate, as opposed to the ideal cluster situation where the spectra are both physically near and are at very similar redshift. Furthermore, the spectra are now being measured with the APM flying-spot system rather than the Joyce Loebl projected aperture. The APM spot will tend to render the green (ie long-wavelength) cutoff less sharp than it actually is, and as measured by the Joyce-Loebl. A further effect might be a drop in constrast of features, due to an additive contribution from the spot halo. However, the profile-fitting technique should result in the best signal-to-noise ratio under the circumstances.

The results of the test are summarised graphically in figures 6.14, 6.15 and 6.16. Figure 6.14 merely serves as an identification check. The objects were found from the spectrum data by their celestial co-ordinates; the figure shows the instrumental J magnitude derived by integrating over the appropriate part of the matched spectrum, plotted against the J magnitude of Bean et al. Plus symbols are objects whose nearest match was greater than 5 arcsec from the published position, and the star symbols those with errors greater than 10 arcsec. Since the distance errors correlate with the photometric errors, objects are rejected from the test if their distance errors are greater than 5 arcsec.

Figure 6.15 shows the comparison of measured z and the values of Bean et al, and figure 6.16 is a histogram of the differences. The value for the standard deviation of the gaussian core, ie 0.015, corresponds to 4500 km s^{-1}. This is much poorer than was obtained with the Oemler/A2670 test, but as noted the conditions are far more general, and in fact this error is similar to that found by Cooke et al

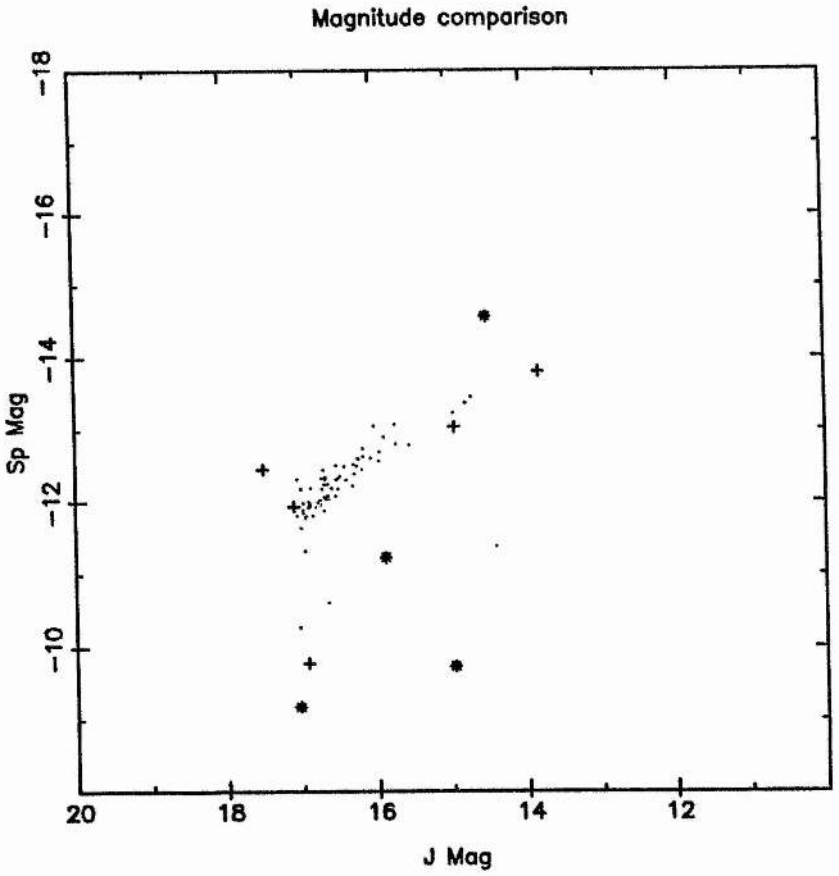

Figure 6.14: Identification check for galaxies in the Durham Redshift survey. Abscissa is published J magnitude, ordinate is instrumental magnitude from the spectrum in each case with the nearest co-ordinate match.

'+' symbols represent objects with co-ordinate errors > 5", and '*' symbols those with errors > 10".

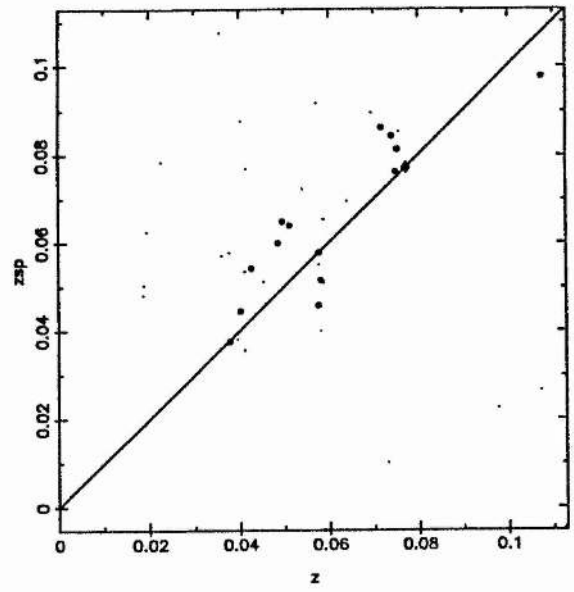

Figure 6.15: Measured redshift (zsp) vs values from the Durham Redshift Survey (z) in the South Galactic Polar region. The solid line is the 1:1 relationship. ♦ represents ellipticals, • represents S0 galaxies.

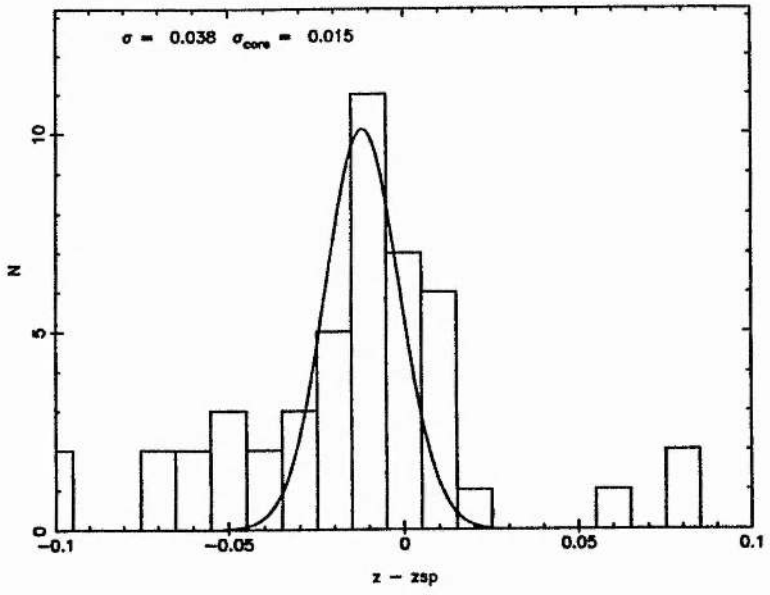

Figure 6.16: Histogram of $z_{Durham} - z_{measured}$. The fitted gaussian has a standard deviation of 0.015.

n	z	zsp	names	Jmag	class	dist/"							
1	0.0187	0.1662	GSA002	13.82	SC	5.4							
2	0.1075	0.0977	GSA004	14.41	S0	1.9							
3	0.0187	0.0684	GSA001	14.51	SBC	13.0							
4	0.0404	0.0878	GSA003	14.72	SBC	0.9							
5	0.0187	0.0481	GSA005	14.80	SB	0.8							
6	0.0190	0.1632	GSA007	14.95	SBC	5.1							
7	0.0179	0.0770	GSA006	14.96	CO+	3.3							
8	0.0690	0.1920	GSAN01	14.97	SB	10.5							
9	0.0584	0.2213	GSA008	15.55	S0	2.5							
10	0.0589	0.0510	GSA009	15.73	SPE	3.9							
11	0.0324	0.1674	GSAN02	15.74	SBC	402.2							
12	0.0341	0.0125	GSAN04	15.88	SAB	191.8							
13	0.0195	0.0625	GSA012	15.89	SB+	0.7							
14	0.0360	0.0571	GSA015	15.95	SB	1.8							
15	0.0578	0.0578	GSA010	15.96	S0	2.9							
16	0.0402	0.1123	GSA016	16.02	SBP	1.1							
17	0.0756	0.0854	GSA011	16.07	SAB	0.8							
18	0.0577	0.0458	GSA014	16.17	S0	1.8							
19	0.0357	0.1076	GSA017	16.17	SB	1.0							
20	0.0378	0.0375	GSA013	16.19	S0	2.1							
21	0.0412	0.0535	GSA020	16.23	SPE	0.7							
22	0.0588	0.0654	GSA021	16.24	SA	0.5	60	0.0759	0.2556	GSA062	16.90	SA	2.3
23	0.0573	0.0918	GSA019	16.26	SBC	2.5	61	0.0996	−0.0100	GSA058	16.92	S0	5.2
24	0.0521	0.0660	GSA023	16.29	PE+	4.1	62	0.0764	0.1718	GSA069	16.93	SBC	1.3
25	0.0648	0.1857	GSAN05	16.30	SB	1.7	63	0.0582	0.0515	GSA050	16.94	S0	3.6
26	0.0581	0.0400	GSA024	16.31	SA	2.5	64	0.0188	0.0503	GSA079	16.95	SC	1.7
27	0.0185	0.1356	GSA022	16.40	S0	2.0	65	0.0646	0.1182	GSA060	16.97	S0	2.3
28	0.0749	0.0763	GSA025	16.42	S0	1.8	66	0.0542	0.0723	GSA061	16.97	SA	2.8
29	0.0395	0.0382	GSA032	16.48	SPE	1.0	67	0.0729	0.0101	GSA070	16.97	SB	3.9
30	0.0497	0.0649	GSA027	16.51	S0	1.6	68	0.0377	0.0578	GSA074	17.00	SA	1.2
31	0.0753	0.0814	GSA018	16.51	S0	1.4	69	0.0585	0.1844	GSA078	17.00	SC	3.1
32	0.0576	0.2039	GSA033	16.53	SAB	2.4	70	0.0204	0.0319	GSA090	17.03	PEC	1.8
33	0.0402	0.1693	GSA035	16.53	SA	1.3	71	0.0533	0.0225	GSA087	17.04	SBC	217.6
34	0.0481	0.1506	GSA026	16.54	SA	3.4	72	0.0228	0.0785	GSA084	17.05	SPE	2.3
35	0.0578	0.0551	GSA039	16.59	SB	0.8	73	0.0404	0.2128	GSA071	17.05	S0	0.4
36	0.0064	0.1667	GSA046	16.62	SDM	2.2	74	0.0678	0.1968	GSA091	17.09	S2+	5.2
37	0.0773	0.0772	GSA034	16.64	E1	1.1	75	0.0380	0.0155	GSA001	17.50	S0	7.5
38	0.0402	0.0445	GSA031	16.64	S0	1.3							
39	0.0427	0.0542	GSA023	16.65	S0+	1.3							
40	0.0580	0.1719	GSA028	16.65	SA	3.1							
41	0.0577	0.0517	GSA037	16.66	SA	1.8							
42	0.0513	0.0640	GSA038	16.68	S0	1.0							
43	0.0487	0.0600	GSA034	16.68	S0	2.2							
44	0.0699	0.0215	GSA043	16.69	PEC	2.0							
45	0.1072	0.0265	GSA036	16.69	SPE	1.6							
46	0.0416	0.0770	GSA131	16.69	SB	0.8							
47	0.0579	0.1648	GSA030	16.70	E0+	4.0							
48	0.0574	0.1730	GSA047	16.72	SC	4.7							
49	0.0694	0.0896	GSA052	16.73	SC	3.9							
50	0.0341	0.1958	GSA041	16.73	SB	1.9							
51	0.1128	−0.0053	GSA048	16.74	ECD	3.9							
52	0.0412	0.0356	GSA053	16.77	S	1.4							
53	0.0717	0.0863	GSA040	16.80	S0	1.2							
54	0.1074	0.1553	GSA056	16.84	SB	1.7							
55	0.0454	0.0512	GSA067	16.87	SC	3.9							
56	0.0640	0.0695	GSA049	16.87	SB	3.0							
57	0.0977	0.0225	GSA051	16.88	SB	3.4							
58	0.1003	0.1554	GSA064	16.89	SC	1.5							
59	0.0740	0.0844	GSA045	16.89	S0	0.8							

Table 6.1: Results of the test with the Durham Redshift Survey.

(1984). Finally, table 6.1 lists the Durham, and measured, z values for the objects used in the comparison.

Comparison with other Piscis Austrinus data.

West and Frandsen (1981) present a list of thirty-two redshifts. Their values for the two objects they measure in the cluster #1 field (2215-359) disagree with the estimate of the mean cluster value obtained using the method described (0.121 and 0.147 respectively). Velocities for the actual objects measured by West and Frandsen cannot be obtained from the objective-prism plate due to excessive crowding in the cluster centre. Following is a criticism of their techniques and results.

(i) Check with other work.

There is no external evidence to validate the data; W&F say "We are confident that the quoted redshifts are correct within the quoted errors, even though none of these galaxies have been observed elsewhere." Thus there is no casting vote, but it may be said that W&F could easily have observed a few objects with published redshifts to check their reduction procedures - preferably over a good range of z.

(ii) Identification of Features.

W&F claim to have 10 Primary Features, ie strong features. In their figure 2, they plot three spectra with the primary features indicated. It can be seen that while they often happen to fall in local minima, the indicated features can hardly be said to be the

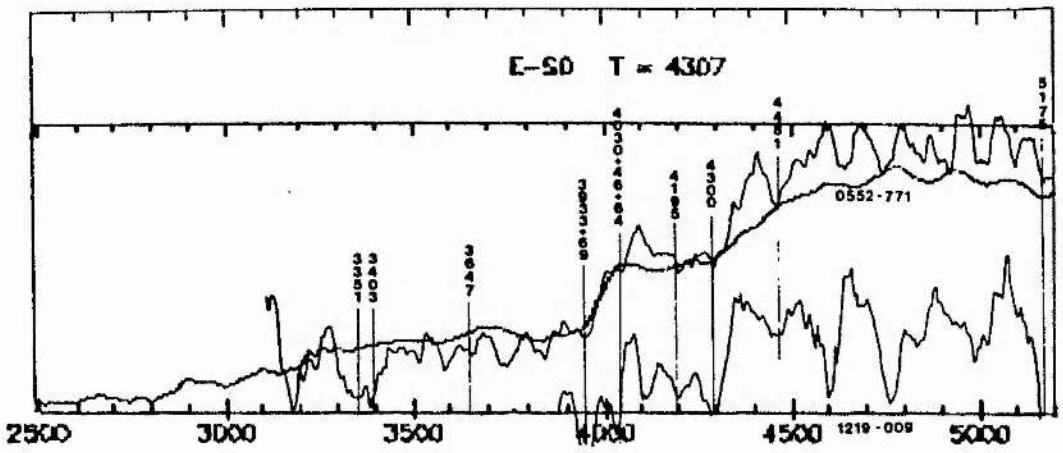

Figure 6.17: Pence E-SO superimposed on 0552-771.

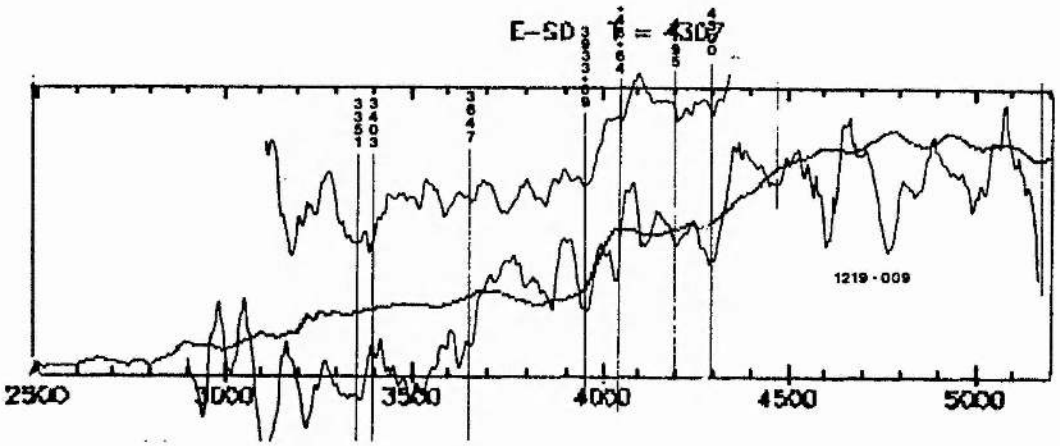

Figure 6.18: Pence directly superimposed on 1219-009.

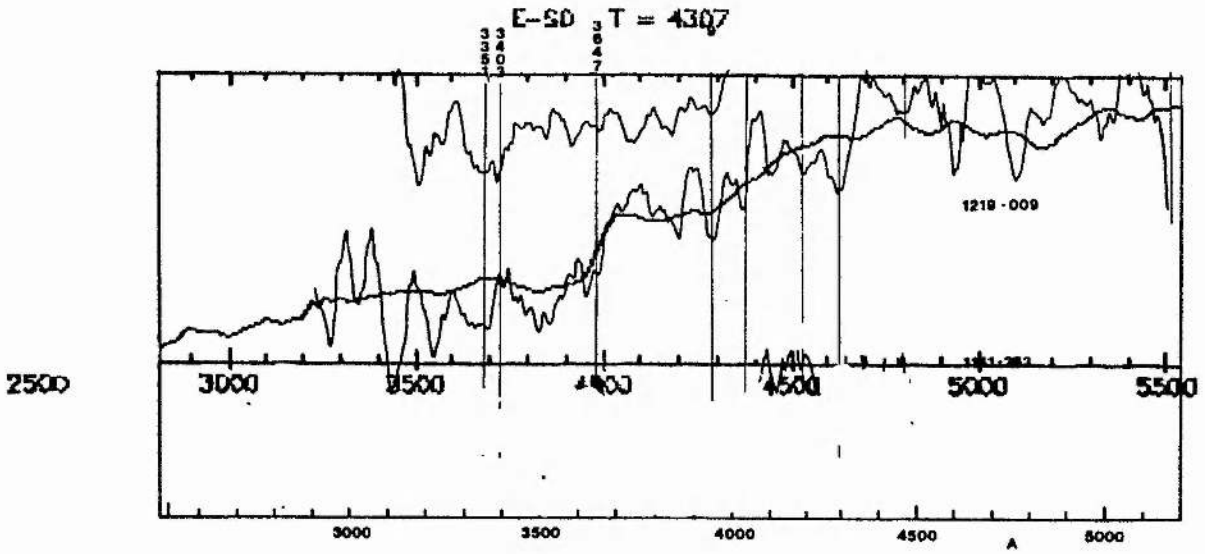

Figure 6.19: Pence superimposed on 1219-009 with 1219-009 blueshifted By ≈ 310 A.

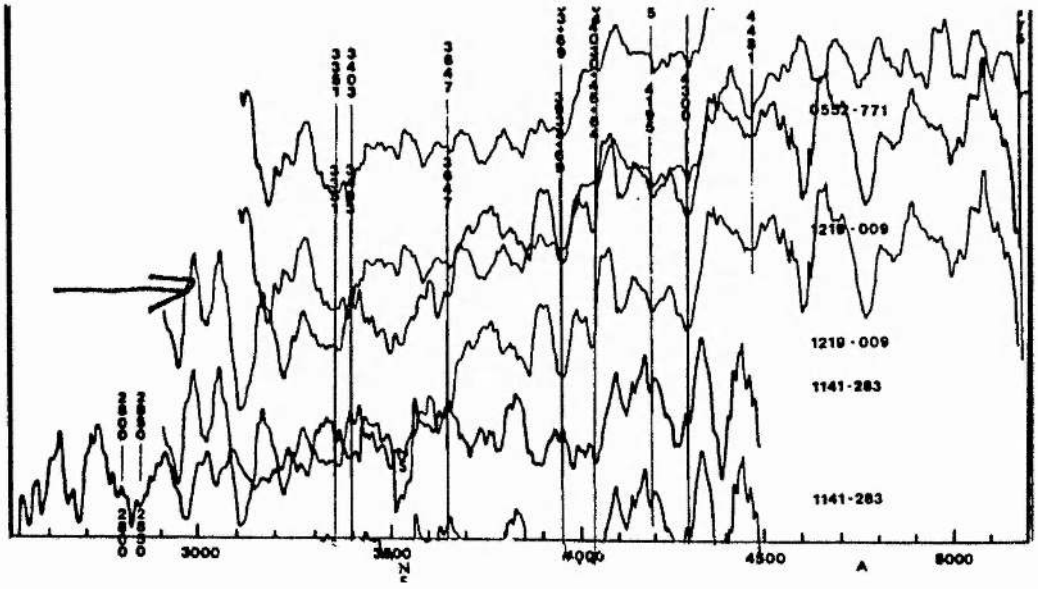

Figure 6.20: 0552-771 directly superimposed on 1219-009.

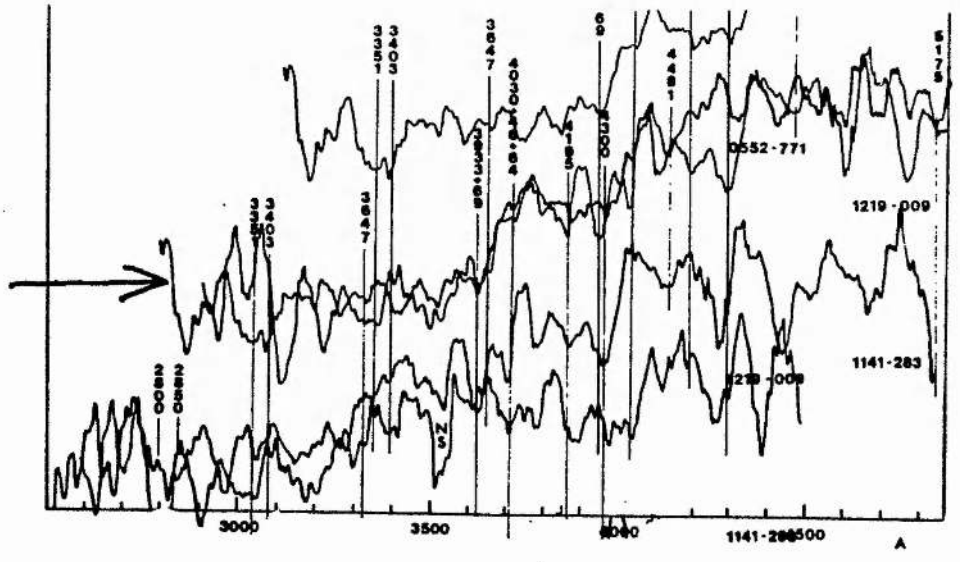

Figure 6.21: 0552-771 superimposed on 1219-009 with a 310 Å shift.

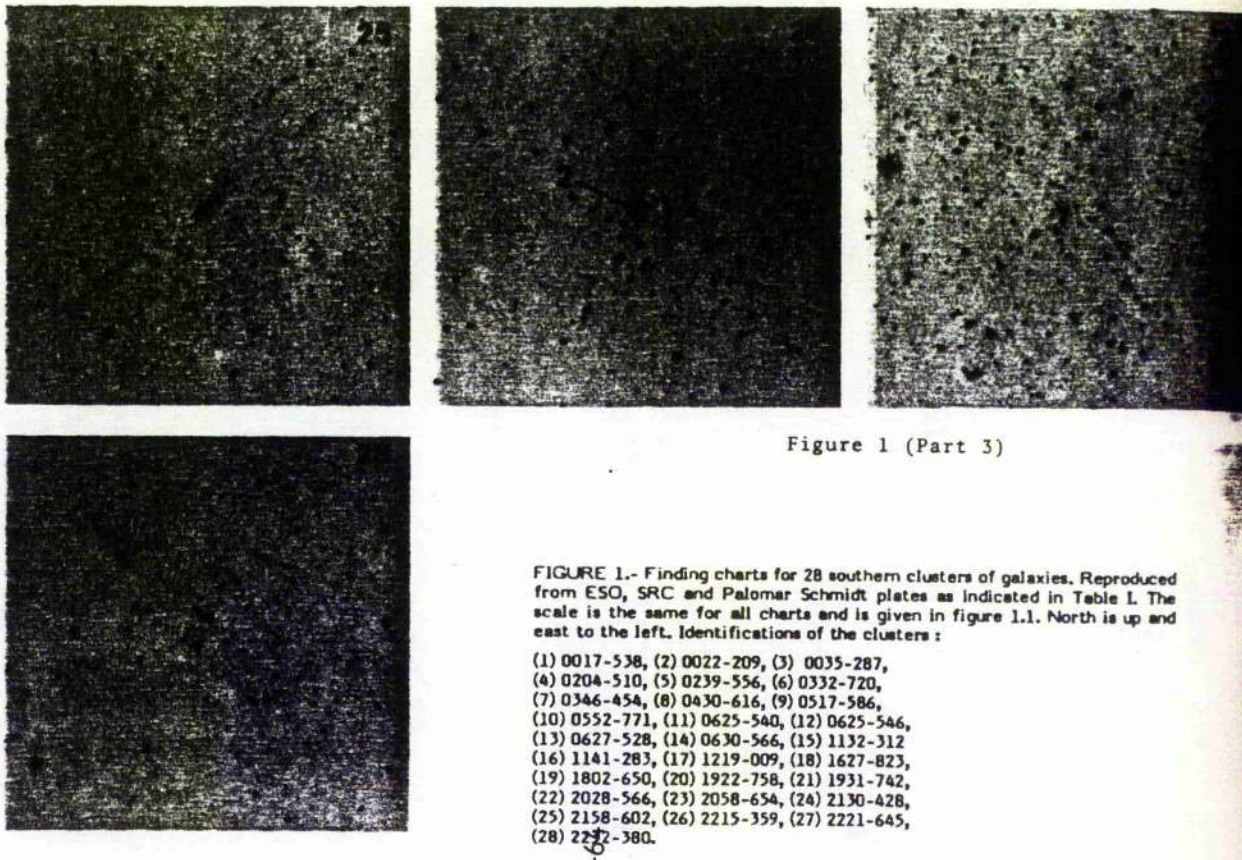

Figure 1 (Part 3)

FIGURE 1.- Finding charts for 28 southern clusters of galaxies. Reproduced from ESO, SRC and Palomar Schmidt plates as indicated in Table I. The scale is the same for all charts and is given in figure 1.1. North is up and east to the left. Identifications of the clusters :

(1) 0017-538, (2) 0022-209, (3) 0035-287,
(4) 0204-510, (5) 0239-556, (6) 0332-720,
(7) 0346-454, (8) 0430-616, (9) 0517-586,
(10) 0552-771, (11) 0625-540, (12) 0625-546,
(13) 0627-528, (14) 0630-566, (15) 1132-312
(16) 1141-283, (17) 1219-009, (18) 1627-823,
(19) 1802-650, (20) 1922-758, (21) 1931-742,
(22) 2028-566, (23) 2058-654, (24) 2130-428,
(25) 2158-602, (26) 2215-359, (27) 2221-645,
(28) 2242-380.

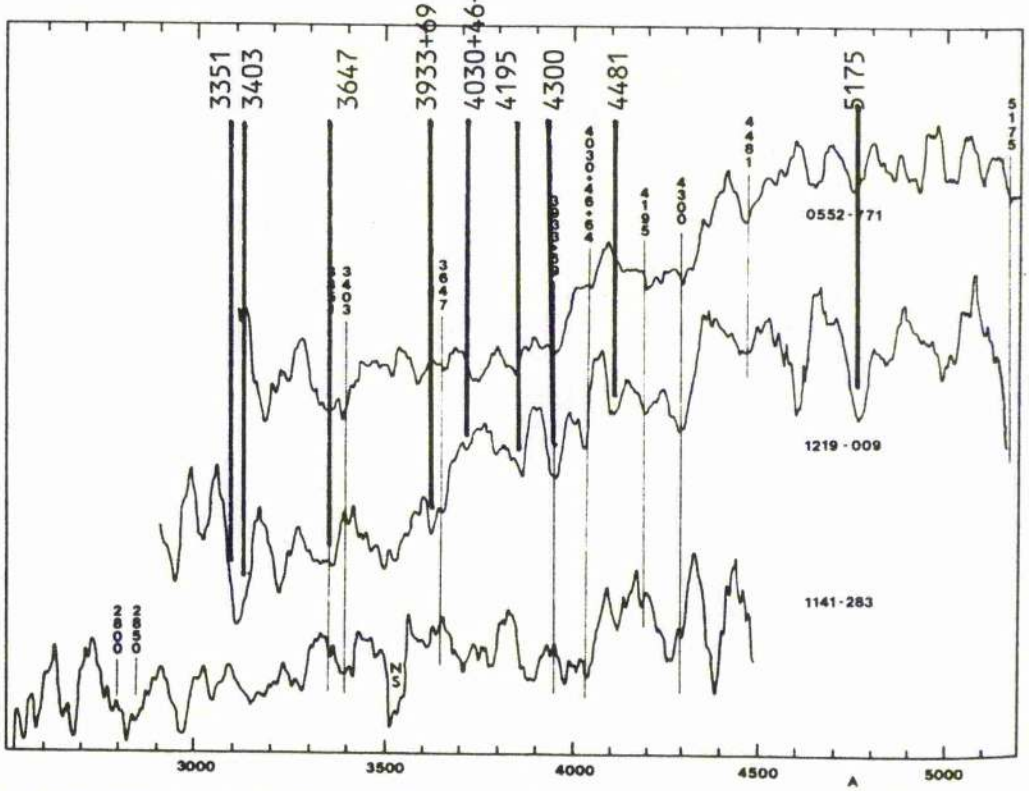

FIGURE 2.- Three spectra with high redshifts : 0552-771 (z = 0.27), 1219-009 (z = 0.37) and 1141-283 (z = 0.58). The spectra have been reduced to relative flux, heavily smoothed (by a 50 point = 50 A sliding mean) and shifted to zero velocity. The lowest spectrum is noisy and not representative of the normal S/N-level. Some of the stronger features (cf. Table II) have been indicated.

Figure 6.22: Re-identificaton of features in 1219-009.

strongest in the presented diagram. At any random point in the diagram, there will be a local fluctuation with which a supposed feature may be associated. It is suggested that some of the "features" were identified **after** the approximate redshift had been decided, and actually add little weight.

(iii) Comparison with Standard Rest Galaxy.

W&F's figure 2 is compared with the standard E-S0 energy distribution of Pence (1976). Figure 6.17 shows Pence superimposed on 0552-771. It can be seen that although most small features are not present in Pence, the overall shape is quite similar.

Figure 6.18 shows Pence overlaid on 1219-009. Now the overall shape is not such a good match. Supposing that a complete mistake has been made by W&F, figure 6.19 shows Pence again superimposed on 1219-009, but with 1219-009 blueshifted by about 310 Angstroms. Now the overall fit is much better.

The experiment is repeated using W&F's two top galaxies in their figure 2. Figure 6.20 shows 0552-771 superimposed on 1219-009 with no further shift; figure 6.21 has 1219-009 blueshifted by, again, about 310 Angstroms. Strictly, such shifting should be done in log space, but without access to the original data that cannot be done.

It is suggested, then, that W&F's value of z is too large by 310/4000 = 0.0775 for this object. Assuming the lower value for z, figure 6.22 shows the re-identification of the primary features. These identifications are at least as convincing as the original ones.

(iv) Conclusion.

Without external data, nothing can be proved. However, It seems that what is happening is that the techniques of West and Frandsen suffer from the same problem, perhaps to a lesser extent, as that suffered by methods of redshift determination from objective prism plates. That is, if the redshift estimate is in the right region, it has high precision; however, if the wrong region is chosen, then another, incorrect, answer still looks convincing. In the objective prism case, this problem is overcome by measuring tens of galaxies in a cluster, so that the large fraction of correct values dominates the scattered "mistakes". On the other hand, measures of only one or two galaxies in one cluster gives no such safty net. Visual inspection of the finding-chart photographs in West and Frandsen's paper makes a greater redshift than z = .12 seem quite reasonable for cluster 2215-359.

The conclusion must be that just because redshifts are produced from slit spectra, does not lead to unquestionable results. For this work, the main use of the redshifts is in determining the relative proximity of the clusters. A zero-point error, therefore, is not too serious, although the absolute value is used to produce secondary results. The values obtained using the techniques in this chapter will be used.

The interactive package, developed on the Nova computer and using Joyce Loebl-scanned data, was used with the zero-velocity galaxy template to provide a cluster galaxy with an absolute value of redshift; the more automatic APM/VAX system was then used to measure

velocities of all galaxies relative to that one. The results of the radial-velocity determinations are presented in the concluding chapter.

CHAPTER VII

Concluding Remarks.

Summary.

The aim of this work was to derive distances to a group of three clusters of galaxies to determine their spatial separation. Visually, they appear close enough to each other to be a supercluster, but of course this may be a projection effect.

Two basic lines of attack have been used:

(i) photometric method using broadband UBVR passbands, and

(ii) radial velocity determination, assuming the clusters to lie in a uniform Hubble flow.

(Photometric and redshift values for a few members of each cluster are tabulated along with corresponding finding charts in appendix A).

The photometric methods used were the comparison of monochromatic apparent luminosity functions, and the (U-R) colour-absolute magnitude calibration. Actually, both categories (i) and (ii) further sub-divide into two; for the immediate aim of the project, relative comparisons are more precise than absolute ones. However, an absolute determination of the distances is not only interesting, but comparison of photometrically derived distances with spectroscopically derived radial velocity leads to a determination of Hubble's constant.

Luminosity Function.

In the introduction several methods of using the luminosity

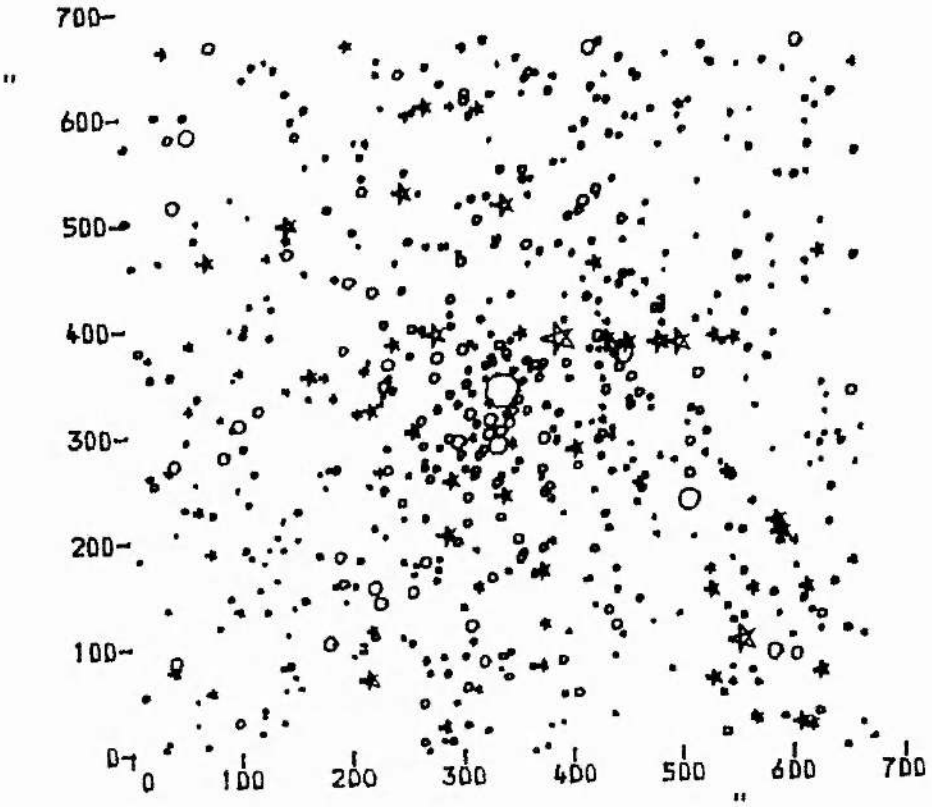

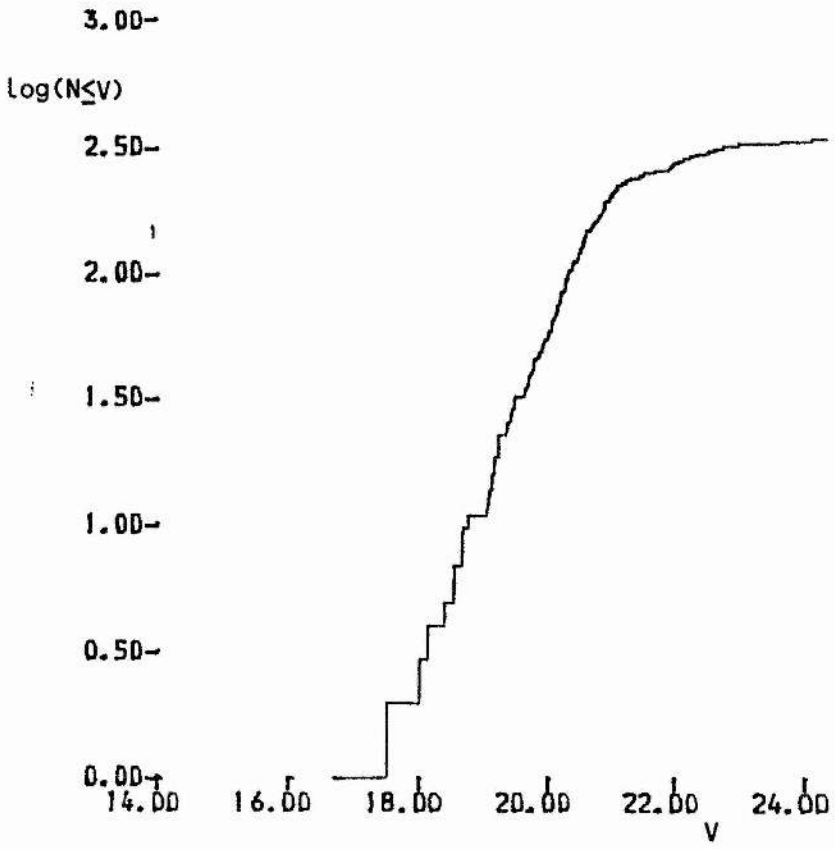

Figure 7.1: Map and cumulative luminosity function of cluster 1.

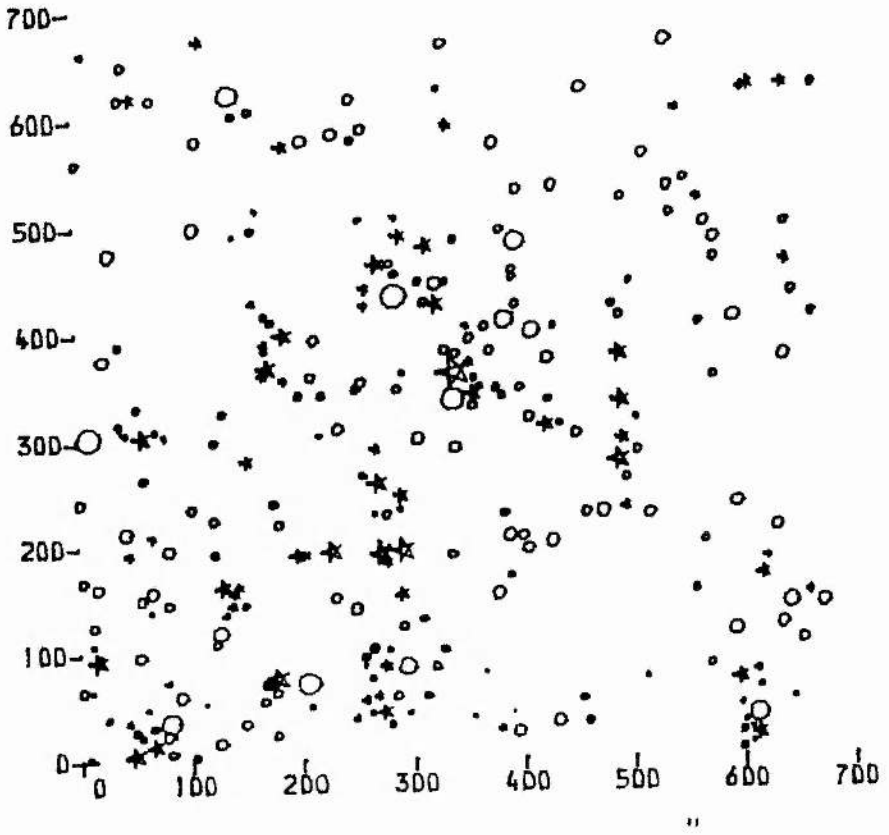

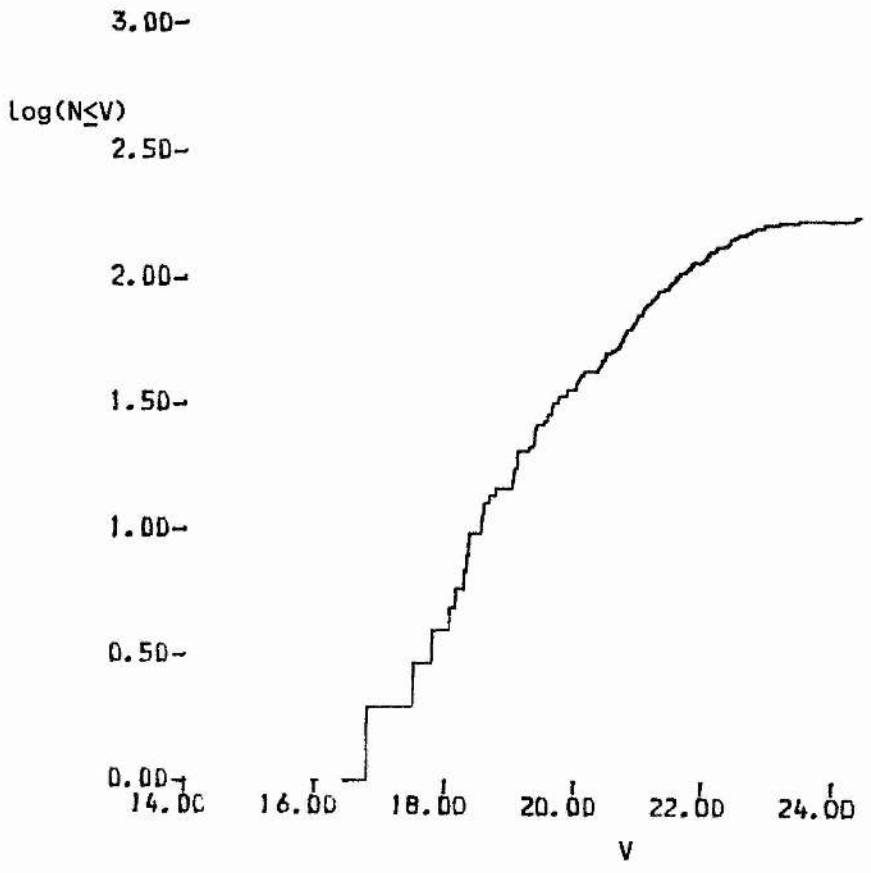

Figure 7.2: Map and cumulative luminosity function for cluster 2.

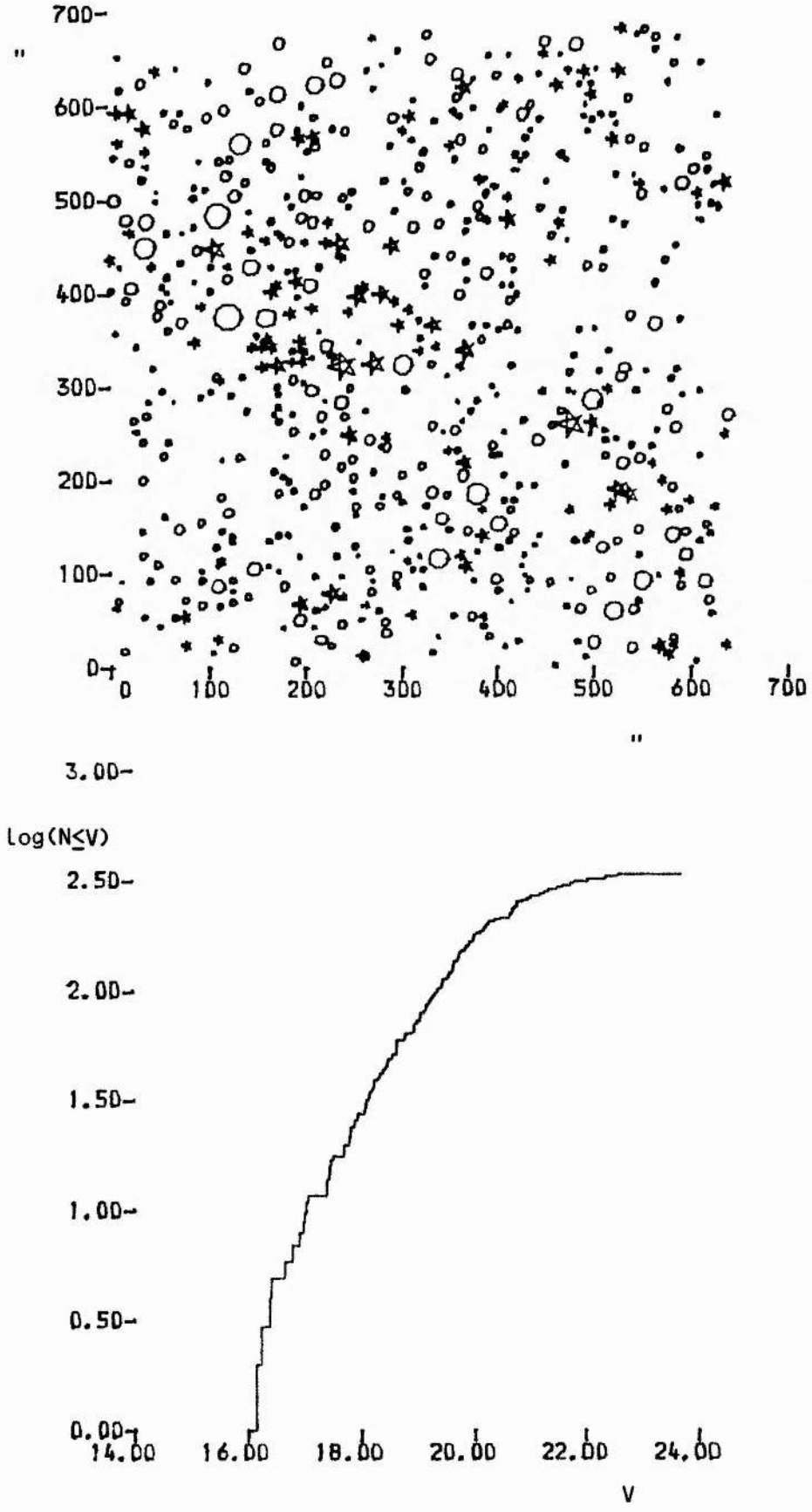

Figure 7.3: Cluster 3.

function as a distance indicator were outlined. Figures 7.1 to 7.3 show maps of the three clusters together with their corresponding background-corrected cumulative luminosity functions.

Although an image was only counted as real if it appeared on at least two plates, it is certain that the very faintest few objects are spurious. Further, there will probably be an incompleteness problem fainter than about twentieth magnitude. At the bright end, the functions are somewhat quantised by the nature of their definition, and, as noted in chapter I, may be distorted by on-going evolutionary effects.

These deviations from a simple ideal situation lead to the rejection of parameterised methods of comparing functions. The use of the the n^{th}-brightest galaxy is rejected, because it obviously depends on the richness apart from more subtle factors; the Abell dual-slope function just does not seem to fit the data here, either just because of the limitations of the data mentioned above or in fact because it is physically incorrect in this case. The more flexible Schecter function would also tend to be compromised by data incompleteness.

There is a further, philosophical argument. Parameterisation necessarily destroys information, and unnecessarily simplifies the hard won data. So a non-parametric approach is adopted in this work. To compare the luminosity functions of two clusters, essentially the brightest galaxy in one is plotted against the brightest in the other, the second brightest against the corresponding second brightest and so on.

Figure 7.4 displays such diagrams for the three possible

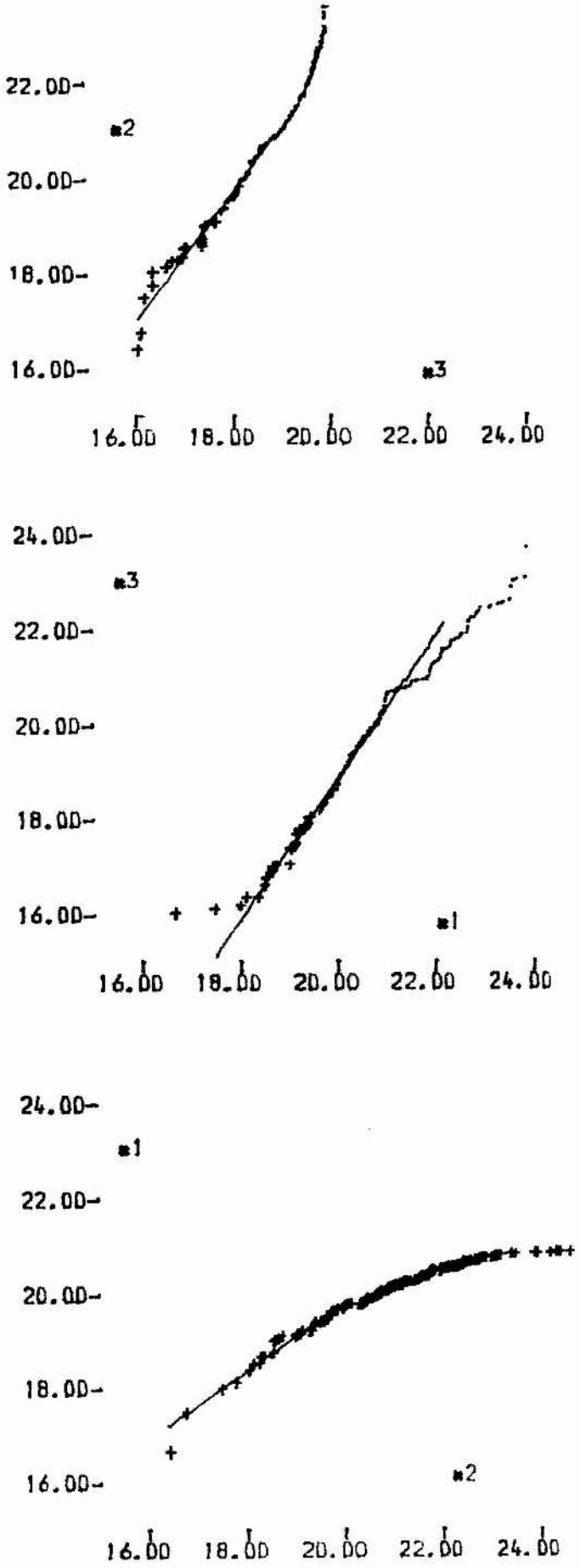

Figure 7.4: The luminosity functions of the three clusters inter compared.

combinations of the three clusters. If all clusters were identical in every respect, these plots would be forty-five degree lines. Because of varying incompleteness the faint ends fluctuate and, perhaps because of evolutionary effects, the bright ends turn drastically over the last two or three points. However, between these two extremes there are runs of well-measured, complete samples of magnitudes which lie very close to a straight line. The gradient of this line is a measure of the relative richness of the two clusters concerned, and the zero-point difference indicates the relative distances. The actual measure of the zero point is taken at the place where the brightest pair of galaxy magnitudes join the linear section.

The parameters of the lines plotted in figure 7.4 are:

clusters	points	gradient	intercept	rms residual
1 vs 2	42	0.729	5.226	0.129
3 vs 1	200	1.468	-10.558	0.066
2 vs 3	70	1.350	- 4.622	0.167

Using the reference point mentioned above, the result is that cluster 2 is 0.61 magnitudes nearer than cluster 1, and cluster 3 is 1.43 magnitudes nearer than cluster 1. Translating into relative distance, if cluster 1 is at unit distance, $d_2 = 0.94$ and $d_3 = 0.85$. The test of the supercluster hypothesis will be whether the radial separation of the clusters is similar to their projected separation.

But first the analysis of the luminosity functions is completed by deriving absolute distances to the clusters.

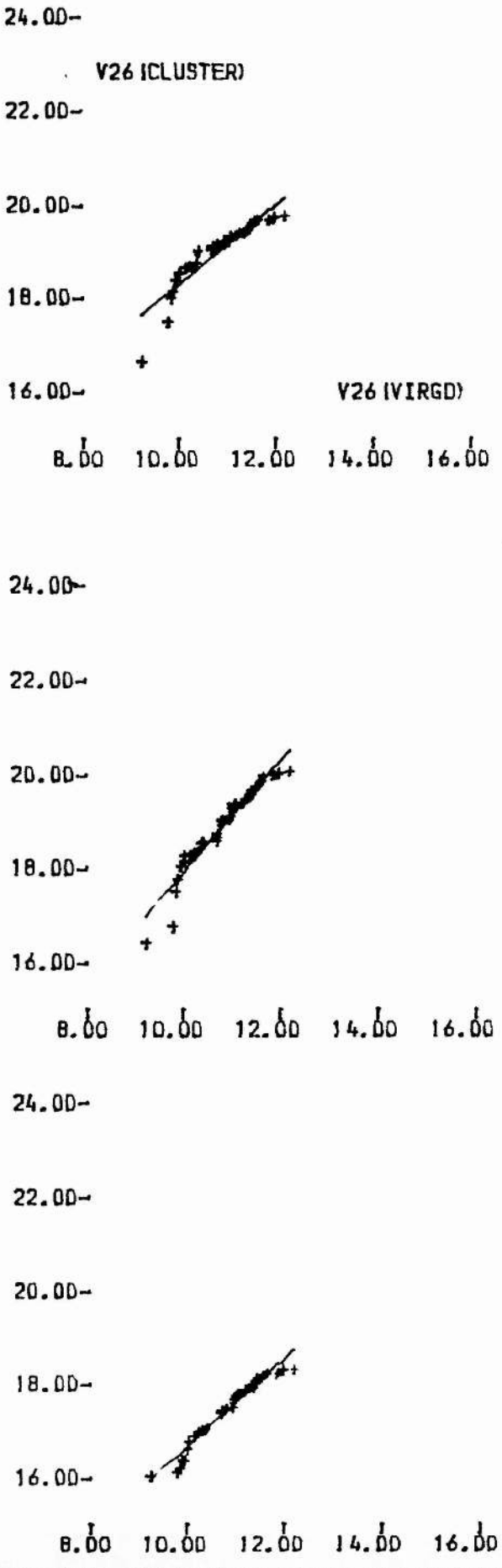

Figure 7.5: The luminosity functions of the three clusters compared with the Virgo cluster.

Comparison with Virgo cluster.

Visvanathen and Griersmith (1979) give V_{26} magnitudes for a number of galaxies in Virgo I. Selectingthe E-SO galaxies the same method as for relative cluster distances can be performed. Figure 7.5 shows the brightest 42 galaxies in each cluster plotted against the corresponding Virgo galaxies. The parameters of the lines are:

cluster	points	gradient	intercept	rms residual	m-M (Virgo)
1	42	.848	9.794	.23	8.27
2	42	1.183	6.049	.22	7.81
3	42	0.926	7.384	.14	6.64

using the above authors' value for the distance modulus of Virgo, which is 31.26 $\pm$ 0.16, the absolute values for the other clusters are:

cluster	m-M	d/Mpc
1	39.5	800
2	39.1	650
3	37.9	380

The errors are hard to quantify since Virgo is much less rich than the clusters under study, and may therefore be composed of intrinsically different galaxies. Certainly, the comparison above is not as tight as the relative comparison of the three. Assuming there may be a 0.4 magnitude zero point error in V as a result of extrapolation from the photo-electric sequence, and combining this with

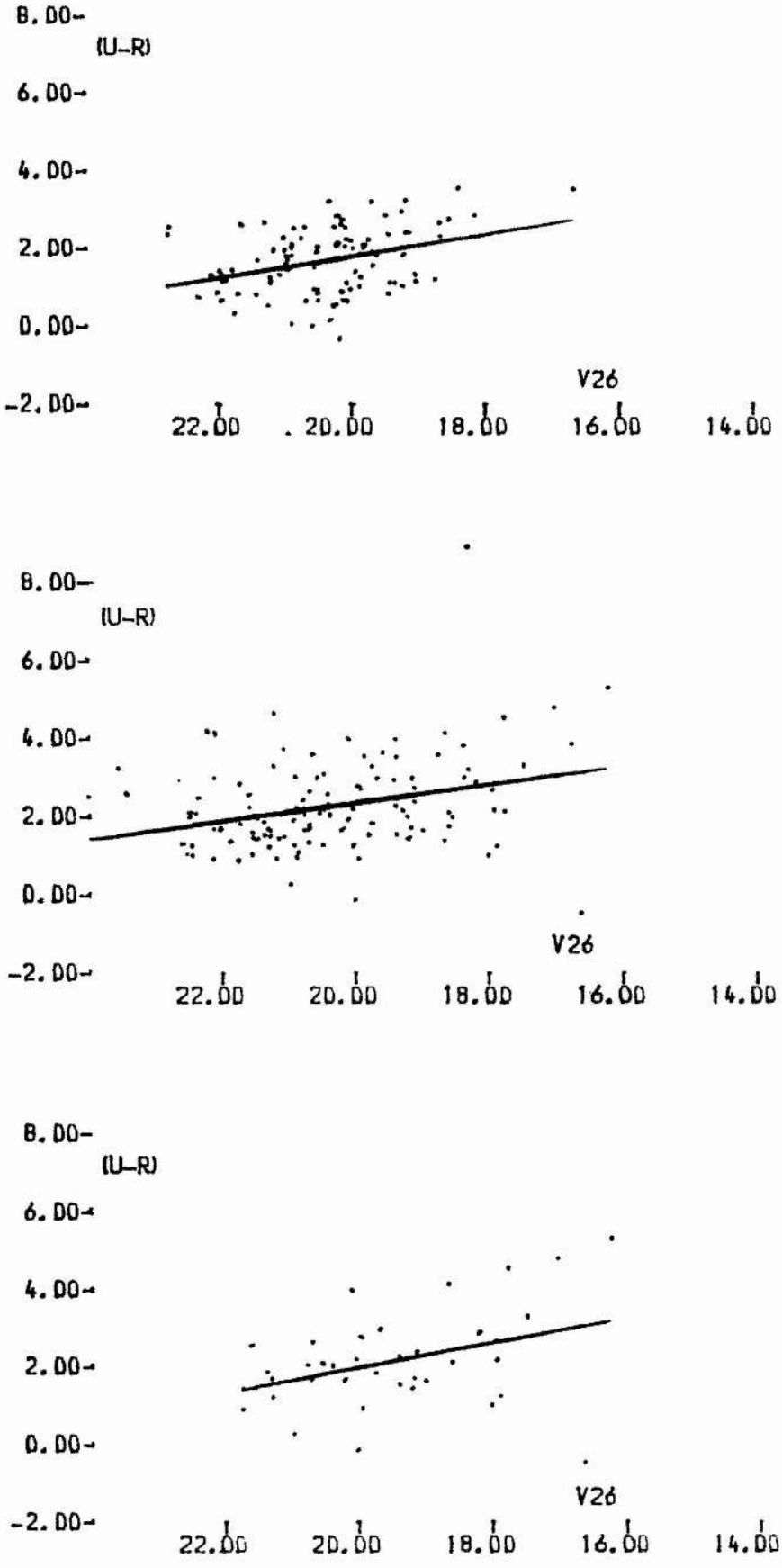

Figure 7.6: (U-R) vs V_{26} for the three clusters showing Strom's absolute-magnitude calibration.

the .2 magnitude rms errors in the Virgo fits, and with the 0.16 error in the distance modulus of Virgo quoted by Visvanathan and Griersmith, the total error may be 0.5 magnitudes.

(U-R) calibration.

The 'Strom effect' is quoted as (U-R) = 0.24 - 0.101 M_V. For an observation of a cluster we obtain (U-R) = C - 0.101 V where C is a constant. Subtracting the two gives

$$V - M_V = m - M = 9.90C - 2.38$$

When expressed in this way it can be seen that the error in the observationally derived constant C will be multiplied by nearly ten in determining the distance nodulus. Nevertheless, it is still worthwhile as an independent method. Figure 7.6 shows the (U-R), V diagrams for the three clusters. The results are as follows:

cluster	C	m-M	d/Mpc
1	3.76	34.9	95
2	4.37	40.9	1500
3	4.14	38.6	520

Given an uncertainly in (U-R) of 0.4 magnitudes, the errors in m-M will be 4 magnitudes. The standard deviation of the distance moduli of the three clusters is 3.0 magnitudes. So this test above cannot help the problem of how relatively close the clusters are.

Redshifts.

Redshifts have been determined as described in Chapter VI for all galaxies in the three clusters, and the distribution of z for each is shown in Figure 7.7. It must be remembered that the relative shifts are valid over a small range. Outside this range, spectra tend to correlate with the wrong features, leading to a value of z which is 'folded' into the valid range. Because of this the histograms are somewhat contaminated.

A technique for locating and parameterising the core distribution, that is, the low-dispersion, visually obvious part of the histograms, is as follows. Firstly, the mode is found. Secondly, the distribution is searched in both directions from the mode, until a bin is found in which the count **increases;** the contribution of correctly-measured cluster members is then assumed to lie mainly within these limits. The position of the peak is determined by parabolic interpolation, that is, a parabola is fitted by least squares to the logarithm of the bin values in the core distrbution, and the postion of the peak taken to be at the maximum of the parabola. Finally, the dispersion is determined as that width which encloses 63% of the area of the core distribution. The results are:

cluster	z	apparent dispersion
1	0.144	0.011
2	0.166	0.012
3	0.166	0.020

where the dispersions are rather rough estimates due to the

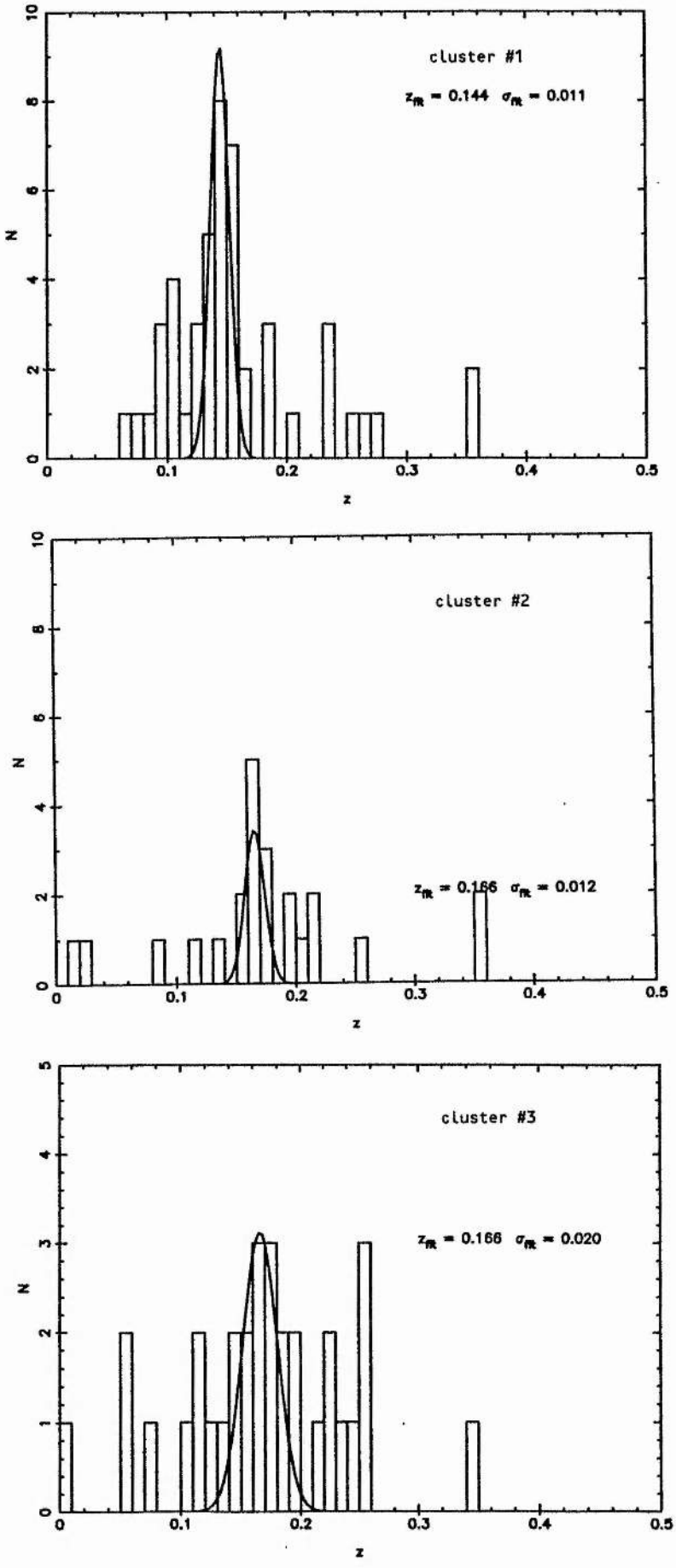

Figure 7.7: Distribution of Redshifts in the three cluster fields.

contamination problem. The relative distances, where again cluster 1 is given unit distance (and for this purpose it must be assumed the three clusters lie in a uniform Hubble flow) are $d_1 = 1.000$, $d_2 = 1.152$, and $d_3 = 1.152$. Strangely, these distances are in the opposite sense to the relative distances derived from the photometry. It is tantalising to speculate that this anomaly may be due to gravitationally modified motion within a supercluster. With this in mind, a virial analysis is carried out in a following section.

It is interesting to compare the distributions in figure 7.7 with the theoretical selection function, derived by MacGillivray and Dodd (1982). They assumed that the selection of objects was on a machine threshold criterion, whereas the selection in this work was effectively on $V_{total} = 18$. Since MacGillivray & Dodd achieve similar results from simulations thresholded at 2% and 10%, it may be assumed that the V_{total} selection will render similar results. Qualitatively, the histograms in figure 7.7 are narrower, and peak at a lower value of z, than the selection function of MacGillivray and Dodd. Therefore, the distributions in figure 7.7 are taken to be dominated by cluster members, and not a reflection of the overall selection function.

The significance of the differences between then observed distributions of redshifts can be established by a series of statistical tests, in order to quantitatively decide whether the three cluster samples come from the same population, as would be expected if they were part of a supercluster at the same cosmological distance.

Statistical Comparison of Redshift Determinations.

(i) Parametric hypothesis testing under the assumption of normality:

Assuming the redshift samples to be normally distributed, the first objective is to establish the significance of the variances of the three data sets.

Bartlett proposed a statistic, "B/C" (eg Brownlee 1960, p292) to test for the equality of several variances, which has an approximately $\chi^2(k-1)$ distribution. Using the 103 redshift values for the three clusters, tabulated in table 7.1, it is found that Bartlett's statistic B/C = 1.557. For two degrees of freedom, χ^2 is 1.557 at about the .55 point, and so the null hypothesis, that the variances are equal, cannot be rejected.

Given equal variances, it is now valid to proceed to the next step, which is to compute the F-ratio to test the significance of the mean values of z in each group with the global mean. The F-ratio is the ratio of the group mean square residual to the global mean square, and from the data it is found that F = 0.3788 with degrees of freedom $\nu_1 = 2$ and $\nu_2 = 100$. The probability for $F(\nu_1,\nu_2) \geq 0.3788$ is 0.6857, and the null hypothesis of equal means cannot be rejected on this test.

(ii) Non-parametric (distribution-free) hypothesis testing:

The two preceding tests have assumed normality, but this may not be valid. Although true cluster members which have been correctly measured will share an approximately normal distribution, field galaxies will be distributed as the skew selection function, and those

1		0.0041
2	0.0107	
3	0.0212	
4		0.0517
5		0.0551
6	0.0691	
7		0.0760
8	0.0793	
9	0.0819	
10	0.0898	
11	0.0918	
12	0.0979	
13	0.0985	
14	0.1008	
15	0.1017	
16		0.1033
17	0.1034	
18	0.1098	
19		0.1109
20	0.1120	
21	0.1157	
22		0.1170
23	0.1227	
24	0.1236	
25	0.1260	
26		0.1286
27	0.1304	
28	0.1330	
29	0.1354	
30	0.1356	
31	0.1360	
32		0.1387
33	0.1395	
34	0.1419	
35		0.1422
36	0.1435	
37	0.1436	
38		0.1448
39	0.1451	
40	0.1456	
41	0.1458	
42	0.1486	
43	0.1486	
44	0.1504	
45	0.1509	
46	0.1515	
47		0.1525
48	0.1549	
49	0.1562	
50	0.1582	
51	0.1591	
52		0.1592
53	0.1597	
54	0.1599	
55		0.1605
56		0.1609
57	0.1621	
58	0.1623	
59	0.1638	
60	0.1654	
61		0.1658
62	0.1658	
63	0.1662	
64	0.1664	
65	0.1705	
66		0.1710
67		0.1711
68		0.1730
69	0.1756	
70	0.1798	
71		0.1803
72	0.1818	
73	0.1824	
74		0.1854
75	0.1890	
76		0.1907
77	0.1916	
78	0.1924	
79		0.1937
80	0.2010	
81	0.2047	
82	0.2110	
83	0.2112	
84		0.2172
85		0.2268
86		0.2284
87	0.2320	
88		0.2334
89	0.2369	
90	0.2383	
91		0.2489
92		0.2538
93		0.2546
94	0.2557	
95	0.2557	
96		0.2574
97	0.2627	
98	0.2795	
99		0.3463
100	0.3509	
101	0.3535	
102	0.3554	
103	0.3583	

Table 7.1: The set of 103 redshift values, shownwith overall ranking, as required by the computation of the Kruskall-Wallis statistic. The three columns list clusters 1, 2, and 3.

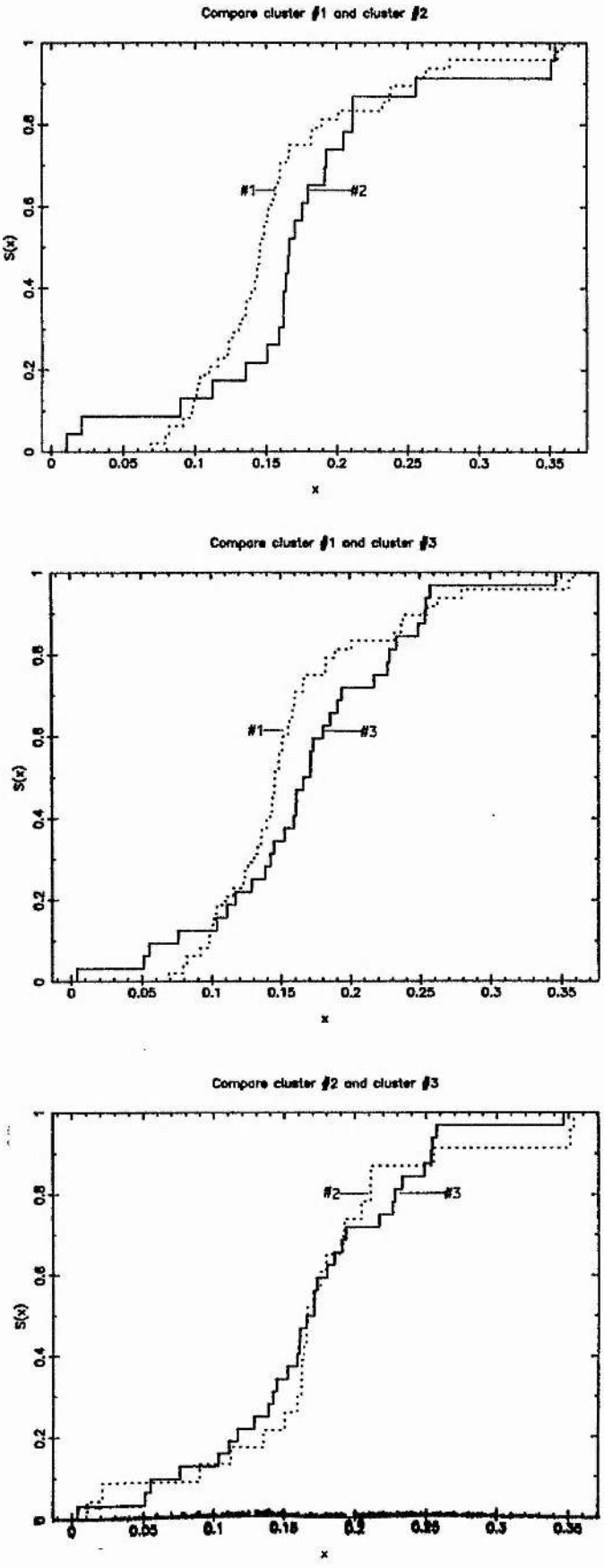

Figure 7.7a: Comparison of the three combinations of empirical distribution functions for the redshift values in each cluster field.

objects with incorrect z values will be distributed erratically. Therefore, it may be considered more realistic to adopt a non-parametric hypothesis-tesing approach.

Non-parametric tests are based on the empirical distribution function (e.d.f) formed by normalising the cumulative distribution function, or the ranks of the measured quantities, ie their order without regard to actual value. Figure 7.7a shows the e.d.f.s of the three clusters superimposed in the three possible combinations, for visual comparison.

Whereas in the previous case, it was neccessary to establish equality of variances before the test for equality of means was valid, in the non-parametric case the reverse is true, that is, firstly the hypothesis of equal location must be proved before tests of variance are meaningful.

Two tests of location are used. The Kruskal-Wallis test investigates the differences between scores from k independent samples of unequal sizes, and tests for differences in location but not dispersion. The Rank-sum test of Wilcoxon (sometimes referred to as the Mann-Whitney test) tests the difference between the medians of two independent samples, and so is also a test of location. The Fisz-Lehmann-Rosenblatt test (sometimes referred to as the Cramér-von Mises Two-Sample Test) tests two samples for differences in both location and dispersion, but if equality of location has been confirmed, then this is a test of variance. The k-sample test has greater power than multiple testing using two-sample tests, although the two-sample tests can indicate where in the group of three clusters any differences actually lie.

The Kruskal-Wallis k-sample test statistic H approximately follows a χ^2_{k-1} distribution. It is found from the data that H = 3.760. The probability of at least H being observed is 0.153, or the null hypothesis that the populations are the same could just be rejected at the .15 confidence level, and so at the usual 0.05 level, the null hypothesis cannot be rejected.

The Wilcoxon test involves ranking the pooled sample of two groups, average ranks being used for ties. The test statistic U is the number of times a score in the first sample precedes a score in the second sample. In the comparison of cluster #1 and #2, it is found that U = 403. The probability, p, of observing a value of U not greater than 403 is .034. The null hypothesis that the medians are equal should be rejected, in the case where the alternate hypothesis is that the medians are not equal, when $p' = 2 \times \min(p,p-1) < \alpha$. For clusters #1 and #2, p' is 0.067, so those clusters cannot be considered to have different locations at $\alpha = 0.05$.

For cluster #1 and #3, U = 628, p = 0.085 and p' = 0.169. Thus again, these clusters are similar. Finally, #2 vs #3 give U = 380, p = 0.581, and p' = 0.838. In this case, cluster #2 and #3 match each other closely.

The Fisz-Lehmann-Rosenblatt statistic T (Conover, p314) is based on the sum of the square of the differences in e.d.f at each data point. In comparing cluster #1 and cluster #2, it is found that T = 0.589, with an associated probability of 0.013, and on this basis the clusters are significantly different to one another. Presumably, this is due to a diference in variance, having established equality of location. For cluster #1 and #3, T = 0.381 and p = 0.061, so the

hypothesis of equality cannot be rejected at the 0.05 level; and for clusters #2 and #3, T = 0.061 and p = 0.807. Again, these two are very similar.

Interpretation of statistics.

The above unbiased tests confirm quantitatively what may be expected from examining the histograms and cumulative distributions of the redshift values displayed in figures 7.7 and 7.7a. All available data were used in the tests, but as mentioned, these data sets are composed only partly of actual cluster members, properly measured. The rest are background objects sharing an identical distribution in each field, and mis-measured objects with erratic (not truly random), but again identical, distribution.

The conclusion is that the k-sample tests demonstrate that it is probable (F ratio, Kruskal Wallis) that all the data was drawn from the same population, and examination of pairs of clusters for location (Wilcoxon) also indicates that the clusters are at the same redshifts, while the F-L-R test indicates that cluster #1 is significantly different to the other two, although this will be due to dispersion difference. On the basis of redshifts, the above analysis supports the idea of a common distance to the three individual clusters.

Virial Mass.

The mass of a cluster of galaxies can be obtained if it is assumed the virial theorem applies to the cluster. In order for this assumption to be justified, the cluster must consist of a stable group of point masses in a relaxed system.

The virial theorem may be stated:

$$2T + \Omega = 0$$

where T is the time average of the kinetic energy and Ω is the time average of the potential energy. The kinetic energy is determined for a cluster from the radial velocities after an assumption is made about the mean velocity of the group as a whole, and correction is made for the component of the kinetic energy that is not seen in the line of sight. The potential energy is estimated, in terms of the unknown mass, from the separation of the individual members of the galaxies from each other. The method is formalised as:

$$M_{VT} = \frac{3 R_e \sigma_v^2}{G}$$

where M_{VT} is the virial mass estimate, R_e is the effective radius, σ_v is the line-of-sight velocity dispersion, and G is the gravitational constant.

Clearly, in this work, the velocity dispersion in the individual clusters cannot be determined. The total dispersion of the data is difficult to estimate, and so also is the large measurement error which must be deconvolved to obtain the actual velocity dispersion. Therefore, since an evaluation of the virial mass for the individual clusters would be based on guesswork, it is not attempted.

The situation for the supercluster as a whole, however, is rather different. The assumption of relaxation is likely to be less true than for individual clusters; it is not clear what value to use for R_e as the full extent of the supercluster is not known, and anyway it

might merge continuously into the field, and only three "points" are available; but finally the velocities of the clusters are known with reasonable precision, at least relatively, since the positions of the peaks of the cluster velocity distributions are well determined.

The radial component of the peculiar motion of each cluster is determined following Harrison's (1974) letter on the Interpretation of Redshifts of Galaxies in Clusters. In some literature, the measured radial velocity, V = cz, is interpreted to mean

$$V = -v_o + V_G + cz_R$$

where v_o is the radial component of our own peculiar velocity, V_G is the radial component of the peculiar velocity of the galaxy, and z_R is the cosmological redshift. Harrison demonstrates that the actual radial component of the peculiar velocity of a galaxy is not V_G but

$$v_G = (V_G + z_R v_o)/(1 + z_R).$$

The cosmological redshift, z_R, is taken to be the mean of the three cluster velocities; z_R = 0.159 and cz_R = 47600 kms^{-1}. The radial component of the peculiar velocities of the

clusters, v_G, can now be computed:

cluster	z	V	V_G	v_G
1	0.144	43200	-4400	-3797
2	0.166	49800	2200	1899
3	0.166	49800	2200	1899

The velocity dispersion, σ_v, is taken to be:

$$\sigma_v^2 = \frac{1}{n-1}\sum_n z_G^2$$

and it is found $\sigma_v = 3289$ kms^{-1}. The quantity R_e, as mentioned, is difficult to determine, but a value of 10 Mpc will be used. This value will be of the right order, and given the uncertainty of the applicability of the virial theorem, will suffice. These values for R_e and σ_v lead to the result:

$$M_{VT} = 7.5\times10^{16}\ M_\odot$$

This may be compared with a virial mass of about 10^{13} $M_\odot$ for the Coma cluster. If there were actually ten individual clusters in the supercluster, each ten times richer than Coma, and R_e has been overestimated by a factor of ten, then M_{VT} for the supercluster is still 7.5 times too high.

The most likely explanation of the result is that the supercluster is not in a gravitationally relaxed state, and so the virial theorem ought not to be applied to the system as a whole. An important future project will be to measure sufficiently accurate velocities of individual galaxies, compute the virial mass of the clusters, and then compare the sum to the virial mass for the supercluster.

Relative dimensions of the supercluster.

It is now possible to compare the relative radial distance of the clusters with their projected separation. If there is a supercluster one would expect the two separations to be comparable.

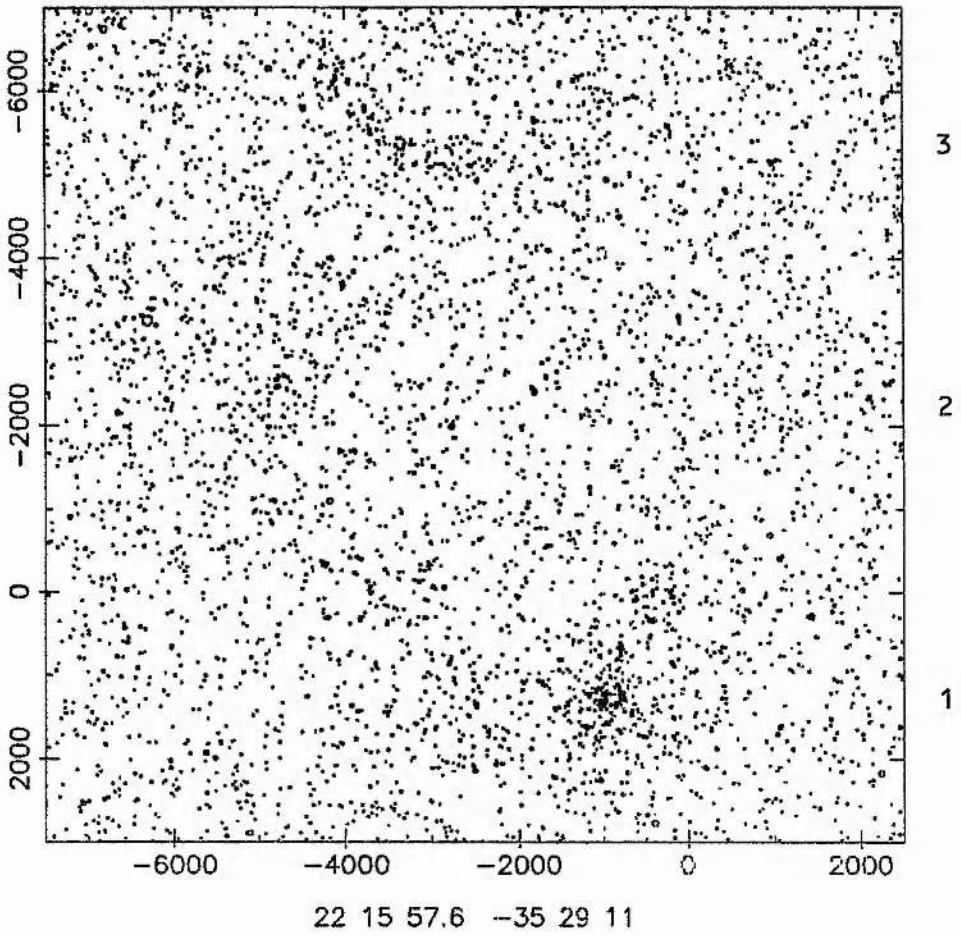

Figure 7.8: Map of the Supercluster region. The map is 12 x 12 Mpc at the distance of the supercluster.

Firstly, by using the luminosity function and radial velocity data, the mean relative distances are $d_1 = 1.0$, $d_2 = 1.05 \pm .11$ and $d_3 = 1.00 \pm 0.15$. The mean projected radius (PR) of the three clusters measured from their projected centroid is 0.49 degrees or 0.0085 radian. The root-mean-square relative distance with respect to radial centroid at $d_c = 1.017$ is 0.021. The ratio of these two numbers in the sense radial distance/projected distance is 2.5. This ratio is based only on comparative distances, which, it is maintained, are determined more accurately than absolute distances.

Therefore, on the basis of the observed spatial shape of this group of clusters, they are as physically close as their apparent distribution suggests.

Wide-Field Distribution.

The area of sky scanned with the APM was 4.8^{o}x 4.8^{o}, and this can be used to examine the large-scale distribution of galaxies across the supercluster field.

A map of all the objects classified by shape as galaxies has already been presented as figure 4.18. It is apparent by looking at that figure that there is a clumpy distribution of galaxies, and the three clusters of this study are particularly prominent. To get a more quantitative measure of the overall galaxy distribution, three "slices" have been taken from the data set. Each slice is 1000 pixels wide, and their positions and orientations are shown on figure 7.9. They were chosen to (i) include cluster #1 & cluster #2; (ii) to include cluster #1 and cluster #3; and (iii) to include cluster #2 and run horizontally

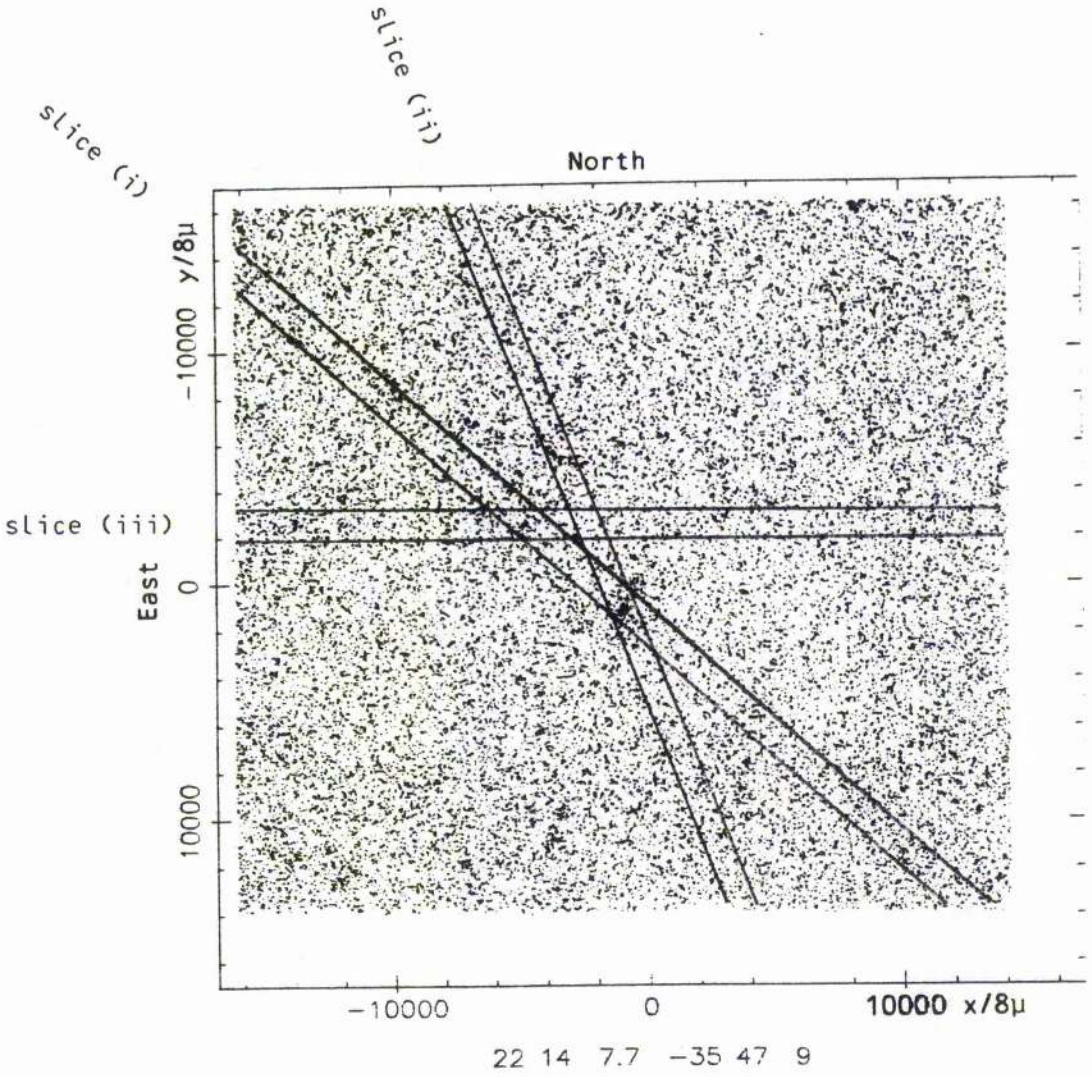

Figure 7.9: Slices used to compile galaxy counts shown in the next figure.

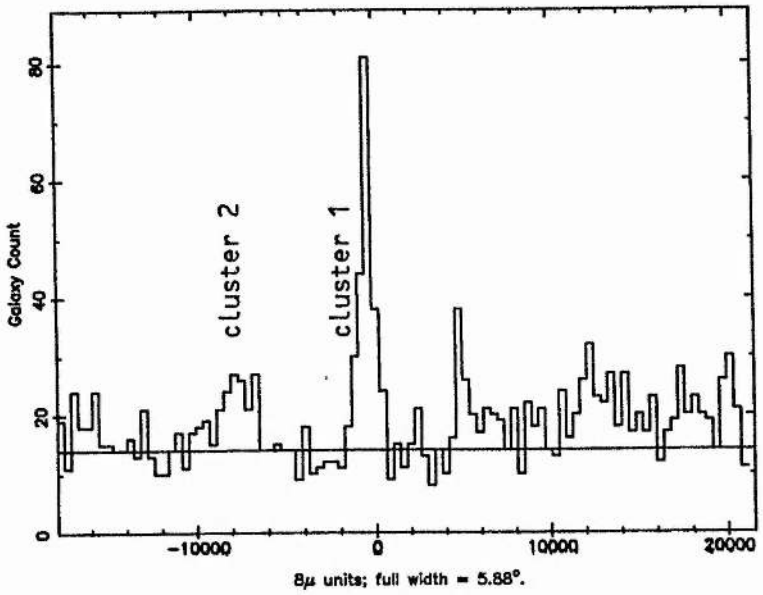

Figure 7.10: Galaxy counts in strip (i).

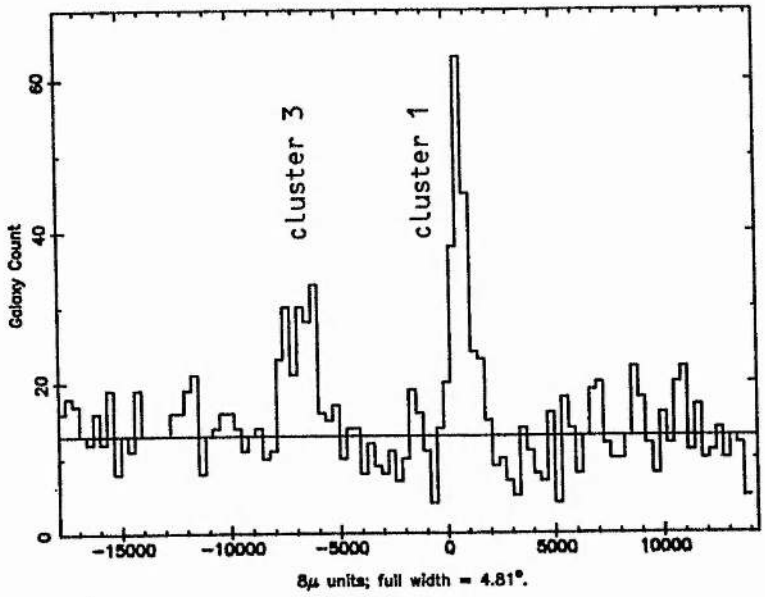

Figure 7.11: Galaxy counts in strip (ii).

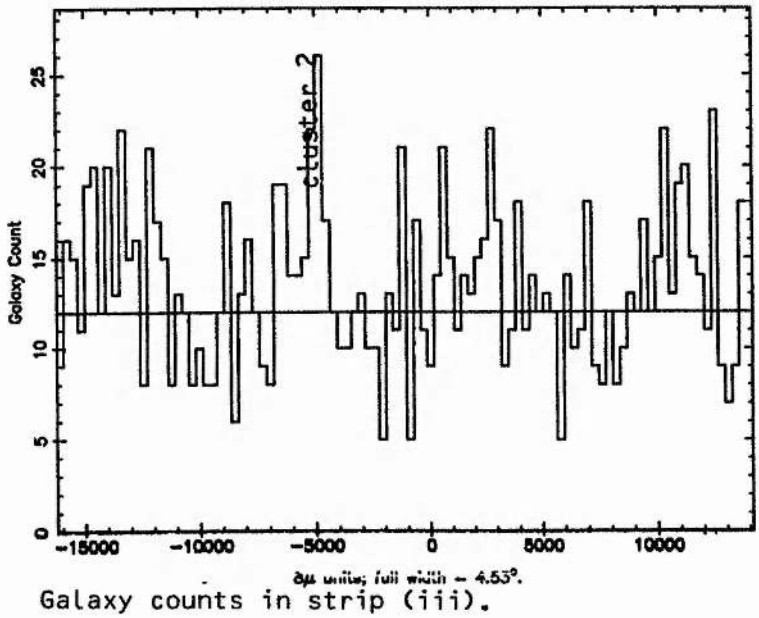

Figure 7.12: Galaxy counts in strip (iii).

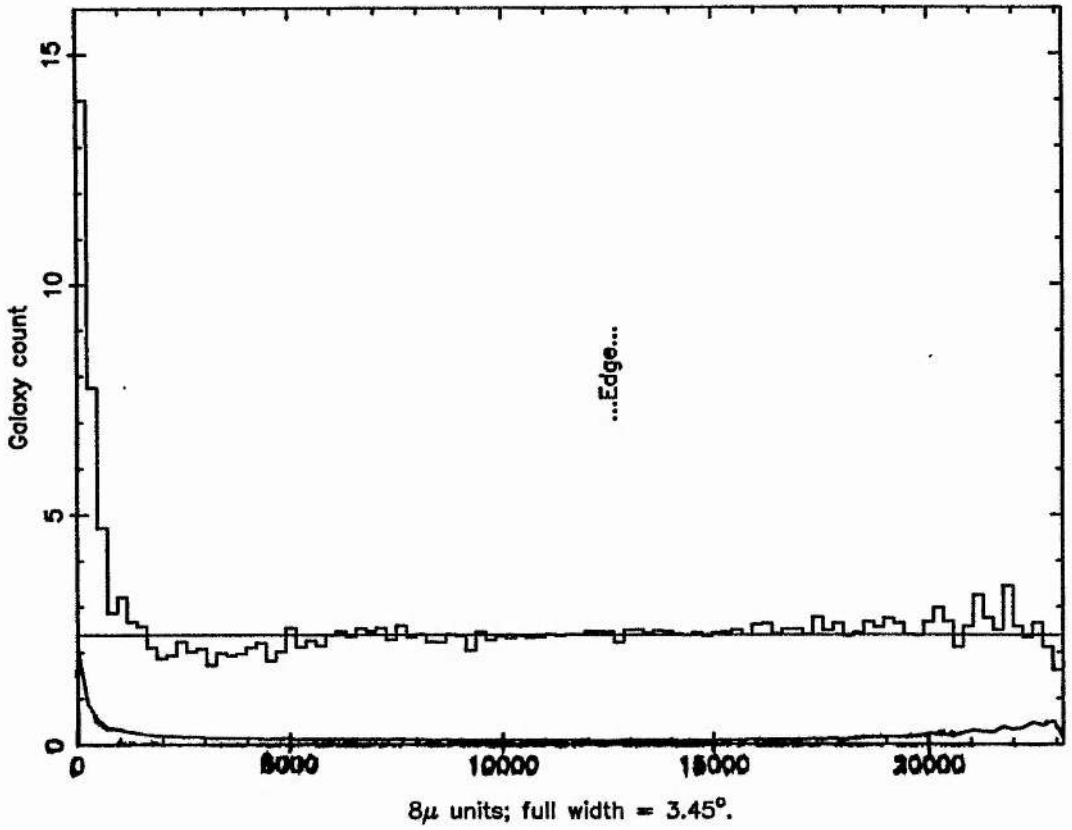

Figure 7.13: Ring counts of galaxies, centred on cluster #1. The smooth curve at the bottom is the corresponding error at each bin.

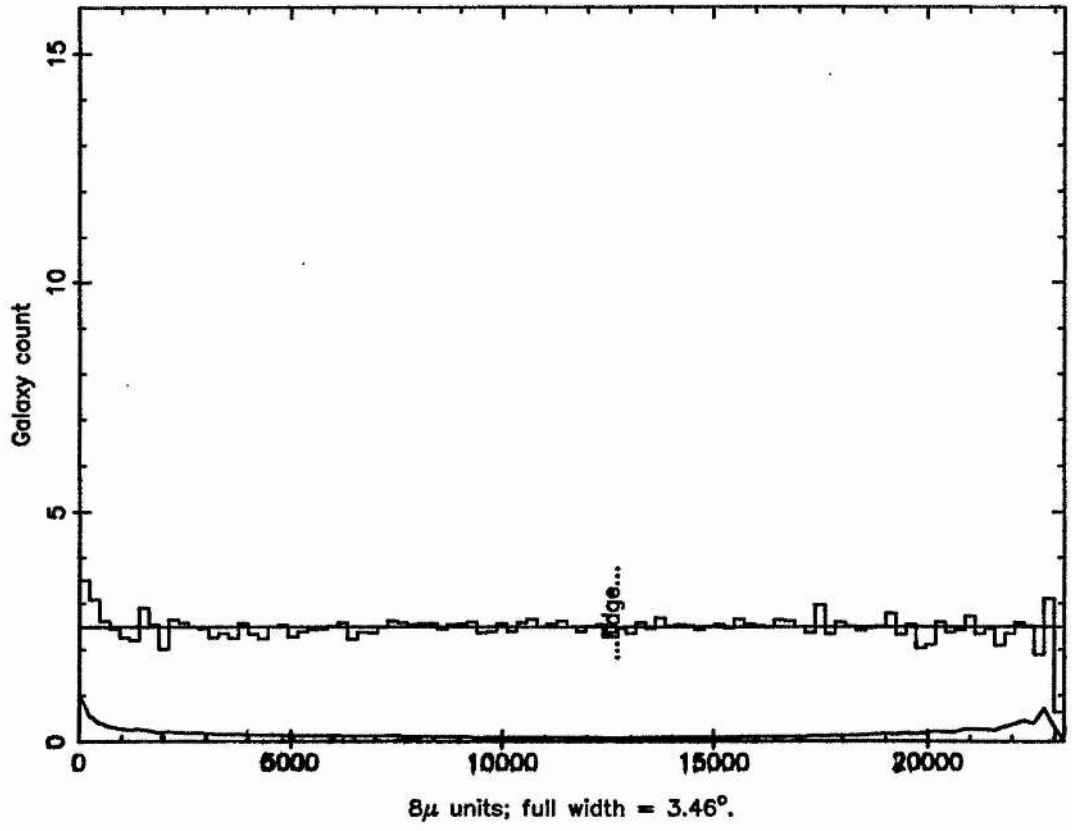

Figure 7.14: As above, but counts of stars.

(ie approximately along a parallel of declination) through the central region between the three clusters. The slices were counted into 100 bins along their length, and the counts are presented in figures 7.10, 7.11 and 7.12. The horizontal line is simply the mode of the distribution of counts, and may not be the "best" estimate of the typical background count.

Although these diagrams are noisy due to the counts in each bin being about 12, they do seem to indicate not only enhanced numbers at the location of the actual clusters, but perhaps a deficit of counts either side of cluster #1. To establish this apparent phenomenon, ring counts were done centred on cluster #1, shown in figure 7.13. Of course the count in each annulus is normalised by the area of the annulus, but also account is taken where part of the annuli fall outside the rectangular scan area. The point on the diagram annotated "...Edge..." indicates where the first annulus to just touch one edge lies. The counts outside this radius become progressively less reliable, since they become less radially symmetric about the cluster.

Rather than clutter the diagram with a hundred error bars, the error function is plotted as a smooth curve at the bottom of the graph. It is derived from the square root of the original annular counts, scaled in the same way as the counts themselves.

The apparent dip is now more clearly seen, and it has a larger amplitude (four or five times) than the error curve. Before discussing physical implications, it is essential to test whether the feature is an artifact either of photographic plate or of measuring machine. Figure 7.14 shows the result of applying the same procedure to the objects classified as stars. There is perhaps still a small dip, of

much smaller amplitude, but there is also a slightly enhanced count at the cluster centre. This must mean that a small percentage of galaxies have been mis-classified as stars. On the whole, the star diagram is quite flat, as would be expected of the stellar distribution at high galactic latitude.

The conclusion is that this startling feature is real. Apparently centred on cluster #1 is a region of depleted numbers of galaxies some 12 Mpc in diameter. The main value of this result in the present study is that there exists a continuous structure over the same (projected) area as the group of clusters. The picture of the supercluster is now a number of clusters occupying a volume of space which is deficient in field galaxies compared to outlying regions. The most rich of the component clusters lies at the centre of the deficient region. The individual clusters appear not to lie strictly in the Hubble flow, and this suggest dynamical interaction between them. It is outside the scope of this thesis to model the dynamics, but it may be suggested that either the clusters formed from collecting field galaxies, or ready-formed clusters have since swept up the field galaxies. A further mechanism could be that interactions between clusters and field galaxies might have accelerated the galaxies, causing them to have been ejected from the region.

The scale of the supercluster is consistent with that in other superclusters investigated by other workers, for example the 6.8 h^{-1} bridge connecting two clusters in the Indus supercluster reported by Beard et al (1984). Kirshner et al (1981) have suggested the existence of voids from redshift data, and have since verified the initial findings (Oemler et al, 1985). The general conclusion is that the Universe is inhomogeneous on large scales.

Luminosity and Colour Segregation.

While not directly part of the supercluster research, it is interesting to use the Joyce Loebl photometry to investigate possible luminosity or colour segregation within the individual clusters. Clearly from visual inspection, the brightest two or three galaxies lie at the centres of the rich clusters. Figure 7.15 plots V_{26} as a function of radius for each galaxy in each cluster, and 7.16 similarly plots (B-V) as a function of radius. These diagrams show that overall, there is no obvious segregation by colour in any cluster, and clusters #2 and #3 do not seem to display any luminosity segregation. The evolutionary implication of this observation might be that, whatever the origin of the clusters, they have since become well mixed, that is, individual galaxies have completed a substantial fraction of an orbit since formation. Cluster #1 shows an apparent preference for bright galaxies nearer to the centre. It may be that a denser region of galaxy-forming gas gave rise to larger galaxies, or that since formation, galaxies have preferentially merged due to the higher probability of encounters.

Hubble's Constant.

Finally, an estimate of Hubble's constant H_o may be computed. For this purpose the group of three clusters are taken as an ensemble and the mean photometrically-derived distance combined with the mean radial velocity.

From comparison with Virgo, $\langle m-M \rangle = 38.8 \pm 0.5$. From Strom's (U-R) calibration, $\langle m-M \rangle = 38.1 \pm 1.7$. The weighted mean of these two values hardly differs from the "Virgo" value, and is $\langle m-M \rangle = 38.7 \pm 0.4$, which leads to a distance $d = 550 \pm 130$ Mpc. The mean redshift $\langle z \rangle = 0.159 \pm .007$ which corresponds to $v = 47700 \pm 2100$ kms^{-1}.

Therefore $H_o = 87 \pm 20$ km s^{-1} Mpc^{-1}.

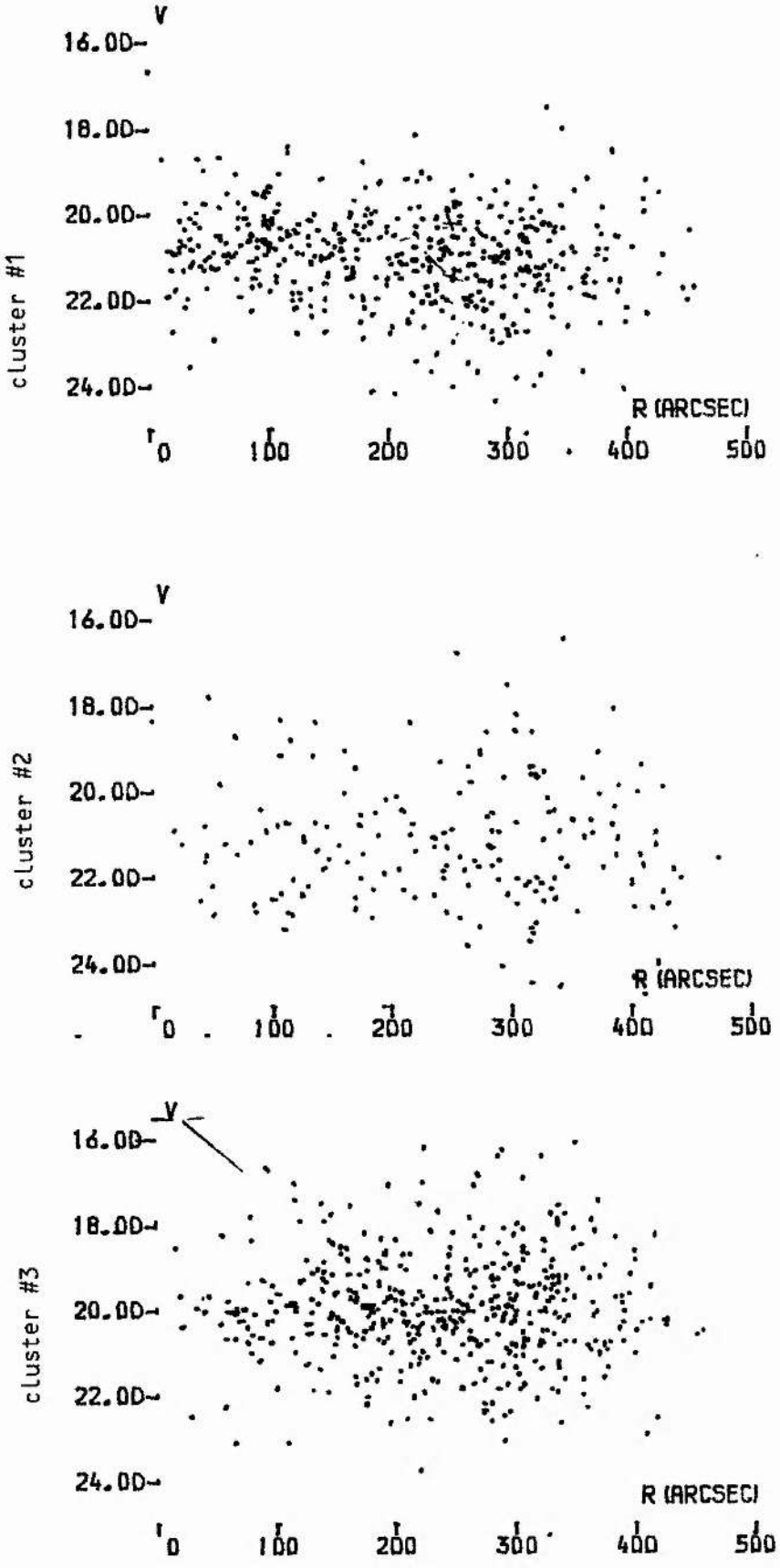

Figure 7.15: V_{26} vs radial distance from cluster centres.

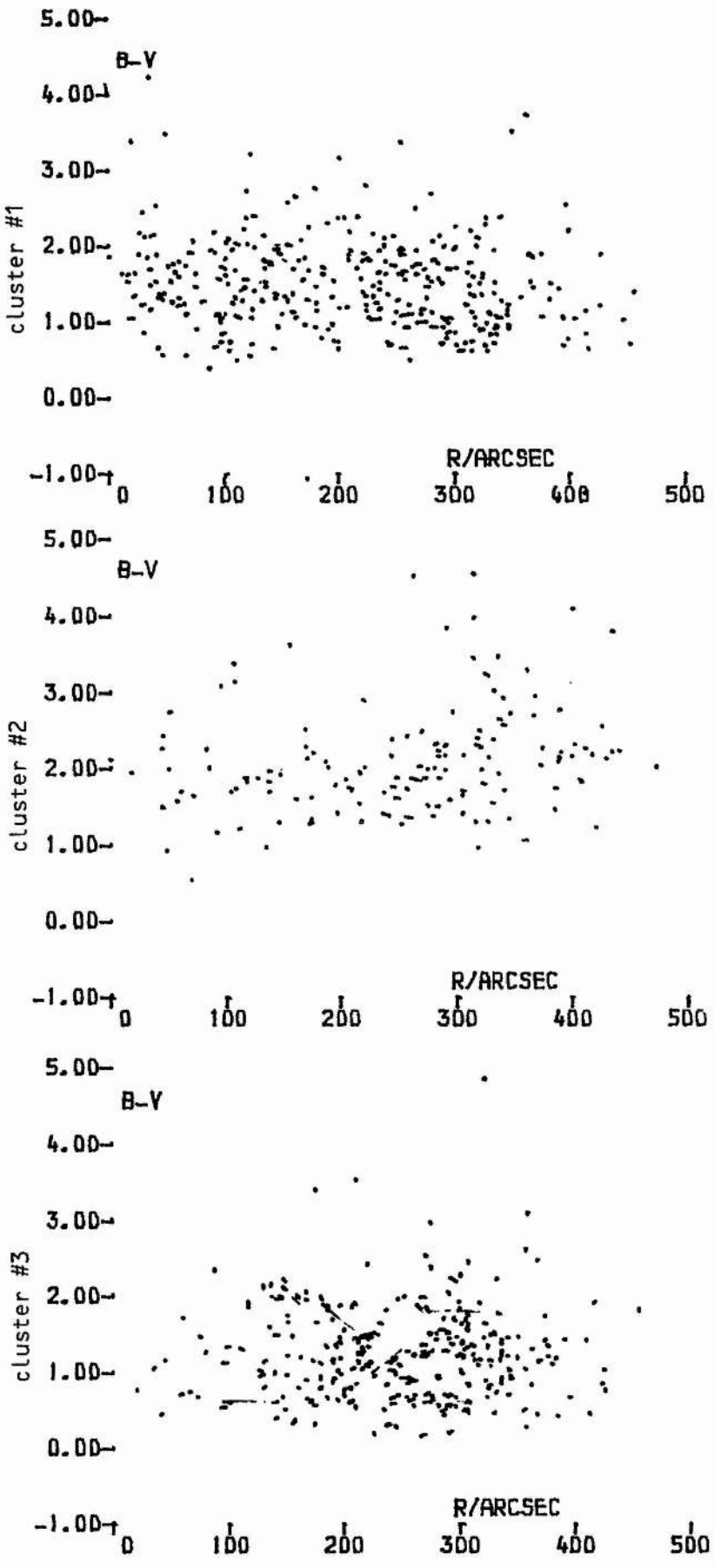

Figure 7.16: (B-V) vs radial distance from the cluster centres.

Epilogue.

The product of this work has herein been presented as a doctoral thesis, and will in due course be published. The issue has been settled in that the three visually identified rich clusters of galaxies actually lie in a compact region of space. A bonus is that a value for Hubble's constant is derived.

The project has also produced some other conclusions on procedural and organisational levels. For example, this work demonstrates how difficult is photographic photometry of faint, extended, and crowded objects, and describes ways to handle the problems. It is shown what the strengths and weaknesses of fast, automatic measuring machines are (APM specifically). While a machine such as APM can produce prodigeous quantities of data with small random errors, one has to be most careful in interpreting what, for example, the "magnitude" refers to. The way to use such a machine in work of this nature may be to scan a small region on a machine such as a Joyce Loebl and carefully reduce the data (in a way similar to that described in chapter III) to produce "ground truth" values. The APM data can then be statistically corrected to give for example V_{26} magnitudes.

Having said this, it has been tantalising that the photographic data is just not quite good enough to actually map out in three dimensions the structure of the supercluster. To do this precisely one could now obtain photometry from charge-coupled devices (CCDs) and radial velocities from fibre-optic multi-spectroscope instruments.

The future continuation of this work, it seems to the author, will

be large, possible whole sky, photographic surveys producing good statistical data, backed up and supplemented by precision measurement of a subset using new technologies.

****

APPENDIX I

Identifications.

Finding charts and lists of selected galaxies are presented in figures A1, A2 and A3. Objects are selected if they have been detected on two plates scanned by the Joyce Loebl, and two plates scanned by the APM, and have a measured redshift from the objective-prism material.

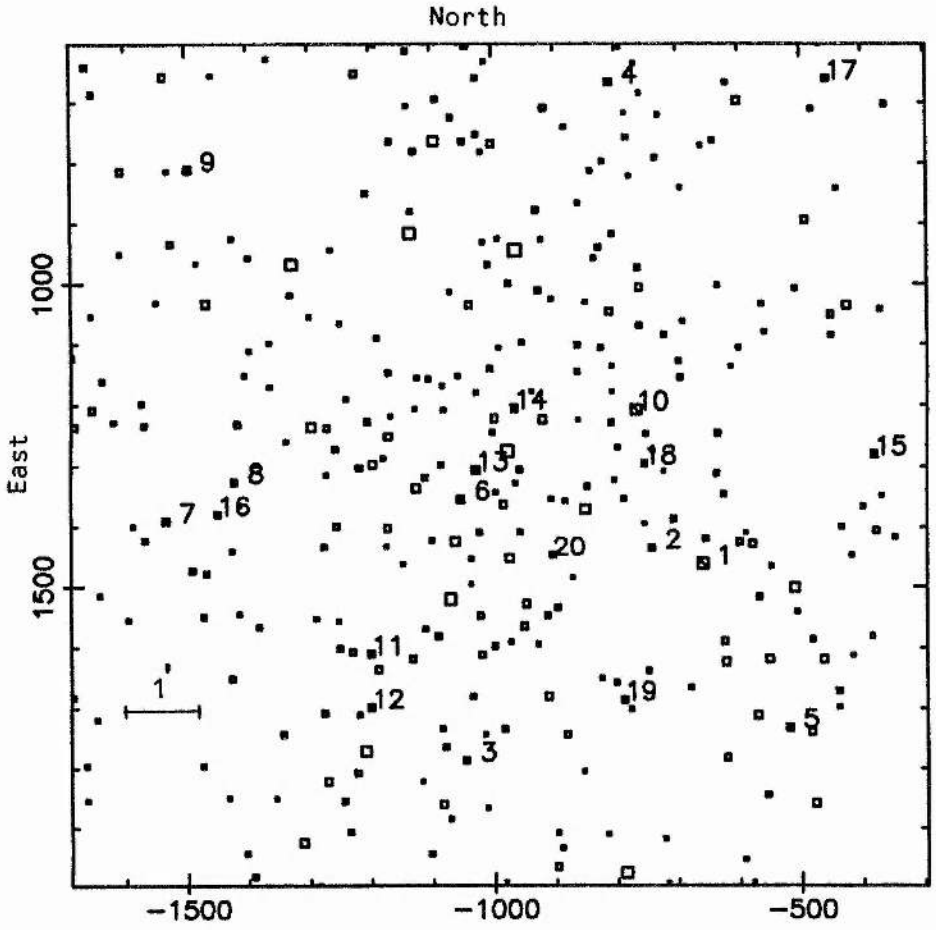

ref	V26	(U-B)	(B-V)	(V-R)	z
1	15.ØØ	3.Ø9	1.3Ø	1.Ø8	Ø.116
2	18.72			-1.64	Ø.13Ø
3	19.87	-Ø.Ø5	1.92	Ø.36	Ø.155
4	17.94		1.43	-Ø.Ø3	Ø.166
5	18.44		1.74	Ø.31	Ø.143
6	18.91	Ø.84	2.Ø5	-Ø.13	Ø.146
7	19.46	Ø.7Ø	2.15	Ø.55	Ø.182
8	19.56	Ø.34	2.Ø5	Ø.67	Ø.11Ø
9	19.4Ø	Ø.65	2.32	Ø.7Ø	Ø.142
1Ø	18.59	Ø.75	2.29	Ø.74	Ø.146
11	19.61	Ø.15	2.24	Ø.68	Ø.123
12	19.87	Ø.24	2.14	Ø.63	Ø.126
13	19.94	Ø.69	2.57	Ø.37	Ø.1Ø3
14	23.72		4.3Ø	Ø.38	Ø.149
15	2Ø.71	Ø.24	2.64	Ø.33	Ø.182
16	2Ø.24	-Ø.Ø3	2.2Ø	Ø.55	Ø.149
17	19.93	Ø.48	2.41	Ø.59	Ø.156
18	2Ø.93	-Ø.25	2.45	Ø.58	Ø.1Ø2
19	2Ø.55	-Ø.17	2.32	Ø.53	Ø.151
2Ø	2Ø.75		2.36	Ø.52	Ø.144

Figure A1: Finding Chart and List of Parameters for Cluster #1

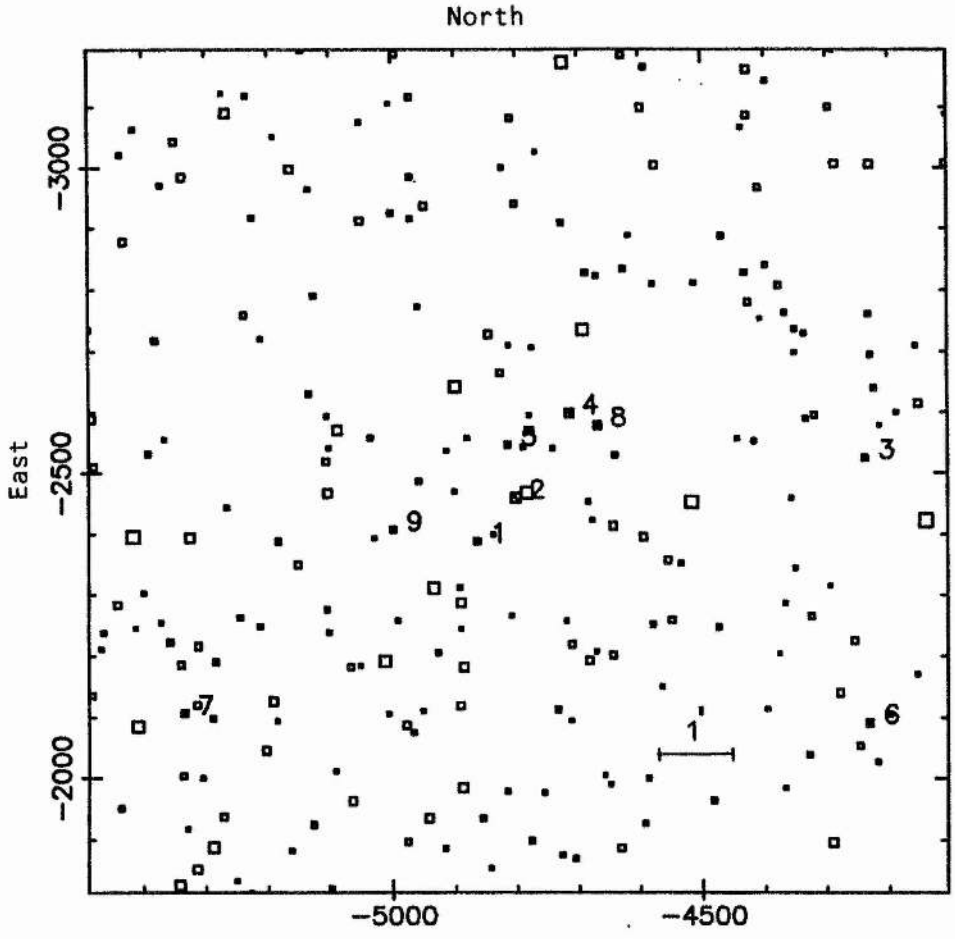

ref	V26	(U-B)	(B-V)	(V-R)	z
1	18.24	1.Ø4	1.44	Ø.29	Ø.192
2	18.76	Ø.94	2.64	Ø.28	Ø.15Ø
3	18.77	Ø.55	1.5Ø	Ø.17	Ø.192
4	19.11	Ø.87	2.65	-2.52	Ø.162
5	21.22	-Ø.Ø8	2.8Ø	Ø.36	Ø.165
6	21.28	Ø.39	3.36	Ø.24	Ø.166
7	21.14	Ø.18	3.Ø1	Ø.36	Ø.112
8	21.35	-Ø.Ø6	3.61	Ø.1Ø	Ø.171
9	22.62	-Ø.28	3.82	-Ø.63	Ø.135

Figure A2: Finding Chart and list of Parameters for Cluster #2

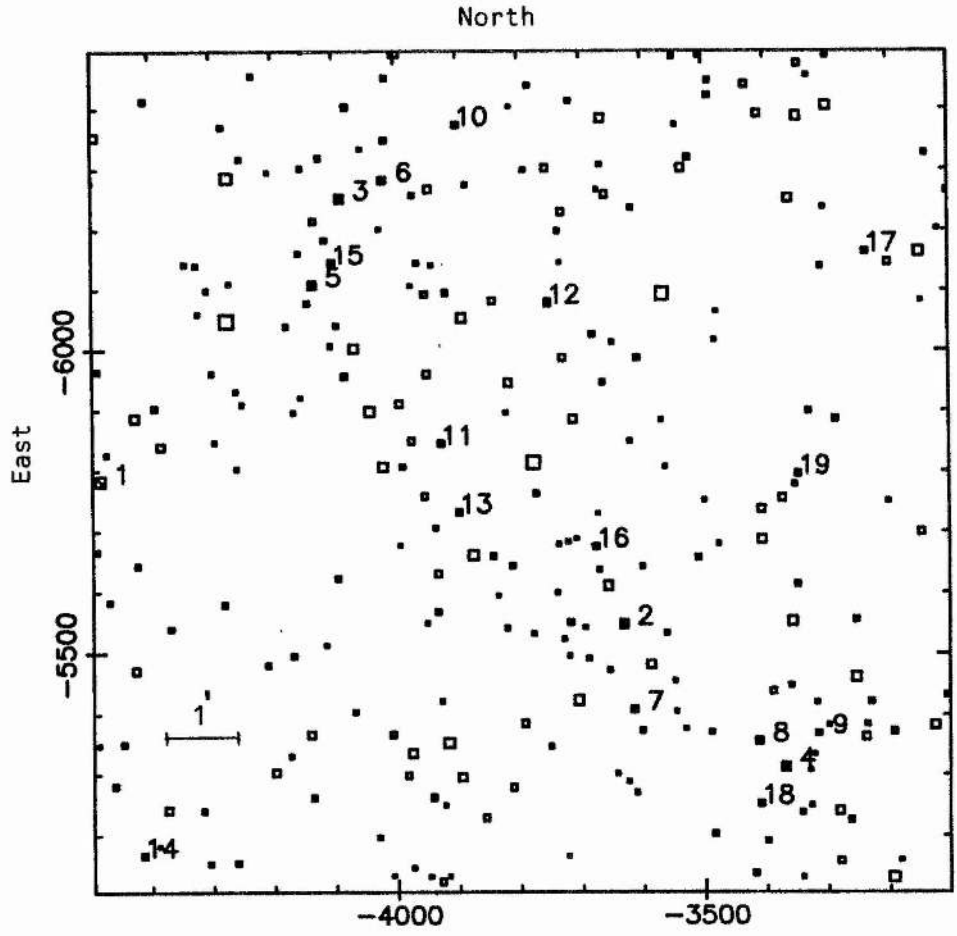

ref	V26	(U-B)	(B-V)	(V-R)	z
1	14.11	1.19	1.Ø1	Ø.Ø5	Ø.145
2	15.9Ø		2.Ø9	Ø.53	Ø.159
3	15.56	1.25	2.12	Ø.4Ø	Ø.18Ø
4	15.7Ø	1.81	1.88	Ø.48	Ø.129
5	15.94	1.Ø3	1.92	Ø.67	Ø.139
6	16.64		1.42	Ø.65	Ø.1Ø3
7	17.19		1.62	Ø.67	Ø.161
8	16.9Ø		1.82	Ø.78	Ø.191
9	17.88	Ø.Ø3	1.25	Ø.89	Ø.111
1Ø	17.28	1.11	1.23	Ø.47	Ø.173
11	17.74		1.71	Ø.67	Ø.117
12	16.97		1.58	Ø.71	Ø.152
13	17.63		1.65	Ø.42	Ø.185
14	17.61	Ø.75	1.23	Ø.74	Ø.166
15	17.28		1.72	Ø.69	Ø.194
16	17.81		1.82	Ø.62	Ø.171
17	17.78		1.26	Ø.58	Ø.142
18	17.67		1.48	Ø.6Ø	Ø.161
19	17.91		1.41	Ø.78	Ø.171

Figure A3: Finding Chart and list of Parameters for Cluster #3

References

Bahcall, N.A., 1979, Ap.J., **232**, 689.

Bean, A.J., Efstathiou, G., Ellis, R.S., Peterson, B.A., and Shanks, T., 1983, Mon. Not. R. astr. Soc. **205**, 605.

Beard, S.M., Cooke, J.A., Emerson, D., & Kelly, B.D., 1984, in Clusters and Groups of Galaxies, Ed. Mardirossian et al., p 17.

Binggeli, B., 1982, Astr. Ap., **107**, 330.

Blackman, C.P., 1977, Ph.D. thesis (St. Andrews).

Braid M.K. & MacGillivray H.T., 1978, M.N.R.A.S., **182**, 241.

Brault, J.W. & White, O.R., 1971, Astr. & Ap., **13**, 169.

Breda, I.G. van, Hill, P.W., Campbell, R.J., Lynas-Gray, A.E. & Carr, D.M., 1974, Proc. 1st CAMAC Symp (Sup to CAMAC Bull 9), 157.

Brown, A., Bunclark, P.S., Stapleton, J.R. and Stewart, G.C., 1979, M.N.R.A.S., **187**, 35.

Brownlee, K.A., 1967, Statistical Theory and Methodology, pub Wiley.

Bunclark, P.S., 1982, Proc. Workshop on Astronomical Measuring Machines, occ. reports, Royal Observatory Edinburgh.

Bunclark, P.S. & Irwin, M. J., 1983, Proc. Statistical Methods in Astronomy Symp., Strasbourg.

Bunclark, P.S., Fraser, C.W. & Dodd, R.J., 1980, Astr. & Ap. Suppl. Ser. **40**, 81.

Carr, D.M. & Stapleton, J.R., 1978, ESO/SRC Conference on Applications of CAMAC to Astronomy p. 143.

Cooke, J.A., Emerson, D, Kelly, B.D., MacGillivray, H.T. & Dodd, R.J., 1981, M.N.R.A.S., **196**, 397.

Cooke, J.A., Kelly, B.D., Beard, S.M., and Emerson, D., 1984, in Astronomy with Schmidt-Type Telescopes, ed M. Capaccioli.

Conover, Practical Non-parametric Statistics.

Cousins, A.W.J. & Stoy, R.H., 1962, Roy. Obs. Bull., **49**, 1.

Cousins, A.W.J., 1976, Memoirs Roy. Astron. Soc., **81**, 25.

Dekel, A., West, M.J. & Aarseth, S.J., 1984, Ap.J., **279**, 1.

Dressler, A., 1978, Ap.J., **223**, 765.

Faber, S.M., 1973, Ap.J., **179**,731.

Fischel, D., 1976, A.J., **81**, No. 4, 285.

Fraser, C. W., 1977, Astron. Astrophys. **29**, 161.

Gonzalez, R.C. & Wintz, P.W. 1977, Digital Image Processing, (Pub. Addison-Wesley).

Gray, D.F., 1975, The Observation & Analysis of Stellar Photospheres. (Pub. Wiley).

Gull, S.F. & Daniell, G.J., 1978, Nature **272**, 686 (April).

Harrison, E.R., 1974, Astrophys. J. (Letters), **191**, L51.

Hartmann, J., A simple interpolation formula for the prismatic spectrum, Ap.J. **VIII**, 1898.

Hewett, P.C., Irwin, M.J., Bunclark, P.S., Bridgeland, M.T. & Kibblewhite, E.J., 1985, M.N.R.A.S., (in press).

Høg, E. & van der Heide, J., 1976, Perth 70: A Catalogue of 24900 Stars. AB Handlungen Aus Der Hamburger Sternwarte, Band **IX**.

Jones, C. & Forman, W., 1984, Ap. J. **276**, No. 1, 38.

Kibblewhite, E.J., Bridgeland, M.T., Bunclark, P.S., Cawson, M.G.M. & Irwin, M.J., 1984, M. Capaccioli (ed.), Astronomy with Schmidt-Type Telescopes, (Pub. D. Reidel).

Kibblewhite, E.J., Bridgeland, M.T., Bunclark, P.S. & Irwin, M.J., 1983, Proc. of the Astron. Microdensitometer Conference, Washington.

Kirshner, R.P., Oemler, A., Schecter, P.L., and Schectman, S.A., 1981, Astrophys. J. **248**, L57.

Mihalas, D. and Binney, J., 1981, Galactic Astronomy, pub. Freeman.

MacGillivray, H.T., and Dodd, R.J., 1982, Astrophys. Sp. Sci. **81**, 231.

Moore, C.H., 1974, Astr. & Ap. Suppl., **15**, 497.

National Algorithms Group, 1985, FORTRAN Library Routine Documentation.

Newell, B. & O'Neill, E.J. Jr., 1977, P.A.S.P., **89**, 925.

Oemler, A., 1974, Ap.J., **194**,1.

Oemler, A., 1985, in Cambridge Workshop on Clusters of Galaxies, ed. Hewett, P.C., unpublished.

Parker, Q.A., MacGillivray, H.T., Dodd, R.J., Cooke, J.A., Beard, S.M., Kelly, B.D. and Emerson, D., 1984, in Astronomy with Schmidt-Type Telescopes, ed. M. Capaccioli.

Pence, W.D., 1976, Ap.J., **203**, 39.

Schechter, P., 1976, Ap.J., **203**, 297.

Shu, F.H., 1982, The Physical Universe.

Singleton, R.C., 1968, Communications of the ACM, **11**, No. 11, 776.

Strom, R.M. & Strom, S.E., 1978, A.J., **83**, No. 2, 73.

Tsubaki, T. & Engvold, O., 1975, AAS Photbull., **9**, 17.

Vaucouleurs, G & A. de & Corwin, H.G., 1976, Second Reference Catalogue of Bright Galaxies, Uni. Texas Press.

Vaucouleurs, G. de, 1968, Applied Optics, **7**, 1513.

Visvanathen, N. and Griersmith, D., 1979, Ap. J. **230**, 1.

West, R.M., and Frandsen, S., 1981, Astron. Astrophys. Suppl. Ser. **44**, 329.

Whitford, A.E., 1975, in Galaxies & the Universe, ed. Sandage, Pub. Univ. of Chicago Press.

INDEX